

VICERRECTORÍA DE INVESTIGACIÓN Y POSTGRADO <u>DIRECCIÓN DE POSTGRADOS Y POSTÍTULOS</u>

FACULTAD DE CIENCIAS DEPARTAMENTO DE FÍSICA Y ASTRONOMÍA

SPECTROSCOPIC CLASSIFICATION OF MASSIVE GALAXY CLUSTER MERGER CANDIDATES

Tesis presentada para optar al Grado Académico de Magíster en Astronomía.

AUTOR: HUGO ANTONIO PRADO PLAZA

LA SERENA, CHILE, Mayo 2022

CONSTANCIA

Don				 	 	 	
HAC	E CO	NSTA	R:				

Que el trabajo correspondiente a la presente Tesis de Magíster, titulada "Spectroscopic classification of massive galaxy cluster merger candidates", ha sido realizada por Don Hugo Antonio Prado Plaza, bajo mi dirección.

Para que conste y en cumplimiento de las normativas vigentes de la Universidad de la Serena, Chile, firmo el presente documento en La Serena, Chile, Mayo de 2022

TESIS PARA OPTAR AL GRADO DE MAGÍSTER EN ASTRONOMÍA

ACUERDAN OTORGARLE LA CALIFICACIÓN DE:

La Serena, Chile, Mayo de 2022

"(...) To live is to risk it all; otherwise you're just an inert chunk of randomly assembled molecules drifting wherever the universe blows you." - Rick Sánchez

ACKNOWLEDGMENT

Principalmente, quiero agradecer a todos aquellos que me acompañaron durante estos 2 años. Si bien, la presencia de algunos fue mayor a la de otros, estoy agradecido por todos los pequeños detalles que aportó cada uno de ustedes :3.

Además, agradezco a mi suegrita por abrirme la puerta cuando me quedo afuera en las mañanas xD. Gracias al profe Nilo por ayudarme a sacar adelante la tesis, aun le debo una chela. Ana, gracias por mostrarme lo weon que soy en la vida, Te odiaré pa siempre Jsdjdj. Agradecimientos al Sr. Daniel suizo por su constante tergiversación de los hechos. Gracias al mitologico matipletorrasca con milanesa por llegar al alba del segundo día. Agradecido con el juanpi por mantener la amistad no importa que tan viejos estemos >:{P.

Gracias al Mani por enseñarme que nunca estare solo y también gracias al Diego, con quien hicimos todo el camino enfrentando tareas, prácticas, laboratorios y pruebas codo a codo en la licenciatura. No lo hubiese logrado sin ti men, y fue mil veces mas difícil sin ti durante esta etapa :L .

Agradezco a mi familia por el apoyo constante que me da aliento cada vez que olvido respirar. Finalmente, una dedicación especial para Pamela. Ya me es costumbre tenerte a mi lado para avanzar por sobre cada obstáculo que se presente. Quiero seguir dando todo de mi para descubrir que nos depara el futuro <3.

Resumen

El estudio de los cúmulos de galaxias es escencial para nuestro entendimiento de la evolución de galaxias, así como también para la evolución del Universo, se encuentran en el máximo del campo de densidad de materia (materia oscura) y así, acretan grupos de galaxias y otro cúmulos de la red cósmica mientras evolucionan. Esta constante acreción implica que los cúmulos de galaxias, raramente se encuentran en equilibrio y usualmente llevan a cabo procesos de fusión a lo largo de su historia, algunos de estas fusiones se encuentran entre los procesos más energéticos del Universo y así, estos eventos proveen con condiciones extremas para estudiar la evolución de galaxias, física de partículas y cosmología. Los cúmulos en fusión juegan un papel importante en la aceleración de rayos cósmicos y la generación de rayos gamma, y pueden llegar a ser usados para acotar la sección eficaz de la partícula de materia oscura cuando interactua con sí misma. Desde un punto de vista cosmológico, los cúmulos en fusión nos permiten probar escenarios de materia oscura fría (ΛCDM) y abren una ventana al universo distante gracias a su eficiencia magnificante como lentes gravitacionales.

La clasificación de sistemas no relajados se puede hacer usando diferentes observables, por ejemplo, al usar la morfología en la emisión de rayos X, usando la emisión en radio, observando la forma de la distribución de las galaxias en los cúmulos; al combinar observaciones en diferentes longitudes de onda, como el desfase entre la posición del máximo de emisión en rayos X con la galaxia más brillante del cúmulo (BCG) o usando espectroscopía para medir la forma del perfil de velocidades. Este último método proporciona la distribución de galaxias

en la línea de visión, permitiendonos crear escenarios tridimensionales, además de caracterizar la fusión en sí, sumado a la clasificación del estado dinámico.

Las grandes muestras de cúmulos de galaxias son identificadas usando surveys en el óptico, rayos X, y con el efecto de Sunyaev-Zeldovich (SZ). Actualmente existen grandes muestras de SZ de cúmulos de galaxias disponibles, tanto en el Planck telescope, Atacama cosmology telescope y el South Pole Telescope (SPT), sumando un total aproximado de 2,000 cúmulos de galaxias masivos. Se espera que el telescopio espacial de rayos X eROSITA pueda aumentar este número a unos 100,000 grupos y cúmulos de galaxias, otorgando una gran muestra de cúmulos en interacción.

En esta tesis, como nuestro trabajo introductorio a los surveys venideros, se toman 15 GCs in un rango de redshift 0.3 < z < 0.65 provinientes del SPT-SZ 2,500 deg² survey donde 14 de ellos, seleccionados por su gran desfase entre la BCG y el centroide/máximo de la emisión de rayos X, son candidatos a cúmulos perturbados. Para estos cúmulos, que representan los cúmulos más masivos en el universo, se usan datos espectroscopicos de Gemini/GMOS para estimar el redshift de los cúmulos, sus masas dinámicas y confirmar la membresía de candidatos a BCG. Se analiza la distribución de las galaxias de los cúmulos en la linea de vision y en el plano proyectado para confirmar el estado dinámico de los cúmulos. Nuestro set de tests consiste en test estadísticos que prueban la distribución en 1, 2, y 3 dimensiones. Al tomar un corte en velocidad de $\pm 3,000~{\rm km\,s^{-1}}$ para seleccionar miembros del cúmulo, se confirma la membresía 11 BCGs indicando un nivel de contaminación del 27%. Se encuentra que 7 cúmulos presentan evidencia de perturbación por almenos uno de los test estadísticos. Particularmente, el acercamiento tridimensional con DS test demostró ser inadecuado para las separaciones de subestructuras en velocidad en nuestra muestra. Más aún, haciendo simulaciones numericas se encuentra que este alcanza niveles de eficiencia sobresalientes cuando se prueban fusiones que no esten superpuestas en linea de visión ni en el plano del cielo. En estos casos, DS test muestra bajos niveles de eficiencia para detectar subestructura que son aún más bajos para fusiones en el plano del cielo. Esta simulación tambien muestra que DS test funciona mejor en fusiones con cúmulos de escalas diferentes a cuando se tienen cúmulos de escalas similares. Además, recolectamos una muestra grande de 138 GCs y corremos los tests estadísticos encontrando que un 36% de esta muestra presenta evidencia de perturbación y un 54% no muestra ningún indicio de perturbación.

Summary

The study of galaxy clusters (GC) is central to our understanding of galaxy evolution as well as the evolution of the Universe. They are located at the peaks of the (dark) matter density field, and as such they accrete galaxy groups and other clusters from the cosmic web as they evolve. This constant accretion implies that GC are rarely in equilibrium and they often undergo mergers during their history. Some of those merging are among the most energetic events in the Universe and as such they provide extreme conditions to study galaxy evolution, particle physics, and cosmology. Merging clusters play a role in cosmic ray acceleration and gamma ray generation, and they can be used to narrow the cross section of the dark matter particle when it interacts with itself. From a cosmological perspective, merging clusters allow us to test a cold dark matter scenario (Λ CDM) and they open a window to the distant universe thanks to their magnifying efficiency as gravitational lenses.

The classification of non-relaxed systems can be done using different proxies e.g. by using the morphology of the X-ray emission; using the radio emission; looking at the shape of the distribution of galaxies in clusters, by combining observations at different wavelengths such as the phase shift between X-ray peak with the Brightest cluster's galaxy (BCG); or using spectroscopy to measure the shape of the velocity dispersion. This last method provides line-of-sight distributions allowing us to build three dimensional scenarios, furthermore characterizing the merger itself in addition to classifying the dynamical state.

Large samples of galaxy clusters are identified using surveys in optical, X-rays,

and Sunyaev-Zeldovich (SZ) effect. Actually there are large SZ samples of galaxy clusters available such as the Planck telescope, Atacama cosmology telescope, and the South Pole Telescope (SPT) accounting for approximately 2,000 massive galaxy clusters in total. Expectations for the X-ray space telescope eROSITA is to raise this number to 100,000 galaxy groups and clusters providing a large sample to detect a large amount of interacting clusters.

In this thesis, as our pilot work to face the upcoming surveys, we use 15 GCs in the redshift range 0.3 < z < 0.65 from the SPT-SZ 2,500 deg² survey where 14 of them were selected by their large offset between the BCG and the X-ray peak/centroid as disturbed cluster candidates. For these clusters, which represent the most massive GCs in the universe, we use spectroscopic data from the Gemini/GMOS spectrograph to estimate cluster redshifts, dynamical masses, and confirm the membership of BCG candidates. We analyze the distribution of cluster galaxies in line of sight and projected space to confirm the dynamical state of the clusters. Our battery of tests consist on statistical tests that probes the distribution on 1, 2, and 3 dimensions. By taking a velocity cut level of $\pm 3.000~{\rm km\,s^{-1}}$ to select cluster members we confirm the membership of 11 BCGs indicating a contamination level of 27%. We find that 7 clusters present evidence of perturbation by at least one of the statistical tests. We find that 4 clusters show no evidence of perturbation through multiple velocity cut levels employed. Particularly, our 3D approach with DS test demonstrated to be unsuitable for the velocity separations of substructures in our sample. Furthermore, by performing numerical simulations we find that it reach outstanding confidence levels when testing mergers not superimposed in line of sight or sky plane. In these cases, DS test show low efficiency levels to detect substructure, and even lower levels for mergers in the plane of the sky. This simulation also show that DS test work better in mergers with clusters of different scales than in those with clusters with similar scales. In addition, we collect a large sample of 138 GCs and run the statistical tests to find that 36% of this sample show evidence of perturbations

and a 54% of the clusters show no deviations from dynamical equilibrium.

Contents

1	Intr	oducti	on	1
	1.1	Galaxy	clusters	1
	1.2	Interac	etion of galaxy clusters	ę
	1.3	Cluster	r sample and thesis goals	8
2	Obj	ectives	3	10
3	Dat	a		11
	3.1	Selection	on of the Merging cluster candidates and the Galaxies for spectroscopy	11
	3.2	Mask o	design and Observations	14
	3.3	Data r	eduction	16
	3.4	Spectro	oscopy	18
		3.4.1	Spectra treatment before redshift measurement	18
		3.4.2	Redshift measurements using FXCOR	19
		3.4.3	Automated redshift estimation pipeline	22
	3.5	Data fi	rom literature	27
	3.6	Goodn	nan Data	27
4	Ana	dysis		29
	4.1	Cluster	r redshift, membership selection, and dynamical mass	29
		4.1.1	Cluster redshift and velocity dispersion	29
		4.1.2	Membership selection	30
		4.1.3	Dynamical mass	31
	4.9	Dynan	pical stata indicators	21

CONTENTS

		4.2.1	Anderson-Darling test	32
		4.2.2	Kolmogorov-Smirnov test	33
		4.2.3	Gaussian Mixture Modelling	34
		4.2.4	Dressler-Shectman test	35
5	Res	ults		37
	5.1	Cluster	properties and BCG membership	37
	5.2	Dynam	ical state	40
6	Disc	cussion	and conclusions	4 6
	6.1	Dynam	ical state in the LoS: AD and KS test	46
	6.2	Dynam	ical state in the spatial direction: GMM2D	47
	6.3	3D app	roach of the dynamical state: DS test	49
	6.4	Simulat	ting 3D mergers	49
	6.5	Dynam	ical state of 138 galaxy clusters	53
		6.5.1	Relaxed sample	56
7	Futi	ıre woı	rk	5 9
A	Pipe	eline aı	nd scripts	81
	A.1	Downlo	pading DES images and catalogs	81
		A.1.1	Donwloading SPT spectroscopic catalogs	85
	A.2	RCS al	ign with saods9	85
	A.3		eduction	86
		A.3.1	Identifying and correcting first end over-scaled spectra	86
	A.4	Catalog	gs and BCG matching	89
	A.5	Cluster	redshifts and dynamical masses	91
	A.6	Dynam	ical state indicators	95
		A.6.1	AD and KS test	95
		A.6.2	Gaussian Mixture Modelling	96
		A.6.3	DS test and Monte Carlo method	98

A.7	Sample size statistics for 1D dynamical tests	•	•	•	•	•		•	•	•	•	•	•	•	•	100
A.8	Statistics for 2D dynamical tests															104

List of Figures

1.1	Figure from Harvey et al. (2014) illustrating all three components of an infalling	
	structure to the main cluster. The notation is G for gas, D for DM, I for the	
	intersection point closest to the DM in the direction towards the gas, and S	
	('stars') for galaxies	4
1.2	Ram pressure stripping of gas from a galaxy in ESO 137-001 in the Norma	
	cluster. Image taken with the HST	(
3.1	Top panel: Projected density contours (from the RCS galaxies) overlaid on the	
	DES i-band images for the unrelaxed cluster SPT-CLJ0522-5026 at $z=0.52.$	
	Levels begin at 100 galaxies $\rm Mpc^{-2}$ and increase linearly with increments of	
	50 galaxies Mpc^2. The field-of-view of the image is $7.7 \times 7.7~\mathrm{arcmin^2}$ (\sim	
	$2.9 \times 2.9 \ \mathrm{Mpc^2}$ at the redshift of SPT-CLJ0522-5026). Note the two clear	
	separate structures in SPT-CLJ0522-5026 (separated by ~ 0.8 Mpc). Other	
	over densities are detected and possible connected to the cluster. The red	
	square shows the BCG location. The large blue circle indicates the radius	
	R_{200} . Bottom panel: Color-magnitude diagram for SPT-CLJ0522-5026 with	
	the total (black dots), blue (blue dots), and red-sequence (red dots) galaxies	
	within R_{200} . The lines correspond to the best fit of the model \pm 0.22 mags	13
3.2	Obj ID: 252454243, slit number 32, second mask for SPT-CLJ0144-4807. 1D	
	spectra shown using splot and 2D spectra displayed with SAODS9. Highlights	
	indicate some visually identified absorption lines	17
3.3	LINECLEAN interactive panel example. Obj ID: 158525328, slit number 30, first	
	mask for SPT-CLJ2344-4224. The figure shows the flux calibrated 1D spectra.	
	The central curve is the order 13 Chebyshev fit to the continuum	18

LIST OF FIGURES

3.4	An example of a star and a low-signal spectra	19
3.5	Spectra of sources from different clusters denoting the presence of the OH line	
	at 7620Å line	19
3.6	$\label{thm:continuous} \mbox{Template spectra listed from top to bottom are $\it syn4$, $\it eltemp$, $\it sptemp$ and $\it habtemp$.}$	21
3.7	Example of the interactive spectrum mode of fxcor. The top panel shows	
	the spectra of a galaxy from SPT-CLJ0111-5518 while the bottom panel is	
	the $syn4$ spectra template. Both spectra have their continuum subtracted. In	
	the interactive mode, the ${f s}$ hotkey can be used to select with the cursor the	
	regions to correlate (the green range line). These are the rsample and osample	
	parameters	22
3.8	Histogram of residual of the heliocentric velocities normalized by the quadratic	
	errors for the 49 galaxies observed in two different masks. The red solid $line$	
	indicate the mean value of the distribution. The histogram shows the distri-	
	bution from -1,200 to 2,200 $\mathrm{km}\mathrm{s}^{-1}$	25
3.9	GCs grouped by requested exposure time. In the vertical axis the apparent	
	magnitudes in the i band (taken from DES survey) and the horizontal axis	
	shows the absolute value of Quintana et al. (2000) statistic. In the legend is	
	also the characteristic i-band magnitude of the clusters. The red line indicate	
	the selected limit magnitude at which fainter galaxies' spectra is inspected	
	visually and redshifts are estimated interactively	26
5.1	Redshift histograms for the 15 clusters (bin size 0.005). Red bars and inner	
	panels (bin size 250 km s ⁻¹) indicate galaxies within $\pm 5{,}000$ km s ⁻¹ . Black	
	dashed lines indicate the position of the BCG	39
5.2	Peculiar velocity of galaxies inside $\pm 5{,}000~{\rm kms^{-1}}$ with member galaxies as red	
	bars (bin size 250 km s ⁻¹). The <i>Black dashed</i> line indicate the position of the	
	BCG. Green dashed line mark 2,500 km s ⁻¹ . The shaded regions represent 1,	
	2, and 3σ going from darker to lighter blue regions and dashed line	40
		-

LIST OF FIGURES

5.3	Distribution of galaxies in the projected plane for the 7 disturbed clusters	
	together with contour levels for the numerical density map of RCS galaxies.	
	Circles and diamonds show galaxies which belong to components found with	
	GMM2D (only circles in the case of just one component). Centers and stan-	
	dard deviations of components found by GMM2D are noted with black solid	
	perpendicular lines. The black cross indicate the position of the BCG and	
	the dashed circle indicate R_{200} . Red and blue shades indicate the velocity of	
	galaxies. The side panel on every plot shows the velocity distribution with the	
	BCG pointed as a dashed black line and member galaxies as red filled bars	44
6.1	An example of the double Gaussian distribution with config. set 1 and an angle	
	of 45°	51
6.2	α values for 138 galaxy clusters. \textit{Cyan} dots indicate 13 clusters from the S13	
	sample, $green$ dots are 48 from the R14 sample, $blue$ are 62 from B16, and red	
	dots are the 15 clusters presented in this paper. The red and lightblue circles	
	mark clusters from the disturbed and the relaxed sample, respectively. $$. $$.	54
6.3	D^* values for 138 galaxy clusters	55
6.4	DS p -values for 138 galaxy clusters	56
A.1	The DES science DB access tool. The right terminal prompts the SQL com-	
	mand lines where you can check the syntax before submitting the job	82
A.2	An example of a first end over-scaled spectra in the left panel. The right panel	
	shows the same spectra after the correction	87
A.3	left: Same first end over-scaled spectra of Fig. A.2. right: histogram of over-	
	scaled pixels in the first end of the continuum. The resulting wvlim in this	
	example is 4660Å	89
A.4	Saods9 RGB displays of cluster galaxies with BCG candidates, SOAR BCG,	
	and the best match found in our catalogs for both clusters, SPT-CLJ2344-4224	
	and SPT_CL 10600_4353	91

L	List of Tables							
	3.1	Sequence of rounds for spectroscopy with fxcor						
	5.1	Spectroscopy results of 15 SPT Clusters						
	5.2	$\pm 3,000~{\rm kms^{-1}}$ sample dynamical tests results						
	5.3	$\pm 2,500 \mathrm{km s^{-1}}$ sample dynamical tests results						
	5.4	$\pm 3\sigma~{\rm kms^{-1}}$ sample dynamical tests results						
	6.1	Parameter sets for 3D merger simulation						
	6.2	Results of 3D merger simulation. $\theta_c = 0^{\circ} \dots \dots$						
	6.3	Results of 3D merger simulation. $\theta_c=45^{\circ}$						
	6.4	Results of 3D merger simulation. $\theta_c = 90^{\circ}$						
	6.5	Percentage of NG classifications by each criteria for 138 galaxy clusters 55						
	6.6	Spectroscopy results for 13 Z20 relaxed clusters						
	7.1	MCMAC results on SPT-CLJ0522-5026						
	A.1	Fraction of NG classifications						

A.5 Best Double Gaussian fit found by lmfit to the velocity profile of SPT-

102

Chapter 1

Introduction

1.1 Galaxy clusters

The impressive success of Hubble's test in the first half of the XX century (Hubble, 1926) opened the gates to map the large scale structure of the Universe (LSS). A cosmic scenario of hierarchical formation in which stars are organized into galaxies, which in turn form galaxy groups, galaxy clusters, superclusters, sheets, walls, and filaments which are separated by immense voids, creating a vast foam-like structure (Carroll and Ostlie, 2017). This revealed the expanding nature of the Universe which is described by the Hubble constant, H_0 (Hubble, 1929). This expansion causes that distant galaxies display their electromagnetic spectrum in redder (larger) wavelength regions. This shift is known as redshift, z, and it is related to the scale factor at a given time t as

$$a(t) = \frac{1}{1+z}.$$

Several galaxy redshift surveys have been carried out, notable examples includes the 2dF Galaxy Redshift Survey, the Sloan Digital Sky Survey (SDSS-II), and the Galaxy And Mass Assembly (GAMA) survey. Studies using these redshift catalogs (e.g., Davis et al., 1982; York et al., 2000; Pimbblet et al., 2004; Porter and Raychaudhury, 2005) indicate the presence of filaments at scales >10 h⁻¹ Mpc (Coil, 2013) where their elemental component, from which the filamental structure is drawn, are galaxy clusters.

The study of galaxy clusters (GCs) is central to our understanding of galaxy evolution as well as the evolution of the Universe. Their formation corresponds

to the collapse of the largest gravitationally bound overdensities in the initial density field (Kravtsov and Borgani, 2012). GCs can be roughly 100 times the diameter and 1,000 times the mass of the largest galaxies (Allen et al., 2011). With diameters >1.5 h⁻¹Mpc and masses from 3×10^{14} to a few 10^{15} M_{\odot}, they can hold as few as 50 or more than 10,000 member galaxies (Schneider, P., 2015). GC's three main components are galaxies, which includes stars, gas, and dust in member galaxies; the intra-cluster medium (ICM), that consists mainly of ionized hydrogen and helium, and accounts for most of the baryonic material in GCs; and the Dark Matter (DM) halo. Baryonic matter account for ~20% of the total GC matter while the other 80% is DM. Meanwhile, This 20% of baryonic matter is 3% stars and the rest correspond to ICM and the gas/dust component in galaxies which are in constant feedback (Schneider, P., 2015; Bykov et al., 2015).

The ICM consists mainly on hot gas at temperatures between 10^7 to 10^8 K that permeates the GC. In this range of temperatures, the gas exists as a hot plasma in which electrons passing through the electric field of near ions are decelerated. This in turn cause a loss of kinetic energy in the electron, which is converted into radiation, and also produce a loss of energy in the plasma, causing the overall temperatures of the gas to cool down. This effect is known as thermal bremsstrahlung and is the reason on why the ICM has X-ray emission.

In GCs, there is often found in the bottom of the potential well a single massive central galaxy, which is typically the Brightest Cluster Galaxy (BCG). BCGs are the most massive galaxies in the universe. They are generally elliptical galaxies which lie close to the geometric and kinematical center of their host galaxy cluster, hence at the bottom of the cluster potential well (Lin and Mohr, 2004), and generally coincident with the X-ray emission center (Mann and Ebeling, 2012a). They have unusually extended envelopes while keeping modest stellar velocity dispersions (i.e. steeper L- σ relation than for other bright cluster galaxies, Lauer et al., 2014) and their typical stellar masses are $M_* \sim 2 \times 10^{11} h^{-2} M_{\odot}$ (Schneider, P., 2015). Also, the mass of their central black hole could be tightly correlated with the mass of their galactic bulge (Graham, 2016), but this relation is apparently steeper for BCGs too (Desroches et al., 2007).

GCs exhibit an appropriate environment for the study of gravitational lenses; Light from objects that are behind GCs is distorted due to the deformation of the space-time curvature product of the large mass of the GC. These distortions are part of the predictions of Albert Einstein's general theory of relativity (e.g.,

Einstein, 1936). Gravitational lenses can work as natural telescopes to magnify galaxies at high redshifts (Barnacka, 2018) or to recover the GC's mass distribution (Hoekstra et al., 2013). This technique has the advantage of being able to track the total GC mass, including the DM halo which is its major component (Clowe et al., 2004, 2006; Ma et al., 2010; Gonzalez et al., 2015).

Following a hierarchical formation scenario with a cold dark matter cosmology (ACDM), GCs evolve through a sequence of mergers and accretion of smaller systems (Kravtsov and Borgani, 2012). In fact, minor merger events are the dominant growth mechanism for large-scale structures in the Universe; most GCs accrete substructure of around ~10% of their total mass at any given time (e.g., Powell et al., 2009). However, when GC's components are in dynamical and hydrostatic equilibrium we say that the cluster is virialized (that follows the Virial theorem, e.g.; Xu et al., 2000), and enters into a relaxation state. Nevertheless, as mentioned above, this state of dynamical equilibrium can be perturbed due to accretion of other small systems or a merger with another system of similar mass.

1.2 Interaction of galaxy clusters

Massive GC mergers are the most energetic events since the Big Bang with energies ranging up to $\sim 10^{64}$ ergs, where $\sim 10\%$ of the energy is dissipated into the ICM through shock waves, compression, and turbulence (Sarazin, 2002, 2004). These characteristics provide access to an environment with extreme conditions which allows for the study of a range of phenomena, from particle physics, as they can be used to constrain the dark matter particle self-interaction cross-section (e.g., Harvey et al., 2015; Wittman et al., 2017; Fischer et al., 2021); to cosmology, where they can provide constraints to dark energy models (e.g., Thompson et al., 2015; Bouillot et al., 2015). Signals of cluster-cluster interaction remain detectable even in more evolved systems, imprinted for example in the dark matter (e.g., Tam et al., 2020) and the gas components (e.g., Ueda et al., 2020).

When analyzing GC mergers, cluster galaxies can be considered as point particles moving at high velocities with a low probability of collision while, on the contrary, the ICM gas is expected to slow down and lag behind the collisionless components (Pizzolato and Soker, 2010; Massey et al., 2011). In fact, in mergers of GCs with similar masses, cluster galaxies will follow the established merger collisionless course while the collisional ICM gas will be slowed down and exhibit

ram-pressure processes and heating. This will generate a displacement between both components during the collision. In this cases, the center of the DM component, which represent the bulk of the total matter, is found to be displaced from the X-ray emission gas and galaxies (Clowe et al., 2004), and this displacement from galaxies is likely to be much smaller for minor merger events (Massey et al., 2011, also see Fig. 1.1). This phenomenon will generate a projected separation between the BCG and X-ray emission peak/centroid of the GC (denoting concentration of the ICM, e.g., Clowe et al., 2004; Mann and Ebeling, 2012a) which can be partial (e.g., Monteiro-Oliveira et al., 2017) or total (e.g., Clowe et al., 2004).

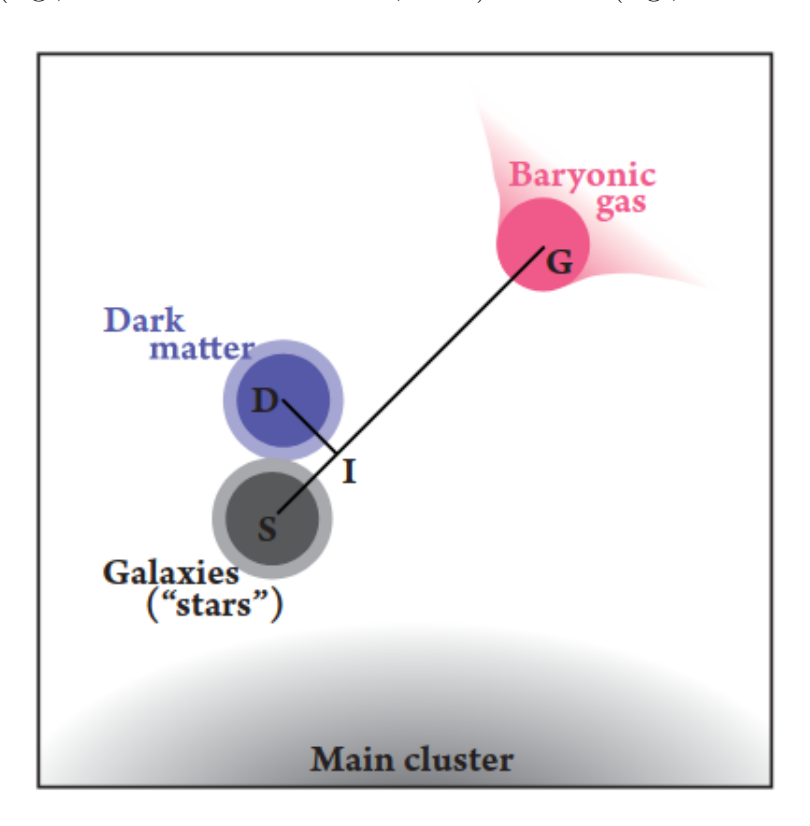


Figure 1.1: Figure from Harvey et al. (2014) illustrating all three components of an infalling structure to the main cluster. The notation is G for gas, D for DM, I for the intersection point closest to the DM in the direction towards the gas, and S ('stars') for galaxies.

Merging clusters also play a role in galaxy evolution. As clusters merge, galaxies in the GCs are subject to extreme ram pressure and such effects can be seen most beautifully in jellyfish galaxies (Owers et al., 2012; McPartland et al., 2016; Poggianti et al., 2016; Roberts et al., 2021). Although jellyfish galaxies (see Fig. 1.2) are examples of extreme galaxy evolution, changes in the overall galaxy populations during mergers are subtle but may be significant enough for detection.

For instance, some systems show a trend for a merger-induced triggering in their star formation (e.g., Stroe et al., 2017; Hernández-Lang et al., 2021), although for others no chance has been found (e.g., Mansheim et al., 2017). Also intriguing, Kelkar et al. (2020) found both scenarios in Abell 3376. After segregating the merger effects from those due to the primitive cluster environment, they found passive spiral galaxies in the central regions, resembling vestiges of a relaxed cluster environment evolution. Meanwhile, post-starburst galaxies evidenced a rapid evolution due to shock-induced star formation or intense surges in the ICM pressures at early stages of the merger. Nevertheless, their pilot study should be applied to a larger number of disturbed systems to generalize (or not) these findings. In this sense, the construction of a large sample of disturbing clusters encompassing several merger configurations (e.g. mass ratios, redshifts) and stages (i.e. time since/to collision) is vital for the goal of performing a comparative study of the merger impact on galaxy properties. Currently, studies over samples of merging clusters with high quality HST imaging range from a few dozens (≈ 30 ; e.g., Harvey et al., 2015), to up to thousands of them when large surveys are used $(\approx 2,000; \text{ e.g.})$, Wen and Han, 2015; Yuan et al., 2022), but only a small fraction of them, if any, had their kinematics addressed in fully details, be through hydrodynamical simulations (e.g., Chadayammuri et al., 2022), identification of shock features (e.g., Cho et al., 2021), or a semi-analytical treatment (e.g., Dawson, 2013; Hernández-Lang et al., 2021).

The classification of the cluster dynamical state has been done using the shape of the red galaxy distribution (Wen and Han, 2015), the X-ray morphology (e.g., Nurgaliev et al., 2017; Lovisari et al., 2017; Yuan and Han, 2020; Yuan et al., 2022), the BCG-gas offset (Lopes, 2007; Mann and Ebeling, 2012b; Zenteno et al., 2020), the radio emission (Osinga et al., 2021; Cuciti et al., 2021), the comparison among different mass estimators (weak lensing, X-ray, SZ, dynamics; e.g., Soja et al., 2018; Monteiro-Oliveira et al., 2021), hydrodynamical simulations (e.g., Lourenço et al., 2020; Doubrawa et al., 2020; Moura et al., 2021), and spectroscopy (e.g., Ferrari et al., 2005; Sifón et al., 2015; Balestra et al., 2016). This last method is an important probe of the cluster disturbance level as it provides spectroscopic properties of the sample of galaxy members such as their line-of-sight (LoS) distribution. As the merger goes on, it leads to a rearrangement of the cluster internal energy that turns into a more enhanced effect near to the pericentric passage (e.g., Pinkney et al., 1996; Monteiro-Oliveira et al., 2022). Understanding how the boost

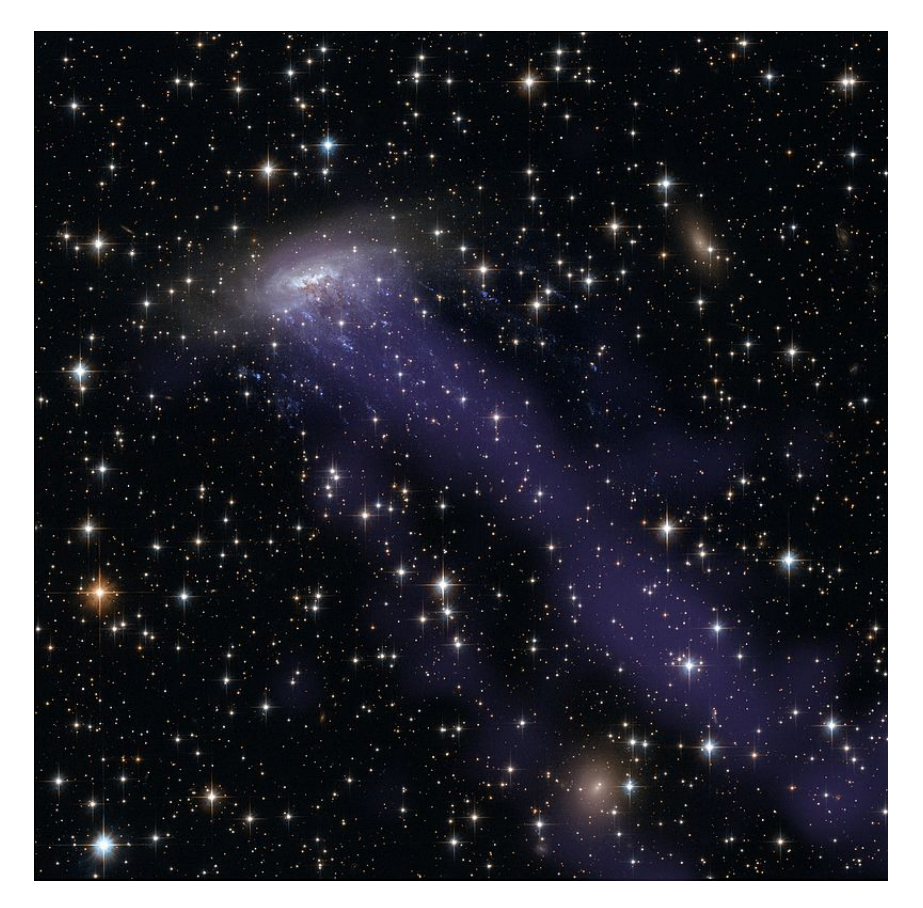


Figure 1.2: Ram pressure stripping of gas from a galaxy in ESO 137-001 in the Norma cluster. Image taken with the HST.

on the cluster's velocity dispersion varies with the time to/since collision, viewing angle, and other merger configurations not only provides an important tool to estimate the merger age (through the comparison with non-biased weak lensing masses; e.g., Monteiro-Oliveira et al., 2018) but also to identify merger candidates through statistical methods (e.g., A. Knebe & V. Muller, 1999; Hou et al., 2009), or by using up to date machine learning techniques (e.g., de los Rios et al., 2016).

Spectroscopic classification of the dynamical state of GCs involves the use of the shape of the velocity profile to separate relaxed from unrelaxed clusters. This is done by exploiting the fact that the velocity distribution of dynamically relaxed clusters show a nearly Gaussian distribution (Beers et al., 1990; Finn et al., 2008). Any departure from such distribution would indicate a perturbation in the cluster dynamical state. Thereby, is common to use statistical tests to compare the cluster velocity distribution to a Gaussian distribution. For example, Hou et al. (2013) classified the dynamical state of galaxy groups from different catalogs in the range

 $0 \le z \le 1$ by using the Anderson-Darling (AD) test. Hou et al. (2013) used the AD tool to probe the hypothesis that the group's velocity distribution is drawn from a Gaussian distribution. Hou et al. (2013) found no significant correlations between the dynamical state of the groups and the fraction of non-star-forming galaxies. The AD test was also used by Bayliss et al. (2016, B16 hereafter) to estimate the probability for 62 GCs velocity distributions, in the redshift range 0.3 < z < 1, to be non-Gaussian. Sifón et al. (2015), using the spectroscopic information of 90 GCs in the redshift interval 0.05 < z < 0.55 and the Dressler-Schectman test (DS, Dressler and Shectman, 1988) to select relaxed and unrelaxed GCs based on the position and the galaxy velocities to find sign of substructures, find that there was no correlation between alignments of the member galaxies dynamical state of GCs. Ribeiro et al. (2013), using spectroscopic information of 146 GCs classified as disturbed and 27 GCs classified as relaxed, find that GCs with velocity profiles deviated from a Gaussian distribution (i.e. unrelaxed) have luminosity functions with fainter characteristic magnitude m^* and shallower slopes compared to the GCs with Gaussian velocity profiles (i.e. relaxed). In this scenario a fraction of the faint galaxies are formed in the relaxed clusters, possibly by transforming brighter late type galaxies into dwarf galaxies (Zenteno et al., 2020).

It is important that samples of merger candidates should be identified using a set of proxies (i.e. using several statistics to classify the dynamical state in multiple dimensions; e.g., Pinkney et al., 1996) and to facilitate the comparison to simulations, the sample of confirmed mergers should be mass limited, nearly redshift independent, and statistically significant.

The South Pole Telescope (SPT) SZ survey is an ideal sample for the study we want to pursue. This survey accounts for 1,202 cluster candidates detected, from which there are 760 confirmed GCs (Bleem et al., 2015, 2020, 2022). Zenteno et al. (2020, Z20 hereafter) studied the impact of the dynamical state of clusters on 288 SZ-selected GCs detected by the SPT, finding differences between the overall cluster populations between the most relaxed and most disturbed systems. In Z20, most of the classification of merging clusters was done using the offset between the gas (measured by the SZ or X-ray centroid/peak) and the collisionless component traced by the BCG. Z20 found that clusters, irrespective of their dynamical state, have a consistent faint end slope luminosity function (LF) up to $z \sim 0.55$. At $z \geq 0.55$ disturbed clusters exhibit a steeper slope with respect to the relaxed sample while no difference was found at lower redshifts. This result is consistent

with a scenario where the fainter galaxies are brought in by mergers (steeping up the LF faint end) and, as the clusters relax, they are destroyed and/or transformed. At the same redshift range, Z20 found that relaxed clusters exhibit a fainter m^* , which could be due to a more efficient dynamical friction at z>0.6, enhancing the accretion of bright neighbouring galaxies by the BCG. This picture is consistent with the finding that BCGs in relaxed clusters at $z \gtrsim 0.55$ exhibit an excess brightness when compared to BCGs from the disturbed and general cluster populations. The characterization of the dynamical state of clusters is then indispensable to understand the evolutive processes of galaxies there in and having a large sample of these systems is essential for the development of this research field.

1.3 Cluster sample and thesis goals

Here we analyze 15 GCs with Gemini/GMOS spectroscopic data in the redshift range 0.3 < z < 0.7, including 14 classified as merging cluster candidates by Z20. This sample consists in SZ-selected and optically-confirmed clusters at signal-to-noise>4.5(5) which can be considered as approximately mass selected with a nearly redshift independent mass threshold of $M_{200} > 4 \times 10^{14} \text{ M}_{\odot}$ (Bleem et al., 2015).

The sample has optical imaging in the DES survey² which comprises nearly $5{,}000~{\rm deg^2}$ of grizY imaging in the south Galactic cap, including nearly 390 million objects, with depth reaching a signal-to-noise ratio ~ 10 for extended objects up to $i_{AB} \sim 23.0$ (Sevilla-Noarbe et al., 2021). In addition to select the BCG candidates for the clusters, Z20 calculated M_{200} and R_{200} from the SZ based M_{500} published in Bleem et al. (2015). Bleem et al. (2015) also estimated photometric cluster redshifts by searching for a redshift with a clear excess of galaxies near the candidate position that are consistent with the expected red sequence.

In this thesis we use spectroscopic data to confirm the dynamical state of the clusters by analyzing multiple proxies, measure the dynamical cluster masses, and classify the membership of candidate BCGs. In addition, we take 123 GCs from

 $^{^{1}}M_{200}$ is the mass contained inside a sphere of radius R_{200} with average mass density equal to 200 times the critical density of the universe. Being R_{200} the radius at which the sphere account for that density.

²https://www.darkenergysurvey.org/des-year-3-cosmology-results-papers/

literature with available spectroscopic data to amass a large sample of clusters and run our tests.

This thesis is organized as follows, in Chapter 3, the observation design, data reduction, and spectroscopy are described. Other sources and samples used in the study are detailed too. Chapter 4 is then dedicated to explain the techniques to find cluster redshifts and dynamical masses, describe our galaxy membership selection, and describe the methods to classify the dynamical state of the clusters. In Chapter 5 we report our estimations and BCG membership for each cluster. Also, dynamical state results on the clusters are presented here. Finally, Chapter 6 contains the discussion and conclusions on the results together with numerical simulations and the application of our tests to the other samples from literature.

We use Bocquet et al. (2015) cosmology assuming a flat Λ CDM cosmology with $H_0 = 68.3 \text{ km s}^{-1} \text{ Mpc}^{-1}$ and $\Omega_{\text{M}} = 0.299$.

Chapter 2

Objectives

In this thesis we analyze spectroscopic data of 15 GCs, 14 of which are candidates to disturbed clusters, taken with the GMOS spectrograph in the Gemini South telescope. We analyze the dynamical state of the clusters by using statistical tests to probe the distribution of spectroscopic members in the GCs. These tests probe the LoS and spatial distribution of the GCs. In the process, we estimated dynamical masses and find the BCG membership status for each GC in our sample. Finally, using 123 GCs collected from literature, we amass a large sample of clusters and run our dynamical tests. To achieve this, a series of specific objectives were developed:

- Estimate the clusters redshift, velocity dispersion, and dynamical mass.
- Confirm the BCGs membership by estimating their peculiar velocities to their respective clusters.
- Analyze the dynamical state of the clusters by using different statistical techniques to probe their distributions in 1, 2, and 3 dimensions.
- Discuss the tests outcome by simulating merger scenarios to test the robustness of the statistical techniques.
- Employ the statistical techniques over a large sample of GCs with public available spectroscopic data.

Chapter 3

Data

3.1 Selection of the Merging cluster candidates and the Galaxies for spectroscopy

The cluster data set used in this work correspond to 43 disturbed cluster candidates from the Z20 sample. From the original 43 disturbed cluster candidates, 22 systems in the redshift range between 0.3 < z < 0.7, were visually selected due to their high asymmetric red sequence galaxy distribution to be observed. From those 22 we obtained data for 14 of them plus SPT-CLJ2100-5708, a cluster classified as disturbed in early versions of Z20 but which was discarded in later iterations. By the time the observations were made all the clusters were candidate to disturbed clusters. As an example, Figure 3.1 shows the projected density contours (from the red cluster sequence galaxies) overlaid on the DES i-band images (top panel) and the color-magnitude diagram (bottom panel) for the unrelaxed cluster SPT-CLJ0522-5026 at z = 0.52 selected from Z20. The galaxy distribution in the region defined by the linear color-magnitude relation for early-type galaxies (the red cluster sequence, RCS) was used to select clusters with clearly spatially recognizable substructures (top panel in Fig. 3.1) to improve the chance to assess the cluster's dynamical state, especially in cases where the collision is nearly in the plane of the sky (Clowe et al., 2004, 2006).

The galaxies are selected by fitting the RCS created from a passive evolving stellar population synthesis model (Bruzual and Charlot, 2003) at the clusters redshift¹, and adopting a RCS width of ± 0.22 mags (or 3σ , López-Cruz et al.,

¹Estimated as "optical" redshifts by Bleem et al. (2015), section 5.2 in there

2004) from the RCS best-fit. This is done by using catalogs created by the Dark Energy Survey (bottom panel in Fig. 3.1).

The exposure time and the number of masks were designed to have enough cluster members to be able to detect a major merger. The number of cluster galaxies are estimated by simulating two overlapping clusters with the same mass, represented by two Gaussian distributions, with a large velocity separation. Both Gaussian distributions have velocity dispersions of $\sigma=1,000~{\rm km\,s^{-1}}$ and are separated by 3,000 km s⁻¹. After applying an Anderson-Darling normality test, this simulation finds that 50 randomly selected galaxies are needed to confirm that they are not drawn from the same Gaussian distribution to a 90% confidence level. Furthermore, by targeting RCS galaxies, B16 showed that there is a 60% probability that the selected targets are actually part of the cluster. This sets the minimum number of galaxies needed per cluster to establish the cluster dynamical state to ~ 80 . The required depth to obtain ~ 80 cluster galaxies can be estimated by integrating the luminosity function (e.g., Zenteno et al., 2016; Hennig et al., 2017). This shows that to find ~ 80 galaxy members for a cluster with a typical SPT $M_{200,c}$ mass $(5 \times 10^{14} M_{\odot})$, magnitudes of m^*+1 mag are required, corresponding to an apparent magnitude of r = 20.5 AB mag at z = 0.3 and r = 23.0 AB mag at z = 0.7.

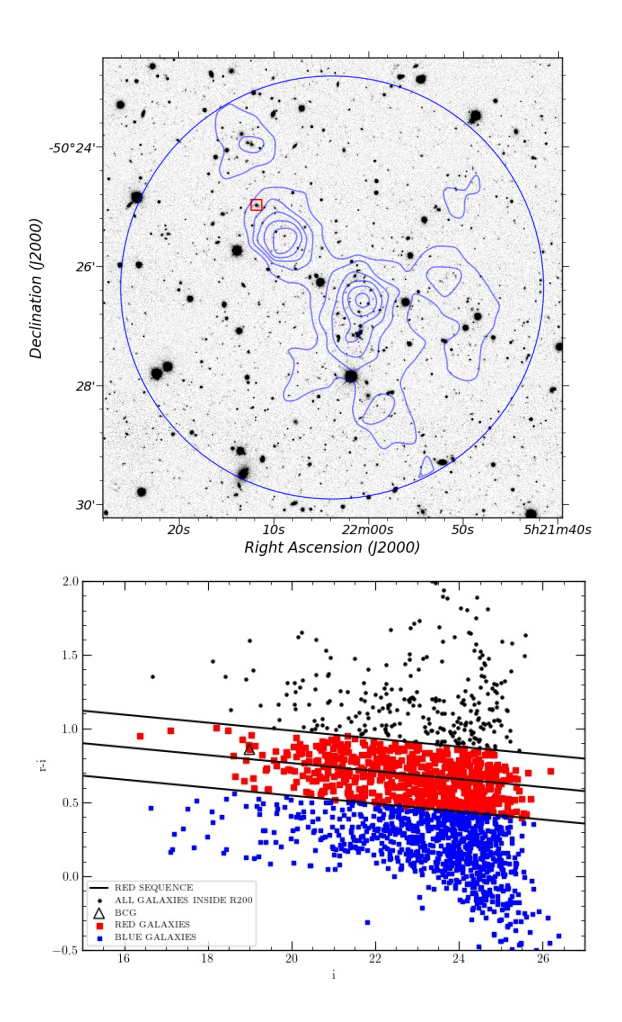


Figure 3.1: Top panel: Projected density contours (from the RCS galaxies) overlaid on the DES i-band images for the unrelaxed cluster SPT-CLJ0522-5026 at z=0.52. Levels begin at 100 galaxies ${\rm Mpc^{-2}}$ and increase linearly with increments of 50 galaxies ${\rm Mpc^{-2}}$. The field-of-view of the image is 7.7×7.7 arcmin² ($\sim 2.9 \times 2.9$ Mpc² at the redshift of SPT-CLJ0522-5026). Note the two clear separate structures in SPT-CLJ0522-5026 (separated by ~ 0.8 Mpc). Other over densities are detected and possible connected to the cluster. The red square shows the BCG location. The large blue circle indicates the radius R_{200} . Bottom panel: Color-magnitude diagram for SPT-CLJ0522-5026 with the total (black dots), blue (blue dots), and red-sequence (red dots) galaxies within R_{200} . The lines correspond to the best fit of the model ± 0.22 mags.

3.2 Mask design and Observations

Optical imaging and catalogs with accurate equatorial coordinates (0.1" or better) are crucial to create multi-object spectroscopic (MOS) masks. Images and catalogs from the Dark Energy Survey were used (propid 2012B-0001; PI Friedman). Where the images, covering the area from which the target lists are extracted, were downloaded from the DES cutout service² while catalogs were downloaded using an SQL service (see appendix A.1). Targets galaxies were selected within ± 0.22 mags from the RCS best-fit. Since ~ 80 targets per cluster were observed, two masks per cluster are required. Therefore, the masks have to be aligned with the projected merging axis indicated by the red galaxy distribution to allow the highest number of slits in the mask (see app. A.2).

The IRAF task gmskcreate, from the Gemini-GMOS package, is used to create the object table (OT) needed to proceed with the mask's design. The input file for gmskcreate contains the ID, the equatorial coordinates (RA, DEC) and the magnitudes of the galaxies, which are mandatory. We also include other optional parameters such as the priority, slit width, and the slit length. In addition, the positions and magnitudes of three point sources (stars) carefully selected are included in the list. These stars are used to align the masks on the sky and are carefully chosen to maximize the number of galaxies in the masks. Each OT contains the information about the coordinates of targeting galaxies, the magnitudes, the slit width and the slit length to be used, the X and Y position on the pre-imaging (the DES images), a priority flag (from 1 to 3, for high to low priority targets, respectively), and the information about three stars to be used to align the masks on the sky.

Once gmskcreate step is completed the Gemini MOS Mask Preparation Software (GMMPS) tool is used taking as input the OT and the pseudo-images³. GMMPS allows to set three priority levels for the catalog objects, based on the magnitudes of the objects. Based on that priority system, it creates an "object definition file" (ODF), which is the final mask design⁴. More priority is given to brighter objects: High priority (flag 1) for galaxies with magnitudes between

²https://deslabs.ncsa.illinois.edu/desaccess/

³The DES images are transformed by GMSKCREATE into a pseudo-image, mimicking a GMOS pre-image. The images are used to inspect the mask design.

⁴For detailed information and step by step instructions on the mask design see https://gmmps-documentation.readthedocs.io/en/latest/index.html

 m^* and $m^* + 0.5$; Medium priority (flag 2) for galaxies with magnitudes between $m^* + 0.5$ and $m^* + 1$; Low priority (flag 3) for galaxies with magnitudes between $m^* + 1$ and $m^* + 1.5$. Finally, if space is available in the masks, suitable galaxies are selected manually to fill empty spaces in the mask with slits. When selecting targets for the second mask, the majority of targets were already selected for the first mask and there was a low number of available targets for the second mask. In this case, if there are no target candidates available near an empty space, targets selected for the first mask are used to fill that empty space. This produce that a single source may have repeated spectroscopic data taken with both masks. These "paired" spectra from the same sources are latter used for uncertainty statistics. Finally, each mask has 45 objects and the final designed masks, the ODFs, are then sent to the observatory for masks cutting. These observations were carried out with the Gemini Multi-Object Spectrograph (GMOS) mounted on the Gemini South telescope (program prop-id GS-2018B-Q-233 Band 3, PI: A. Zenteno), between October 6th, 2018 and February 6th, 2019. By the end of the 2018B semester, 15 clusters were observed.

All masks were observed during dark/gray time, with a good transparency, and with a seeing between 0.9" and 1.3". The total exposure times used depend on the redshifts of the clusters and varied between 900s (3 \times 300s) for clusters with 0.3 < z < 0.35 up to 3600s (3 \times 1200s) for clusters with 0.55 < z < 0.66. All spectra were acquired using the 400-lines per millimetre ruling density grating (R400), 1" slitest, 2 \times 2 binning, and central wavelengths between 6800 Å to 7800 Å. The central wavelength used varies according to the redshifts of the clusters to maximize the wavelength coverage. Offsets of 80 Å in the spectral direction toward blue and red were applied between exposures to allow for the gaps between CCDs and to avoid any lose of important emission/absorption lines present in the spectra. For each mask a set of spectroscopic flats and CuAr comparison lamps spectra for wavelength calibration were obtained before or after each science exposure. In addition, the spectrophotometric standard star CD-34 241 was observed using the same configuration as the science images to relative flux calibrate the spectra.

3.3 Data reduction

The observed spectra were reduced using the Gemini GMOS package version 1.14. following the standard procedures for MOS observations. The reduction process begin with the bias subtraction. Calibration files were chosen to match the science images' observation date, including data from the previous and the following night. Using 15 bias files a master bias is created using the task *gbias*. The master bias file is then applied to all the science images, the CuAr lamp images, and the spectroscopic flats and then they are trimmed with the task *gsextract*. Both masks in a cluster use the same master bias unless they had been observed with more than three days apart. Before subtracting the bias is necessary to replace pixels with wrong values (i.e. correction of bad pixels).

Then, the task gswavelength is used to establish the wavelength calibration using the GMOS CuAr comparison lamps based on a pre-identified list of lines from the GMOS package. This task automatically identify the lines, establish the wavelength calibration for all spatial points, remove the no-linear components, and generate a database with the correction to be done to remove the S-shape distortion presented in the 2D slits. In some cases gswavelength fails to fit the lamp's spectra to the database and the spectral lines have to be identified visually, using a reference plot available in the Gemini web page⁵. The final wavelength solution has an average residual values (rms) of ~ 0.20 - 0.25 Å.

Next, the task *gsflat* is used to process the spectroscopic flats for each wavelength setting. This task remove the calibration unit plus GMOS spectral response and the calibration unit uneven illumination, normalizing and leaving only the pixel-to-pixel variations.

The following step is to apply quantum efficiency (QE) corrections to science and flat-field images using the task *qecorr*. This is needed to correct the relative difference in QE between the GMOS CCD2 and the other 2 CCDs. After normalizing the flats by QE corrections, the task *gsreduce* is used to flat-field the QE corrected science images. After this step, bad pixels are interpolated and images are cleaned from cosmic rays using the *lacos_spec* script⁶.

The resulting two-dimensional science spectra are then wavelength calibrated

 $^{^5\}mathrm{Arc}$ lamp line plots and lists <code>https://www.gemini.edu/observing/resources/near-ir-resources/spectroscopy#Wavelength</code>

⁶astro.yale.edu/dokkum/lacosmic

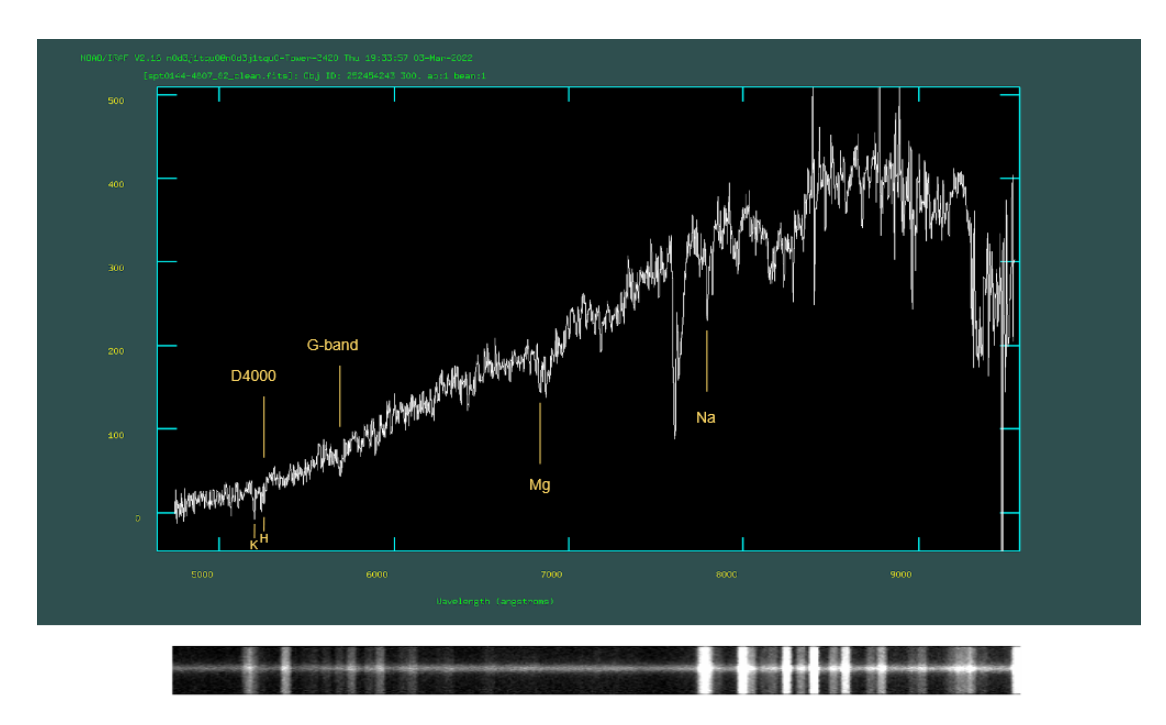


Figure 3.2: Obj ID: 252454243, slit number 32, second mask for SPT-CLJ0144-4807. 1D spectra shown using splot and 2D spectra displayed with SAODS9. Highlights indicate some visually identified absorption lines.

and corrected by the S-shape distortion using the task gstransform, sky-subtracted using the task gsskysub, and combined using the task gemcombine. The spectra in the 2D combined science images are then extracted to a one-dimensional format with the task gsextract using a fixed aperture of 1.4". The same procedure is used to reduce the spectrophotometric standard star CD-34 241. The 1D-spectrum of the standard star is used to determine the sensitivity and extinction functions using the task gsextract. Finally, the task gsextract is used to calibrate in flux and correct by extension the 1D-extracted GMOS spectra. With the choice of 1" slit width, the spectra have a resolution of \sim 7 Å (measured from the sky lines FWHM), a dispersion of \sim 1.5 Å pixel⁻¹, and a wavelength coverage between \sim 5,000 Å - \sim 10,000 Å. Fig. 3.2 shows an example of the data reduction products, a 1D and 2D spectra. The final sample consist of 1334 spectroscopic sources.

3.4 Spectroscopy

3.4.1 Spectra treatment before redshift measurement

Before measuring redshifts from the spectra we remove sky-line residuals, bad pixels contaminants and odd behaviors to reduce any chance of confusion when identifying spectral features. First, we use the IRAF package LINECLEAN to replace anomalous pixels in the 1D spectra by fitting a one dimensional Chebyshev function of order 13 to the continuum (see Fig. 3.3). This will reject any data point outside 2.5σ in the selected region of the spectra and replace it with the value of the fit. This task should be used with great caution, inspecting interactively each routine step to select precise regions of the spectra to alter, otherwise the continuum fit can delete good data from feature lines. We refer to Wells and Bell (1994) for proper indications on how to use the LINECLEAN interactive interface.

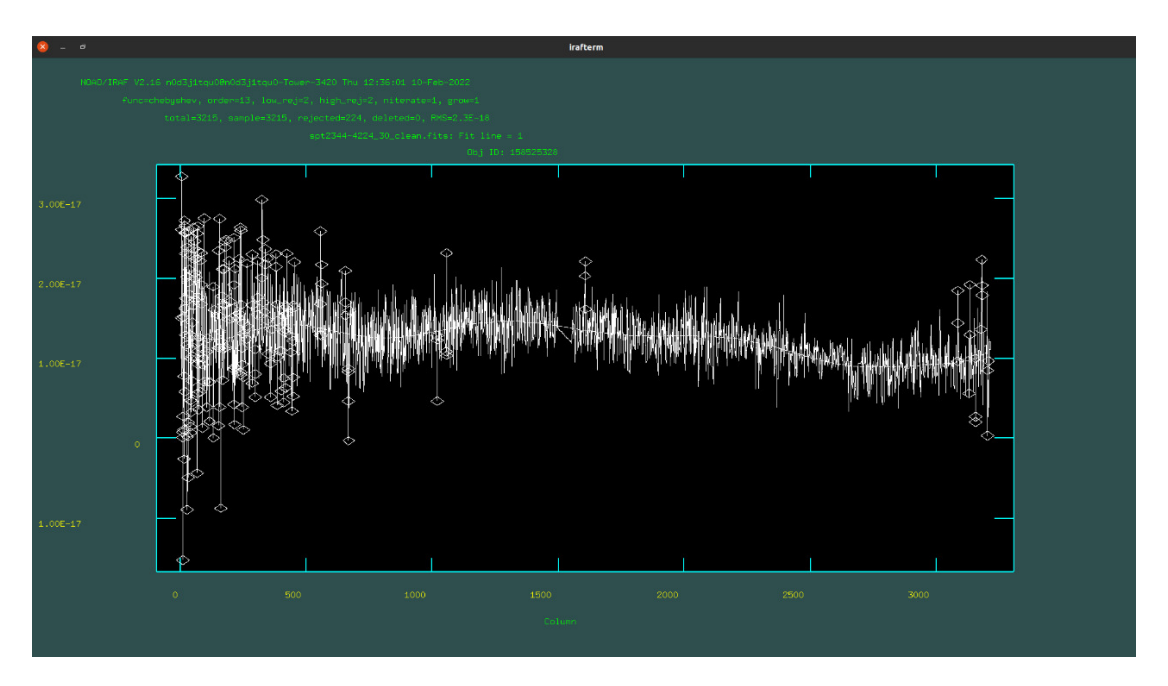


Figure 3.3: LINECLEAN interactive panel example. Obj ID: 158525328, slit number 30, first mask for SPT-CLJ2344-4224. The figure shows the flux calibrated 1D spectra. The central curve is the order 13 Chebyshev fit to the continuum.

While using LINECLEAN, we also identify and reject spectra corresponding to stars or galaxy spectra with too low signal-to-noise (see Fig. 3.4). At this point, we exclude 192 sources yielding 1142 spectra to process.

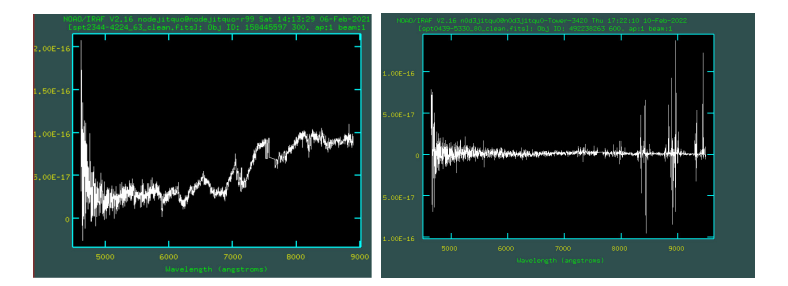


Figure 3.4: An example of a star and a low-signal spectra.

We then remove prominent sky features that populated the spectra. In particular, the OH line at 7620Å presented in all the spectra (see Fig. 3.5). The line is removed by replacing the region between 7580Å to 7670Åwith a 1D linear function connecting the first and last data point in the section. This task is performed using routines from astropy⁷.

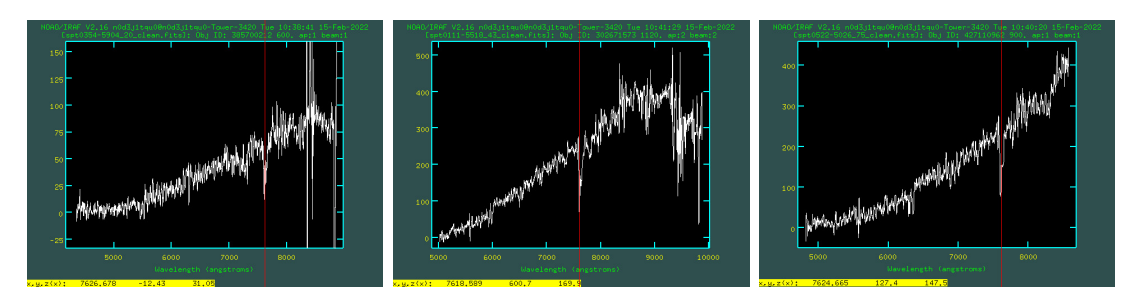


Figure 3.5: Spectra of sources from different clusters denoting the presence of the OH line at 7620Å line.

Once the treatment of the 1D spectra is completed, we proceed to measure redshifts for the final sample of 1142 galaxy spectra.

3.4.2 Redshift measurements using FXCOR

To obtain redshift estimations we use the IRAF task fxcor inside the package RV. This task makes a cross-correlation between the object and a series of template spectra yielding the velocity shift (corrected by heliocentric motion effects), the velocity error (as independent estimation in km s⁻¹), and the R-value as a reliability parameter of the cross-correlation (Tonry and Davis, 1979). For detailed information on fxcor we refer to Alpaslan (2009) where the complete usage instructions are described.

⁷https://docs.astropy.org/en/stable/io/fits/index.html

To process the spectra, fxcor (along with many other parent programs such as RVIDLINE or XCSAO) requires specific headers to make the heliocentric calculations. We check that the headers include the following parameters:

- RA, DEC: Right Ascension and Declination of the Target
- UT, UTSTART, UTOPEN: UT at observation start
- UTEND: UT at observation end
- UTMIDLE: UT during half the observation
- EXPTIME: Exposure time in seconds
- EXPOSURE: Requested exposure time in seconds
- EPOCH: Epoch of target coordinates
- EQUINOX: Equinox coordinate system
- DATE-OBS: UT Date of observation (YYY-MM-DD)
- ST: Sidereal time at the start of the exposure
- AIRMASS: Mean airmass for the observation
- OBSERVAT: Name of telescope (Gemini-North—Gemini-South)
- JD: Julian date
- HJD: Heliocentric Julian date
- LJD: Local Julian date keyword
- SITELONG: Observatory longitude
- SITELAT: Observatory latitude
- SITEELEV: Observatory elevation

fxcor allows the use of multiple templates to cross-correlate with the observed spectra. We use three templates from the IRAF package rvsao; eltemp and sptemp, which are composites of elliptical and spiral galaxies, respectively; and habtemp which is a composite of absorption line galaxy at z=0. The first two were produced with the FAST spectrograph for the Tillinghast Telescope (Fabricant et al., 1998a) while habtemp was produced with the HECTOSPEC spectrograph for the MMT (Fabricant et al., 1998b). Additionally, we use a synthetic galaxy template syn4 from stellar spectra libraries constructed using stellar light ratios (see section 3 in Quintana et al., 2000, for details). Fig. 3.6 show the 1D spectra of the templates. Our spectroscopic methods will assume that line features in them can be found in the spectra of galaxies with a certain signal but shifted to larger wavelengths.

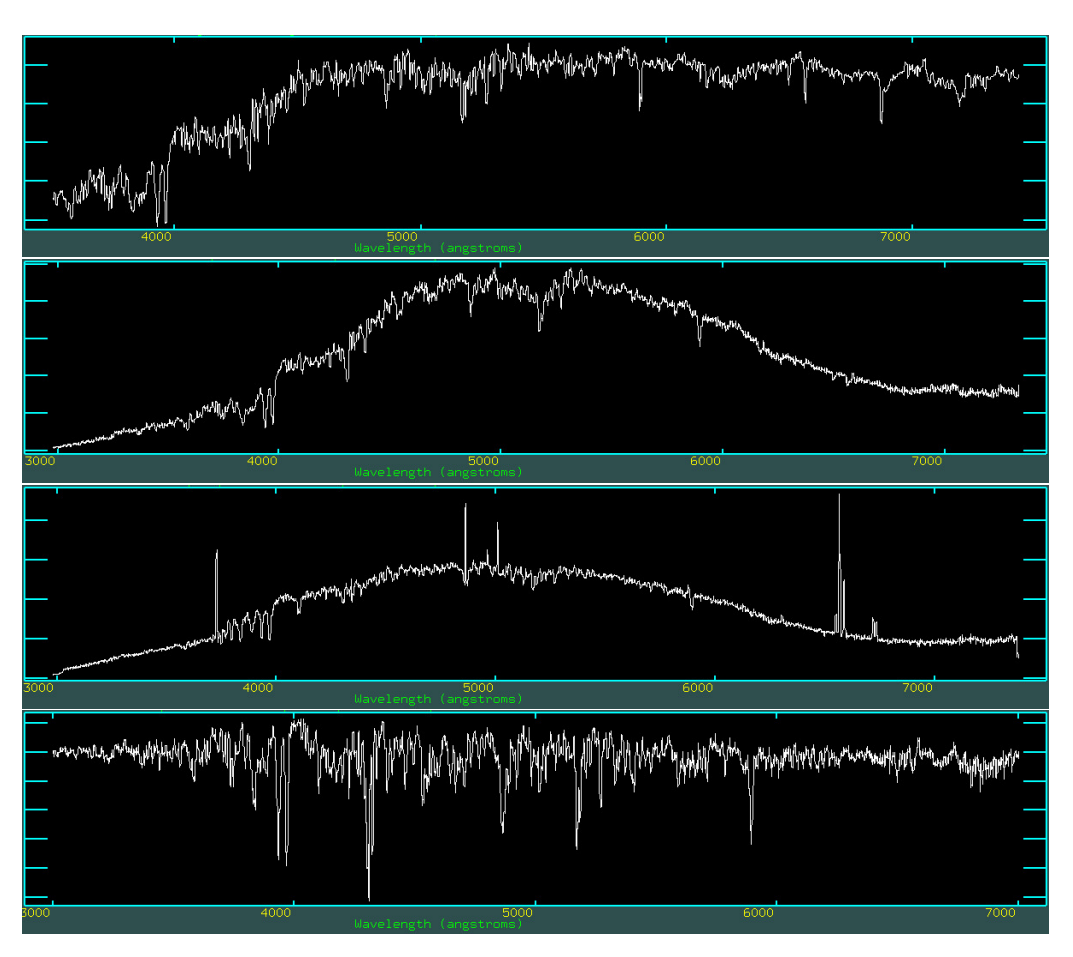


Figure 3.6: Template spectra listed from top to bottom are syn4, eltemp, sptemp and habtemp.

Since we use several templates and the sample has a large range of redshifts,

to obtain reliable redshifts we use a custom pipeline to obtain redshift estimations based in the fxcor task and its input parameters. Specifically, fxcor allows to indicate the sections of template and object spectra to be correlated (see Fig. 3.7). These parameters are respectively rsample and osample and they will be the main focus of our custom pipeline to extract redshifts autonomously.

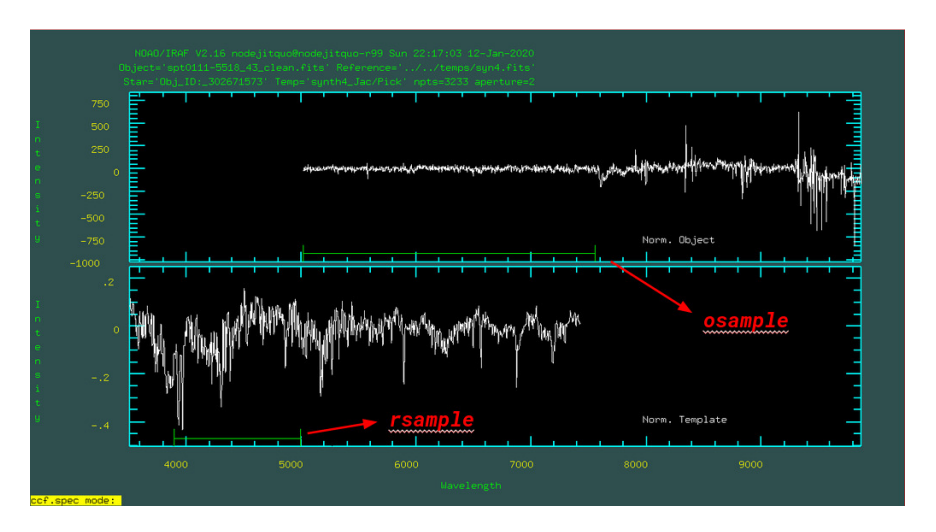


Figure 3.7: Example of the interactive spectrum mode of fxcor. The top panel shows the spectra of a galaxy from SPT-CLJ0111-5518 while the bottom panel is the *syn4* spectra template. Both spectra have their continuum subtracted. In the interactive mode, the s hotkey can be used to select with the cursor the regions to correlate (the green range line). These are the rsample and osample parameters.

3.4.3 Automated redshift estimation pipeline

For a single spectra, we estimate 4 velocity shifts corresponding to the cross-correlation with each of the 4 templates. Over these measurements we take the following considerations to obtain a velocity shift:

- Three or more templates have to agree in the heliocentric velocity within a range of ± 100 km s⁻¹ from the median of the four templates.
- At least two of these templates have a Tonry Davis parameter $R \geq 5$.
- The velocity error estimation of the templates that met the first condition have to be in the range $5 < \sigma_v < 350 \text{ km s}^{-1}$, otherwise it means that one or more redshift estimations went wrong.

If these conditions are met we take the mean of the heliocentric velocities and the errors of the 3 or 4 templates. This is what we called an *ideal result*.

To obtain a final velocity estimation we run fxcor following a sequence of rounds where different rsample, osample, and prominent spectra features are considered each time (see Table 3.1). This generate a sample of *ideal results* for a single galaxy spectra from where we select the final velocity estimation. The sequence of rounds works as follows: The wavelength ranges in Table 3.1 are used for the rsample parameter to select the section of the template spectra to correlate. The first round 0-A correlates the entire spectrum of object and template spectra. Subsequent rounds then correlate smaller ranges considering less feature lines each time. In practice, we start by performing the 0-A round for all galaxies from the same mask. osample is then calculated from the median heliocentric velocity v_m of the *ideal results* generated. This way, osample = rsample \times (1 + (v_m/c)), where v_m is re-estimated on each round including ideal results posterior to round 0-A.

With the exception of the 0-A round, the entire sequence of rounds is performed three times: Denoted with 'C' for correlations with the osample parameter calculated as if galaxy at the median cluster redshift v_m/c ; 'B' for those correlated as if foreground galaxy, $v_m/c-0.2$; and 'D' for those correlated as if background galaxy, $v_m/c+0.2$. With 10 rounds plus the initial 0-A round, this set the maximum of possible ideal results for a single galaxy to 31. Since early rounds consider more feature lines; 'B', 'C', and 'D' rounds do not differ significantly on their velocity result for a single galaxy. However, late rounds can have difficult times yielding ideal results and their velocity result can differ in many km s⁻¹. In the case of spectra that yields no ideal results, the spectra is checked by eye along with the 4 templates in the interactive mode of fxcor to obtain an estimation following the stated conditions. In many cases, these spectra are classified as a low-signal and are removed from the study sample.

To select the final velocity estimation of an individual galaxy we take the velocity indicated by the most number of *ideal results* for that galaxy. For this, we group these results in bins of 200 km s⁻¹ and take the peak with more results. In some cases, there are many peaks with the same amount of results. The one with the earlier rounds has priority since later rounds consider a lower number of features. With the peak selected, the *ideal result* from the earliest round in that bin is taken as the final result. Cases with no ideal results are solved in interactive fxcor mode. If the conditions for ideal result are met, this is the final velocity. Only a few 4 to 6 galaxies per cluster have to be processed this way and

a total of 12 galaxies is rejected as a low-signal spectra. All these considerations are included in a custom pipeline to extract the heliocentric velocity estimation for the entire spectral sample automatically. The python implementations and scripts that conform this pipeline can be found in a public GitHub repository⁸. The final sample has 1130 galaxies with redshift estimation.

Round^a	rsample	features
	Å	
0-A	all	all
$0-B, 0-C, 0-D^b$	6500-6780	$H\alpha$, [SII]
1-B, 1-C, 1-D	3500-6000	D4000, G-band, Mg, Na
2-B, 2-C, 2-D	3500-5300	D4000, G-band, Mg
3-B, 3-C, 3-D	4200-6000	G-band, Mg, Na
4-B,4-C,4-D	3500-4600	D4000, G-band
5-B, 5-C, 5-D	4200-5300	G-band, Mg
6-B, 6-C, 6-D	4820 - 5920	Mg, Na
7-B, 7-C, 7-D	3800-4400	D4000, G-band
8-B,8-C,8-D	4800-5400	${ m Mg}$
9-B,9-C,9-D	5700-6300	Na

Table 3.1: Sequence of rounds for spectroscopy with fxcor.

Notes. Prominent feature lines: $\text{H}\alpha(6559\text{Å})$, [SII](6717,6731Å), D4000 (Calcium H at 3933Å and K at 3967Å), G-band(4304Å), Mg(5607Å), and Na(5892Å). a. Rounds are accompanied by a letter B, C, or D indicating that the osample parameter is calculated in, before (-0.2) or after (+0.2) the median redshift. b. Rounds 0-B, 0-C, and 0-D accounts for prominent emission lines in our sample. Ideal results from these rounds only consider estimations from the correlation with the sptemp template. This estimation must have $R \geq 15$ and met the velocity errors condition.

To test the effectiveness of this automated redshift measurement we compare the heliocentric velocities obtained for pairs of spectra following the approach of Quintana et al. (2000). In the final sample there is a total of 49 galaxies with spectra observed in two different masks. For these galaxies, we use the heliocentric velocity v and the velocity error σ from both masks to compute $(v_{msk1} - v_{msk2})/(\sigma_{msk1}^2 + \sigma_{msk2}^2)^{1/2}$ to compare the differences between results. In Fig. 3.8 is the distribution and mean statistic of the 49 galaxies. Note that there are some galaxies with discrepancies greater than 100 km s⁻¹. This number of discrepancy cases suggest that $\sim 24\%(12/49)$ of the entire sample exhibit a wrong

⁸https://github.com/NOD3J1TQU0/autofxcor#autofxcor

velocity estimation. In response to this behavior we examined the correlation between the statistic and the i-band magnitude of the sources. Since we manually selected some galaxies to fill the masks while making the ODFs for the mask design (see section 3.2), we lack the DES magnitudes for some galaxies in our catalog. To get these magnitudes we matched our catalogs with the DES catalogs within 1 arcseconds using the package SKYCOORD. Fig. 3.9 show the distribution of this statistic against the i-band magnitudes of the galaxies. As a practical solution, we selected, by visual inspection, limit magnitudes for each cluster (specifically for each exposure time group) for which all the spectra beyond these limits is checked by eye. The selected limit i-band magnitudes are 20.6, 21.4, 21.16, 21.3, and 21.5 for clusters with exposure time of 1.4, 1.6, 2.0, 2.5, and 3.1 hrs, respectively.

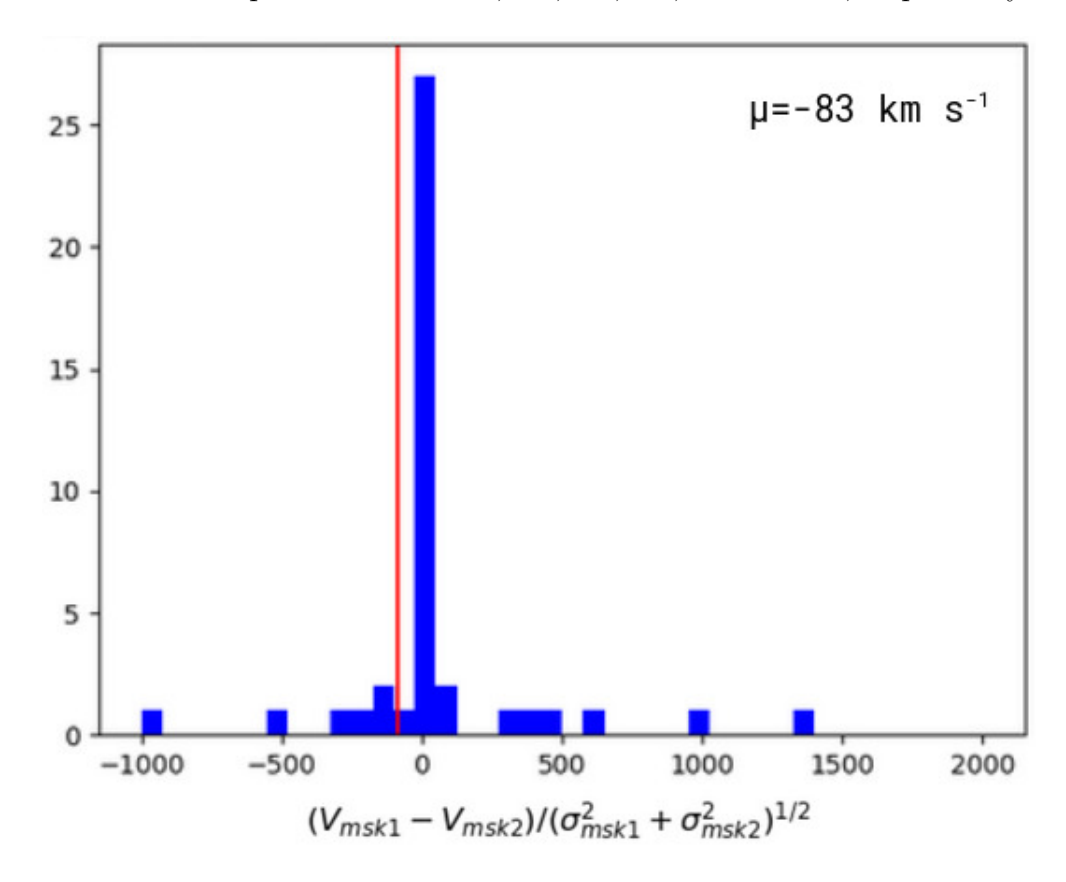


Figure 3.8: Histogram of residual of the heliocentric velocities normalized by the quadratic errors for the 49 galaxies observed in two different masks. The *red solid line* indicate the mean value of the distribution. The histogram shows the distribution from -1,200 to 2,200 km s⁻¹.

After this process a total of 260 velocity shifts are re-estimated interactively where all of these yield a velocity shift estimation. The final sample, keeping first mask spectra in the cases of spectra pairs, has a total of 1081 galaxies with

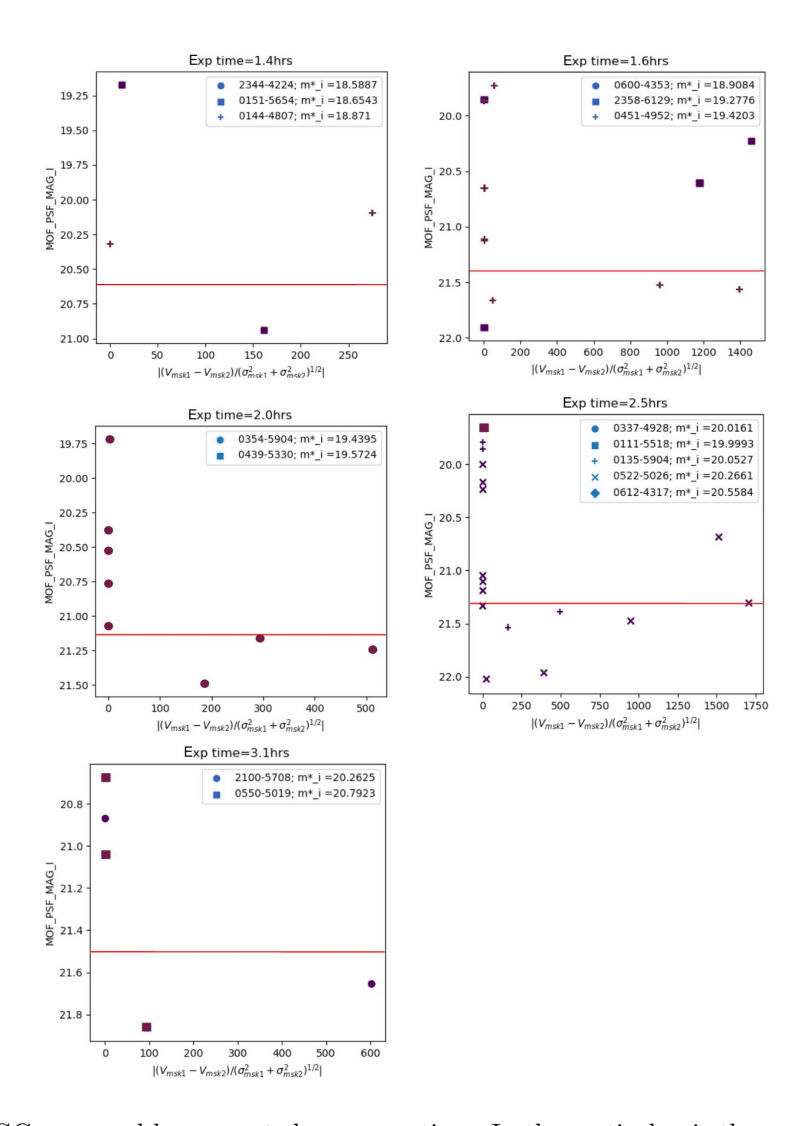


Figure 3.9: GCs grouped by requested exposure time. In the vertical axis the apparent magnitudes in the i band (taken from DES survey) and the horizontal axis shows the absolute value of Quintana et al. (2000) statistic. In the legend is also the characteristic i-band magnitude of the clusters. The red line indicate the selected limit magnitude at which fainter galaxies' spectra is inspected visually and redshifts are estimated interactively.

estimated heliocentric velocities. The mean number of galaxies assigned to each cluster is 72 ± 10 . Finally, a 15.3% of the total observed spectra have to be removed (by low signal or star spectra) from the sample.

3.5 Data from literature

In addition to the parent sample, we collected a total of 123 GCs that have public spectroscopic data. This dataset includes 62 SPT GCs, in the redshift range 0.3 < z < 1, from B16, with a number of spectroscopic members from N \sim 8 to \sim 45 members. From Ruel et al. (2014), a sample of 48 SPT GCs (hereafter R14 sample) with redshifts between 0.3 < z < 1.3, and a number of members between 5 to \sim 45, are retrieved. From Sifón et al. (2013) a total of 13 GCs, from the Atacama Cosmology Telescope (ACT; hereafter S13 sample), spanning a redshift range of 0.3 < z < 1 and 20 < N < 90. These catalogs can be downloaded from VizieR (see app. A.1.1). These three samples gather a total of 4696 galaxy redshifts across 123 GCs.

In addition to spectroscopy and optical imaging, we obtain the BCG positions from Z20 for the 15 GCs. Also, we use the information in Z20 about the center of the SZ emission centroid, M_{200} , and R_{200} . Nevertheless, SPT-CLJ2100-5708 is not included within the 288 clusters studied in Z20 and thus, we only have these parameters for 14 GCs of our sample.

The BCGs coordinates are matched to the cluster galaxy catalogs within 1 arcseconds using the package SKYCOORD. For two clusters, SPT-CLJ2344-4224 and SPT-CLJ0600-4353, no match was found and we obtain these BCGs redshift using dedicated spectroscopy from SOAR/Goodman observations (see next section).

3.6 Goodman Data

For SPT-CLJ2344-4224 and SPT-CLJ0600-4353 we measure the BCG redshift using the Goodman red camera. We use a 1" slit oriented in an angle to cover the BCG and another bright galaxy, for SPT-CLJ2344-4224 a galaxy also identified by the Gemini GMOS spectroscopy. The data was reduced using the Goodman Spectroscopic Data Reduction Pipeline (*The Goodman Pipeline*) installed in a

machine in SOAR. To obtain redshifts we use fxcor interactively following the methods described in 3.4.2. Thereby, our final sample consist of 1084 galaxies distributed in the observed area of the 15 clusters with approximately 70 galaxy redshifts each one.

Chapter 4

Analysis

4.1 Cluster redshift, membership selection, and dynamical mass

4.1.1 Cluster redshift and velocity dispersion

Galaxy clusters can sustain heavy interior subclustering throughout its merging history (Mostoghiu et al., 2019). However, a central redshift can still represent a good estimation of the position of the whole group. We are interested on measuring the average cluster redshifts, which reflects the Hubble flow motion of the cluster, and the velocity dispersion of clusters which is a proxy for the cluster's mass.

To find these parameters we use a 3σ -clipping on the peculiar velocities of the galaxies (Yahil and Vidal, 1977; Mamon et al., 2010; Saro et al., 2013; Ruel et al., 2014; Bayliss et al., 2016) which we apply iteratively using the biweight location estimator as the center of the distribution. Goodall (1983) performed simulations which showed that even for samples with at least 5 data points the biweight location estimator retains high efficiency. Then, to calculate the velocity dispersion of the distribution we follow Beers et al. (1990), using either the biweight scale σ_{bi} or the Gapper scale estimator σ_g depending on the number of members N (σ_g is preferred when N < 15; Beers et al., 1990). Note that in each iteration, peculiar velocities of galaxies v_i are obtained from their redshifts z_i as $v_i = c(z_i - z)/(1+z)$ (Danese et al., 1980) where z is the iteration's central heliocentric velocity found by the biweight location divided by the speed of light ($z = v_{\text{HEL,bi-loc}}/c$). Initial estimations are taken from a first iteration with a peculiar velocity cut of $\pm 5,000$

km s⁻¹ relative to the (visually identified) starting guess of the cluster redshift. Although, this is somewhat arbitrary, a generous 5,000 km s⁻¹ cut ensures that all cluster members are included. In one case the number of cluster galaxies was so low that contamination dominated the velocity distribution, making it artificially flat. To avoid this effect on low-member clusters we take an initial cut of $\pm 2,500$ km s⁻¹ if the number of galaxies inside the first cut is less than 15 galaxies. Cluster redshifts z and velocity dispersion σ are taken from the last iteration when the clipping process converge and no galaxies are rejected.

Uncertainties of the velocity dispersion $\sigma_{\rm BI}$ are described by $0.92\sigma_{\rm BI}/\sqrt{N-1}$ (0.91 $\sigma_g/\sqrt{N-1}$ for σ_g), which includes statistical uncertainties, systematic errors from the estimators (e.g. caused by non-Gaussianity), and effects of selection (e.g. rejection of true members and/or inclusion of non-members) (Ruel et al., 2014). Cluster redshift uncertainties are estimated as the standard error $\Delta z = \sigma(1+z)/c\sqrt{N}$ (Ruel et al., 2014), where N is the number of galaxies inside $\pm 3\sigma$. The individual galaxy redshift errors have a negligible contribution to the final estimate of the cluster redshift. To test this we compute median cluster redshifts that incorporate the individual galaxy redshift efforts by bootstrapping 1,000 samples and then computing the scatter of the median cluster redshift recovered. We found that the bootstrapped uncertainty in the median cluster redshift due to the individual galaxy redshifts is always lesser than 0.00025. Since these errors are added in quadrature its contribution to uncertainty is even smaller and is therefore disregarded.

4.1.2 Membership selection

While justifying a redshift cut for cluster membership is a straightforward process for relaxed clusters, it is less so for merging systems. Since there is no expectation for the distribution to be Gaussian, a 3σ -clipping (as in the cluster redshift determination) is less well motivated. Following Hernández-Lang et al. (2021) which studied an appropriate velocity cut in the LoS using the Illustris TNG300 simulations, we classify galaxies with peculiar velocities within $\pm 3,000$ km s⁻¹ from the cluster's redshift as member galaxies. Furthermore, motivated by different cuts made in the literature (e.g. Bayliss et al., 2016; Wen and Han, 2013) we report the dynamical state results for other velocity cut levels; a $\pm 3\sigma$ cut, and a $\pm 2,500$ km s⁻¹ cut. For the purpose of the dynamical state analysis, the center

of the distribution is always taken as the cluster redshift z and the center of the SZ centroid.

4.1.3 Dynamical mass

To estimate the cluster's dynamical masses we use Munari et al. (2013) $\sigma_v - M_{200}$ scaling relation. This scaling relation was obtained from a radiative simulation which included star formation, supernova triggered feedback, and AGN feedback. Munari et al. (2013) scaling relation is:

$$\frac{\sigma_{\rm 1D}}{\rm km s^{-1}} = A_{\rm 1D} \left[\frac{h(z) M_{\rm 200, dyn}}{10^{15} M_{\odot}} \right]^{\alpha}$$
 (4.1)

where $A_{1D} = 1177 \pm 4.2$ and $\alpha = 0.364 \pm 0.0021$. Mass errors are estimated by propagating the velocity dispersion errors through eq. 4.1. Details on the code line for this entire section can be found in app. A.5.

4.2 Dynamical state indicators

The dynamical state of a cluster can be identified by looking at the distribution of its members where it is assumed that relaxed clusters should have an underlying Gaussian distribution (Menci and Fusco-Femiano, 1996; Ribeiro et al., 2013; Hernández-Lang et al., 2021). To parameterize this departure from relaxation in the clusters we run multiple tests to classify their distributions as Gaussian (G) or non-Gaussian (NG).

For LoS analysis we use the Anderson-Darling (AD) test that is one of the most reliable 1D test to distinguish departure from relaxation (Hou et al., 2009). Other 1D test and a well known statistic used vastly in this topic is the Kolmogorov-Smirnov test (KS; Kolmogorov, 1933). Despite its low power for normality tests (Stephens, 1974; D'Agostino and Stephens, 1986; Hou et al., 2009), we include the KS test in the analysis to examine its performance. As these tests are based on the shape of the velocity distribution, the strength of the signal is higher for mergers along the LoS.

To complement the 1D LoS analysis, we include the Multidimensional Gaussian Mixture Modelling (Muratov and Gnedin, 2010) from the sklearn.mixture Python package test (Gaussian Mixture; Pedregosa et al., 2011), and use it to find

the most probable number of projected space components using spatial information from the spectroscopically confirmed cluster members.

Finally, we included the Dressler-Schectman (DS) test (Dressler and Shectman, 1988), which uses both spatial and velocity information, thus making a 3D analysis of the distribution.

In the following, we briefly explain the statistical tests used in this thesis and the steps followed to calculate each statistic. Details on the python code used can be found on app. A.6.

4.2.1 Anderson-Darling test

The AD test is a reliable tool to measure departure from relaxation. Hou et al. (2009) showed that its application is not restricted only to Gaussian distributions, moreover, it can be used with many continuous or discrete distributions. It is based on the analysis of the empirical distribution function (EDF) returning the statistical parameters A^2 and A^{2*} estimated from the ordered data $\{x_i\}$

$$A^{2} = -n - \frac{1}{n} \sum_{i=1}^{n} (2i - 1)(\ln \Phi(x_{i}) + \ln (1 - \Phi(x_{n+1-i})))$$

$$A^{2*} = A^{2} \left(1 + \frac{0.75}{n} + \frac{2.25}{n^{2}}\right). \tag{4.2}$$

with $x_i \leq x_{i+1}$ and $\Phi(x_i)$ is the cumulative distribution function (CDF) of the hypothetical underlying distribution. A^{2*} is a correction of the statistic for cases where the distribution parameters of the merging clusters are not known a priori (D'Agostino and Stephens, 1986; Hou et al., 2009). The significance level, α , which gives the probability that the data comes from a Gaussian distribution is then calculated as

$$\alpha = a \exp\left(-A^{2*}/b\right) \tag{4.3}$$

where the introduced coefficients a = 3.6789468 and b = 0.1749916 are factors determined via Monte Carlo simulations (Lloyd, 1998).

To interpret the results of AD tests we follow the criteria used by Hou et al. (2009) where $\alpha < 0.05$ indicates a NG distribution. Note that the probability α is not normalized to unity allowing probabilities greater than 1 when A^{2*} reach low

values. The only statistical importance of the AD test is to identify cases where the distribution is inconsistent with a Gaussian function at high significance for the purpose of identifying NG distributions. Thereby, to avoid nonsensical results we replaced all of these high α values to reach a maximum at $\alpha = 1$.

4.2.2 Kolmogorov-Smirnov test

The one-sample KS test quantifies the distance between the empirical distribution function (EDF) of the sample and the cumulative distribution function (CDF) of the reference distribution. The null distribution of this statistic is calculated under the null hypothesis that the sample is drawn from the reference distribution (i.e. a G distribution in this case). The main characteristic of KS tests is that it is sensitive to differences in both the location and the shape of the cumulative distribution function. The statistic computed for the KS test is the D value, which is the vertical difference between the EDF of the ordered data, x_i , of size n and the CDF. This value is derived from the positive deviation, D^+ , and negative deviation, D^- , from the CDF.

$$D^{+} = supremum \left| \frac{i}{n} - EDF \right| \tag{4.4}$$

$$D^{-} = supremum \left| EDF - \frac{(i-1)}{n} \right| \tag{4.5}$$

$$D = \max(D^+, D^-) \tag{4.6}$$

Originally, this statistic provides means of testing whether a set of observations are from some completely specified continuous distribution by comparing D to a specific critical value depending on the sample size (Smirnov, 1948). This method often probe to have some advantages over the chi-square test (David and Johnson, 1948; Massey Jr., 1951). It was the work of Lilliefors (1967) which found a way to test the hypothesis that a set of data arises from a normal distribution with unknown mean and variance. It modifies the standard KS test and present a table with a new set of critical values for different sample sizes. Here we use Lilliefors modification employing Stephens (1974) correction,

$$D^* = D\left(\sqrt{n} - 0.01 + \frac{0.85}{\sqrt{n}}\right). \tag{4.7}$$

This last correction (equation 4.7) allow us to compare D with one critical value table, rather than computing critical values for specific sample sizes and significance levels. Thereby, we use a critical value of $D^* > 0.895$ to identify NG from G clusters at a 95% confidence interval (Stephens, 1974).

4.2.3 Gaussian Mixture Modelling

A Gaussian mixture model (GMM) attempts to find a mixture of multidimensional Gaussian probability distributions that best model any input data set. GMM methods maximize the likelihood of the data set given all the fitted parameters, using the expectation-maximization (EM) algorithm (e.g., Press et al., 2007). To derive explicit equations one can assume that each mode is described by a Gaussian distribution as a simplification. The algorithm is fully scalable to multivariate distributions and for this study we employ a bi-dimensional GMM using sky projected coordinates of member galaxies.

Thereby, for a sample x_N^n of size N $(x_1, x_2, ..., x_i, ..., x_N)$ with n parameters $(x^1, x^2, ..., x^j, ..., x^n)$ the probability distribution of a single data point $P(x_i^j)$ is

$$P(x_i^j) = \sum_{k=1}^{K} p_k N(x_i^j | \mu_k^j, \sigma_k^j),$$

where

$$N(x_i^j | \mu_k^j, \sigma_k^j) = \frac{1}{(2\pi\sigma^2)^{1/2}} e^{\left[-\frac{(x-\mu)^2}{2\sigma^2}\right]}$$

is the Gaussian density of the kth component for the distribution of the jth parameter with his respective mean μ_k^j and standard deviation σ_k^j . The weight parameter p_k is normalized as $\sum_k p_k = 1$.

GMM methods stands out for its ability to determine the maximization likelihood values of the parameters (p_k, μ_k, σ_k) but with the disadvantage that the method will always split the data set into the specified number of modes, K (Muratov and Gnedin, 2010). When fitting models, it is possible to increase the likelihood by adding parameters, but doing so may result in overfitting. GMM addresses this problem by introducing a penalty term for the number of parameters in the model called Bayesian Information Criterion (BIC). The BIC penalty term approximate the posterior probability of a model with a uniform prior that scales with $\ln(N)$. Although there exist other kind of metrics and methods, in this thesis

we follow the work of Athey et al. (2019) that used the BIC to select the best GMM model fitted to the data. For specific definitions and further information we refer to the work of Athey et al. (2019).

To perform this routine first we use the cluster redshift, Right Ascension, and Declination coordinates to obtain separations (X,Y) in Mpc to the center of the distribution of each member galaxy. We use the multidimensional Gaussian Mixture model from the sklearn.mixture Python package (GaussianMixture, Pedregosa et al., 2011) that draws confidence ellipsoids for multivariate models and then compute the BIC statistics. The outcome of this module provides the number of subcomponents and the mean value of the location for each subcomponent, predicts the labels for the data sample and provides the BIC criteria for the number of subcomponents found. When searching for the right number of subclusters the sample size of subclusters would fall significantly if the number of modes is too high and it could lead to a wrong grouping of uncorrelated galaxies (or the unnecessary dissection of a subgroup) if the number of member galaxies is too low. Also, since we are looking to find if the cluster can or can not be separated into more than one unique group, these statements motivate us to run only two type of models, a unimodal distribution set with a number of modes of K=1 and a bimodal distribution with a number of modes of K=2. We report the number of subclusters indicated by the best model selected from the lowest BIC. Finally, as GMM locate subcomponents in the distribution we speak of presence of subclustering when identifying more than one component. We do not expect that GMM capabilities identify perturbations of a dynamically unevolved cluster, which not necessarily involves the merger of two separate components but instead the virialization of already accreted systems (Mostoghiu et al., 2019).

4.2.4 Dressler-Shectman test

The DS test uses spatial information as well as redshift information. It evaluates the local mean velocity kinematics of galaxy neighbors, identified in sky projected clusters, and searches for deviations from the cluster mean values (Pinkney et al., 1996). For each galaxy the test takes n neighbours and determines the mean local velocity v_{local} and local velocity dispersion σ_{local} for each subsample. Finally, compares the local values to the mean global velocity v_c and velocity dispersion

 σ_c of the whole cluster of $N_{\rm gal}$ galaxies. These deviations are quantified by

$$\delta_{\text{local}}^2 = \frac{(n+1)}{\sigma_c^2} \left[(\upsilon_{\text{local}} - \upsilon_c)^2 + (\sigma_{\text{local}} - \sigma_c)^2 \right]. \tag{4.8}$$

We adopt $n=N_{\rm gal}^{1/2}$, as suggested by Pinkney et al. (1996). The significance of substructure is quantified as the cumulative deviation Δ , which is the sum of $\delta_{\rm local}$ over all cluster galaxies $N_{\rm gal}$,

$$\Delta = \sum_{\text{local}=1}^{N_{gal}} \delta_{\text{local}} \tag{4.9}$$

 Δ is large for groups with kinematically distinct subgroups; for random distribution of velocities, Δ values should be of the order of $N_{\rm gal}$, but for the case of NG distributions, Δ can be significantly larger than $N_{\rm gal}$, even if there is no subclustering (Dressler and Shectman, 1988). For this reason, we calibrated the Δ statistic by Monte Carlo simulations. The Monte Carlo simulation breaks any true correlation between velocities and positions since it randomly shuffle these values before quantifying any statistical parameter. So we ran 5,000 models for each cluster and calculated $\Delta_{\rm sim}$ each time. The significance of having substructure or the *p-value* is then calculated as the ratio of the number of $\Delta_{\rm sim}$ that is larger than the estimated Δ over the total number of simulations $(N_{\Delta_{\rm sim}})$. The smaller the *p-value*, the larger is the probability of substructure.

For clusters with a number of spectroscopic members greater than 20, the DS test provides a robust identification of substructures when the p-value limit is set to be under 0.05. For clusters with less than 20 spectroscopically confirmed members this indicator becomes unreliable (Hou et al., 2012).

Chapter 5

Results

5.1 Cluster properties and BCG membership

In Table 5.1 cluster redshift values, velocity dispersions, and dynamical masses, along with the number of member galaxies within $\pm 3,000 \,\mathrm{km}\,\mathrm{s}^{-1}$, are listed. The average of member galaxies per cluster is ~ 35 . Note that SPT-CLJ2100-5708 is the only cluster with less than 15 members, thus we report σ_g (see § 4.1). In Fig. 5.1 we show redshift histograms of all galaxies for each cluster, including background and foreground galaxies. The red bars and insets show the velocity distribution for galaxies within $\pm 5,000 \,\mathrm{km}\,\mathrm{s}^{-1}$. In several cases a bi-modal distribution seems visually striking, such as for SPT-CLJ2344-4224, SPT-CLJ0144-4807, SPT-CLJ0451-4952, SPT-CLJ0354-5904, SPT-CLJ01111-5518, and SPT-CLJ0522-5026.

One of the goals of this thesis is to confirm the membership of the candidate BCG selected by Z20. We matched the BCG positions to our cluster catalogs using a radius of 1 arcsecond, finding 2 of them to be clearly foreground galaxies with velocities with respect to the cluster below $-19,000~{\rm km\,s^{-1}}$ (SPT-CLJ0151-5654 and SPT-CLJ0439-5330), and two galaxies with velocities at -4,286 and $6,110~{\rm km\,s^{-1}}$ (SPT-CLJ2344-4224 and SPT-CLJ2358-6129, respectively; see Table 5.1 and dashed lines in Fig. 5.1). If we use a $\pm 3,000~{\rm km\,s^{-1}}$ limit for cluster membership (Hernández-Lang et al., 2021), then 11 BCGs belong to their respective clusters, all of them within $\pm 1,700~{\rm km\,s^{-1}}$. The BCG contamination rate is then of $27\%~\pm~13\%$ for the whole sample. If we exclude SPT-CLJ2100-5708 then the BCG contamination is $29\%~\pm~14\%$. All the miss-identifications are at z < 0.43. Fig. 5.2 shows the position of the BCGs in the velocity distribution of the GCs within $\pm 5,000~{\rm km\,s^{-1}}$. We confirm the BCG membership status when

Table 5.1: Spectroscopy results of 15 SPT Clusters.

SPT-CL N_{mem}	N_{mem}	23	σ	$M_{200,\mathrm{dvn}}^a$	M_{200}^b	R_{200}^b	BCG^c	$BCG \text{ vel}^c$
			${ m kms^{-1}}$	$10^{14} \dot{M_{\odot}}$	$10^{14} M_{\odot}$	\Box	mem.	${ m kms^{-1}}$
J2344-4224	40	0.282384 ± 0.000675	906 ± 133	6.19 ± 2.51	4.602 ± 1.32	5.44	٠.	-4286
J0151-5654	23	0.294158 ± 0.00089	972 ± 200	7.47 ± 4.22	4.868 ± 1.35	5.54	×	-23577
J0144-4807	43	0.317957 ± 0.0005	766 ± 110	3.82 ± 1.51	4.919 ± 1.34	5.27	>	-1205
J0600-4353	54	0.322976 ± 0.000755	1290 ± 160	15.98 ± 5.45	7.533 ± 1.48	5.4	>	-1674
J2358-6129	19	0.374287 ± 0.000789	744 ± 161	3.42 ± 2.04	6.067 ± 1.3	4.92	×	6110
J0451-4952	34	0.3976 ± 0.000857	1004 ± 160	7.69 ± 3.38	4.714 ± 1.25	4.34	>	271
J0354-5904	45	0.398998 ± 0.001002	1394 ± 183	18.91 ± 6.83	6.344 ± 1.29	4.61	>	09
J0439-5330	37	0.420179 ± 0.000904	1096 ± 163	9.65 ± 3.96	5.452 ± 1.21	4.23	×	-19567
J0337-4928	36	0.502187 ± 0.000402	460 ± 77	0.85 ± 0.39	5.268 ± 1.19	3.59	>	896
J0111-5518	37	0.503513 ± 0.00089	1068 ± 171	8.57 ± 3.77	4.335 ± 1.24	3.23	>	34
J0135-5904	42	0.509212 ± 0.000937	1239 ± 178	12.84 ± 5.07	4.387 ± 1.26	3.57	>	-448
J0522-5026	42	0.550769 ± 0.000905	1069 ± 151	8.35 ± 3.26	4.735 ± 1.16	3.51	>	870
J2100-5708	∞	0.551477 ± 0.001475	794 ± 295	3.69 ± 3.77			>	-86
J0612-4317	30	0.615316 ± 0.001084	956 ± 163	5.91 ± 2.78	6.17 ± 1.29	3.73	>	40
J0550-5019	21	0.665938 ± 0.000702	540 ± 117	1.19 ± 0.71	4.274 ± 1.13	2.9	>	237

Notes. ^aDynamical mass $M_{200,dyn}$ calculated with Munari et al. (2013) formula (eq. 4.1). ^bMass M_{200} and radius R_{200} candidate, and?? for unknown BCG status. The last column show the BCG velocity with respect to the center of the extracted from Z20. c BCG membership status denoted with a \checkmark for confirmed membership, a \varkappa for discarded BCG velocity dispersion.

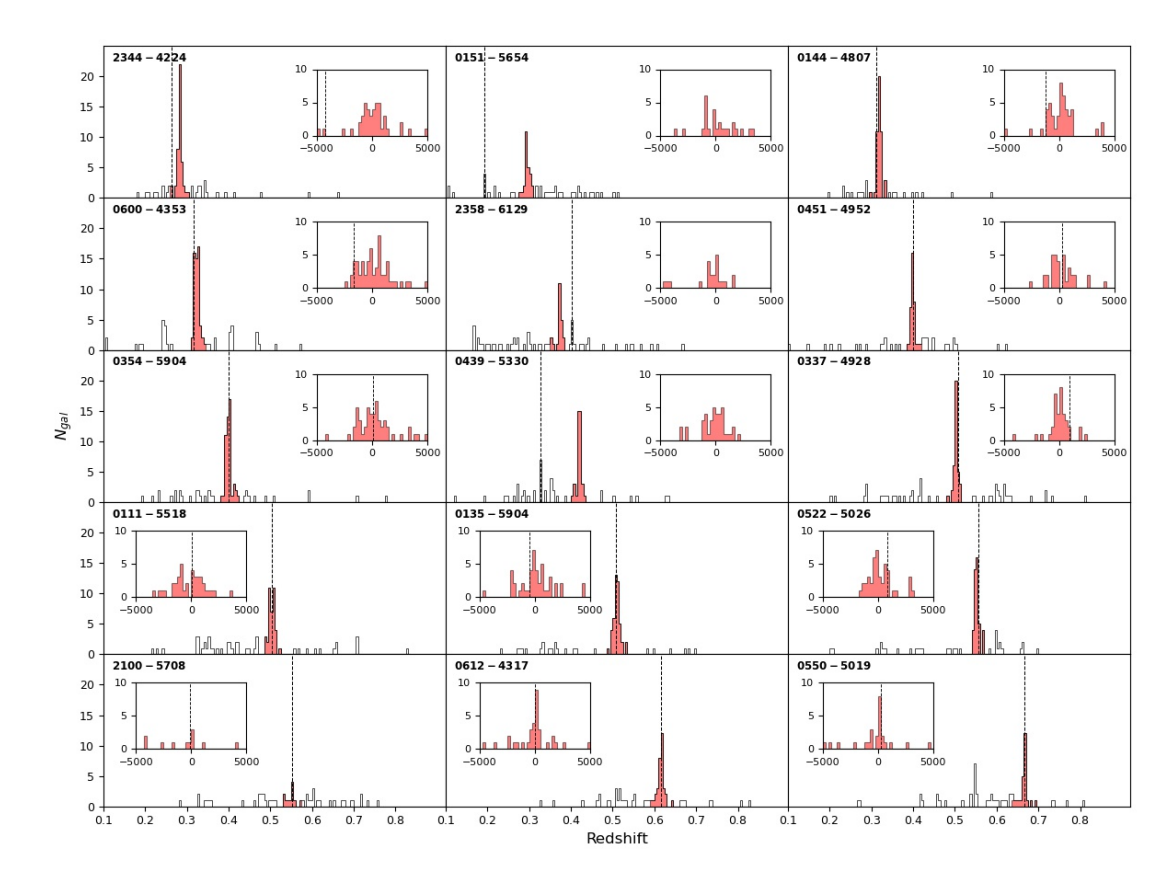


Figure 5.1: Redshift histograms for the 15 clusters (bin size 0.005). Red bars and inner panels (bin size 250 km s⁻¹) indicate galaxies within $\pm 5{,}000$ km s⁻¹. Black dashed lines indicate the position of the BCG.

the velocity of the BCG candidate is within $\pm 3,000~\rm km\,s^{-1}$ and discard the BCG candidates of three clusters (SPT-CLJ0151-5654, SPT-CLJ2358-6129, and SPT-CLJ0439-5330) as they lie beyond $\pm 5,000~\rm km\,s^{-1}$. But for SPT-CLJ2344-4224 the BCG candidate lies within the latter velocity cut and it is just $\sim 1,000~\rm km\,s^{-1}$ closer than our membership velocity cut selection. Thereby, we do not confirm its membership to the cluster, but we do not discard its potential as a candidate.

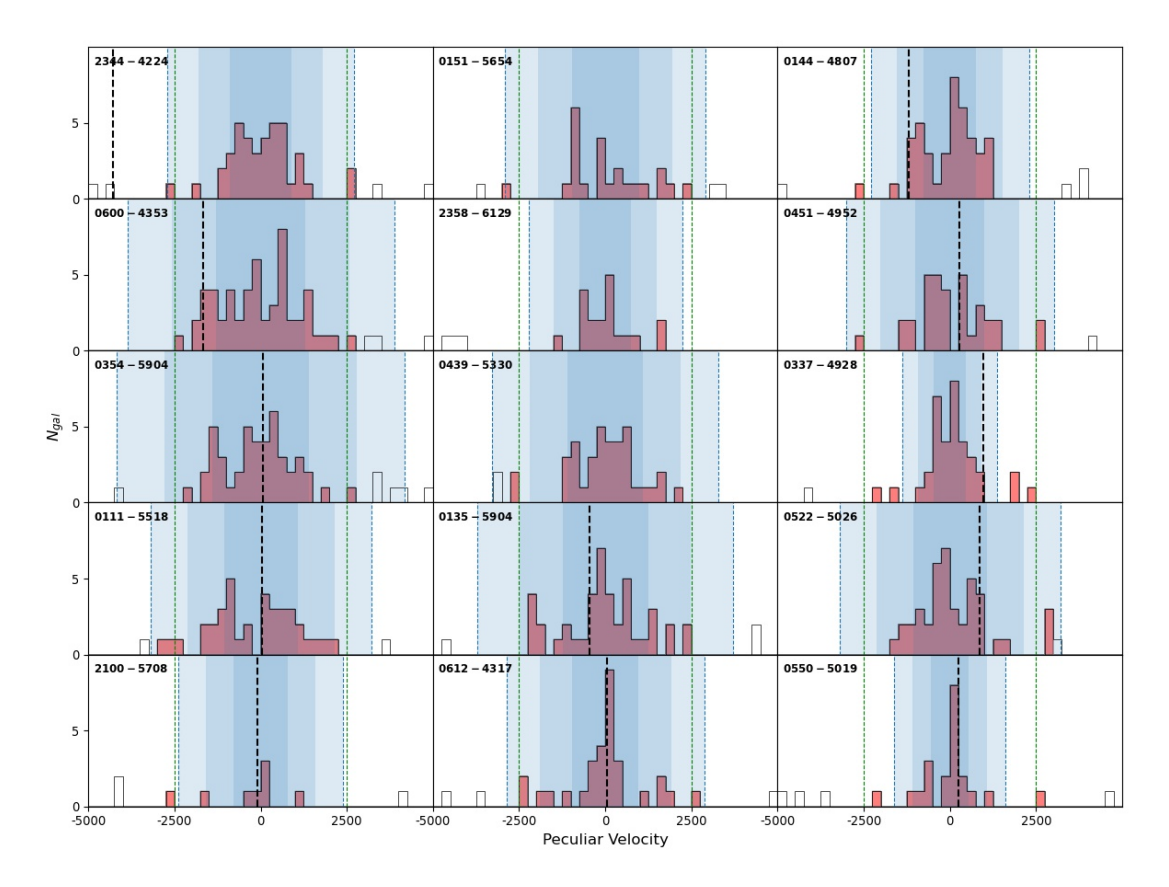


Figure 5.2: Peculiar velocity of galaxies inside $\pm 5{,}000~\rm km\,s^{-1}$ with member galaxies as red bars (bin size 250 km s⁻¹). The Black dashed line indicate the position of the BCG. Green dashed line mark 2,500 km s⁻¹. The shaded regions represent 1, 2, and 3σ going from darker to lighter blue regions and dashed line.

5.2 Dynamical state

Results from the dynamical state tests are shown in Tables 5.2, 5.3, and 5.4. The tables show values for three velocity cuts, indicating if the distribution is consistent with a Gaussian distribution (G) or if it is not (NG). They also show the GMM2D results indicating if 1 or 2 components (the only options) are preferred. For the $\pm 3,000~{\rm km\,s^{-1}}$ velocity cut level, 7 clusters are found for at least one test as disturbed. 4 of the clusters (SPT-CLJ0151-5654, SPT-CLJ0451-4952, SPT-CLJ0111-5518, and SPT-CLJ0135-5904) show no deviations from relaxation through all tables 5.2 to 5.4.

We remark that the methods used in this study yield coherent results with the ones of B16 which also used the AD test to find 9 clusters with $\alpha < 0.05$. If we obtain the cluster redshifts and velocity dispersions for the B16 sample using

the methods in § 4.1, and then run the AD test; there are 10 clusters which present α values lower than 0.05. From these 10 clusters, 8 are the same with NG distributions in the B16 results. The small discrepancy is due to the cluster redshift and velocity dispersion estimation which differs only in the added ± 2500 initial velocity cut for low-member clusters. In addition, if we compare these estimations with the ones of B16 we find good coincidence with differences less than $\sim 10\%$, even in the number of cluster members.

		AD	KS	DS	GMM2D	AD	KS	DS
SPT-CL	N	α	D^*	p-val.		$\alpha < 0.05$	$D^* \ge 0.895$	p-val. $<$ 0.05
J2344-4224	40	0.182516	0.694299	0.5062	2	G	G	G
J0151-5654	23	0.251492	0.615952	0.8584	1	G	G	G
J0144-4807	43	0.088039	0.837021	0.5512	1	G	G	G
J0600-4353	54	0.745519	0.569097	0.0346	1	G	G	\overline{NG}
J2358-6129	19	0.325113	0.713851	0.3478	1	G	G	G
J0451-4952	34	0.311488	0.601306	0.386	1	G	G	G
J0354-5904	45	0.695421	0.511864	0.487	1	G	G	G
J0439-5330	37	0.481172	0.450373	0.1312	2	G	G	G
J0337-4928	36	0.005674	0.958729	0.6378	1	NG	NG	G
J0111-5518	37	0.584639	0.585253	0.9	1	G	G	G
J0135-5904	42	0.504057	0.616973	0.3226	1	G	G	G
J0522-5026	42	0.024253	0.854101	0.088	2	NG	G	G
J2100-5708	8	0.103107	0.837362	0.766	1	G	G	G
J0612-4317	30	0.013935	0.884303	0.5366	1	NG	G	G
J0550-5019	21	0.02625	0.828025	0.893	2	NG	G	G

Table 5.2: $\pm 3,000 \text{ km s}^{-1}$ sample dynamical tests results.

Notes. G indicates coincidence with a Gaussian distribution while NG indicates a

non-Gaussian distribution. Strictly speaking, in the case of the DS test, NG indicates presence of substructure and G for absence of it.

As we discuss in the next chapter, for clusters with perturbations in the LoS direction the AD test should assess the dynamical state with a high efficiency, and better than that of KS test, while in the case of mergers in the plane of the sky GMM2D shall detect the major components. It must be noted that DS test does not account for deviations from Gaussianity but instead accounts for presence of substructure. Substructure is an indicative of recent accretion of galaxies or smaller groups of galaxies (Lacey and Cole, 1993), while on the other hand, non-Gaussianity would indicate a dynamically complex or unevolved system (Hou et al., 2013). Thereby, our set of dynamical state tests search for different types of evidence of disturbance (and its direction) and thus we confirm

		AD	KS	DS	GMM2D	AD	KS	DS
SPT-CL	N	α	D^*	p-val.		$\alpha < 0.05$	$D^* \ge 0.895$	p-val. $<$ 0.05
J2344-4224	37	1.0	0.514892	0.392	1	G	G	G
J0151-5654	22	0.066595	0.792054	0.9082	1	G	G	\mathbf{G}
J0144-4807	42	0.080296	0.737004	0.3906	2	G	G	\mathbf{G}
J0600-4353	53	0.449195	0.66074	0.0896	1	G	G	G
J2358-6129	19	0.325113	0.713851	0.3306	2	G	G	${ m G}$
J0451-4952	31	0.662568	0.568768	0.1532	1	G	G	G
J0354-5904	44	0.389214	0.560436	0.2116	1	G	G	\mathbf{G}
J0439-5330	35	0.834644	0.424484	0.0686	2	G	G	\mathbf{G}
J0337-4928	36	0.005674	0.958729	0.65	1	NG	NG	\mathbf{G}
J0111-5518	35	0.431987	0.754289	0.9618	1	G	G	G
J0135-5904	42	0.504057	0.616973	0.3276	1	G	G	G
J0522-5026	39	0.96669	0.484477	0.0756	2	G	G	\mathbf{G}
J2100-5708	7	0.136293	0.700453	0.4516	1	\mathbf{G}	G	${ m G}$
J0612-4317	29	0.010833	0.924044	0.6544	1	NG	NG	${ m G}$

Table 5.3: $\pm 2,500 \, \text{km} \, \text{s}^{-1}$ sample dynamical tests results.

the disturbed dynamical state of a cluster when at least one of the tests find evidence of unrelaxation. Also, since Z20 selection is based on the BCG-gas offset, our sample is biased towards mergers in the plane of the sky.

2

NG

NG

G

0.722

J0550-5019

20

0.043252

0.999082

For the 7 disturbed clusters, we estimated density contour maps from the RCS galaxy distribution which are shown in Fig. 5.3 along with the AD, GMM2D, and DS output. We highlight SPT-CLJ0522-5026 as this cluster show clearly correlated substructure of its spatial and velocity distribution where a merger of similar scale is apparently happening.

Table 5.4: $\pm 3\sigma~{\rm km\,s^{-1}}$ sample dynamical tests results.

		AD	KS	DS	GMM2D	AD	KS	DS
SPT-CL	N	α	D^*	p-val.		$\alpha < 0.05$	$D^* \ge 0.895$	p-val. $<$ 0.05
J2344-4224	40	0.182516	0.694299	0.5078	2	G	G	G
J0151-5654	22	0.066595	0.792054	0.9054	1	G	G	G
J0144-4807	42	0.080296	0.737004	0.3994	2	G	G	G
J0600-4353	56	0.684491	0.446132	0.1742	1	G	G	G
J2358-6129	19	0.325113	0.713851	0.3298	1	G	G	G
J0451-4952	34	0.311488	0.601306	0.3874	1	G	G	G
J0354-5904	50	0.026859	0.788549	0.412	1	NG	G	G
J0439-5330	39	0.031602	0.689711	0.182	2	NG	G	G
J0337-4928	31	0.721301	0.507369	0.5536	1	G	G	G
J0111-5518	37	0.584639	0.585253	0.9006	1	G	G	G
J0135-5904	42	0.504057	0.616973	0.3422	1	G	G	G
J0522-5026	43	0.005491	0.951527	0.2538	2	NG	\overline{NG}	G
J2100-5708	7	0.136293	0.700453	0.4342	1	G	G	G
J0612-4317	30	0.013935	0.884303	0.5428	1	NG	G	G
J0550-5019	19	0.185549	0.935069	0.379	2	G	\overline{NG}	G

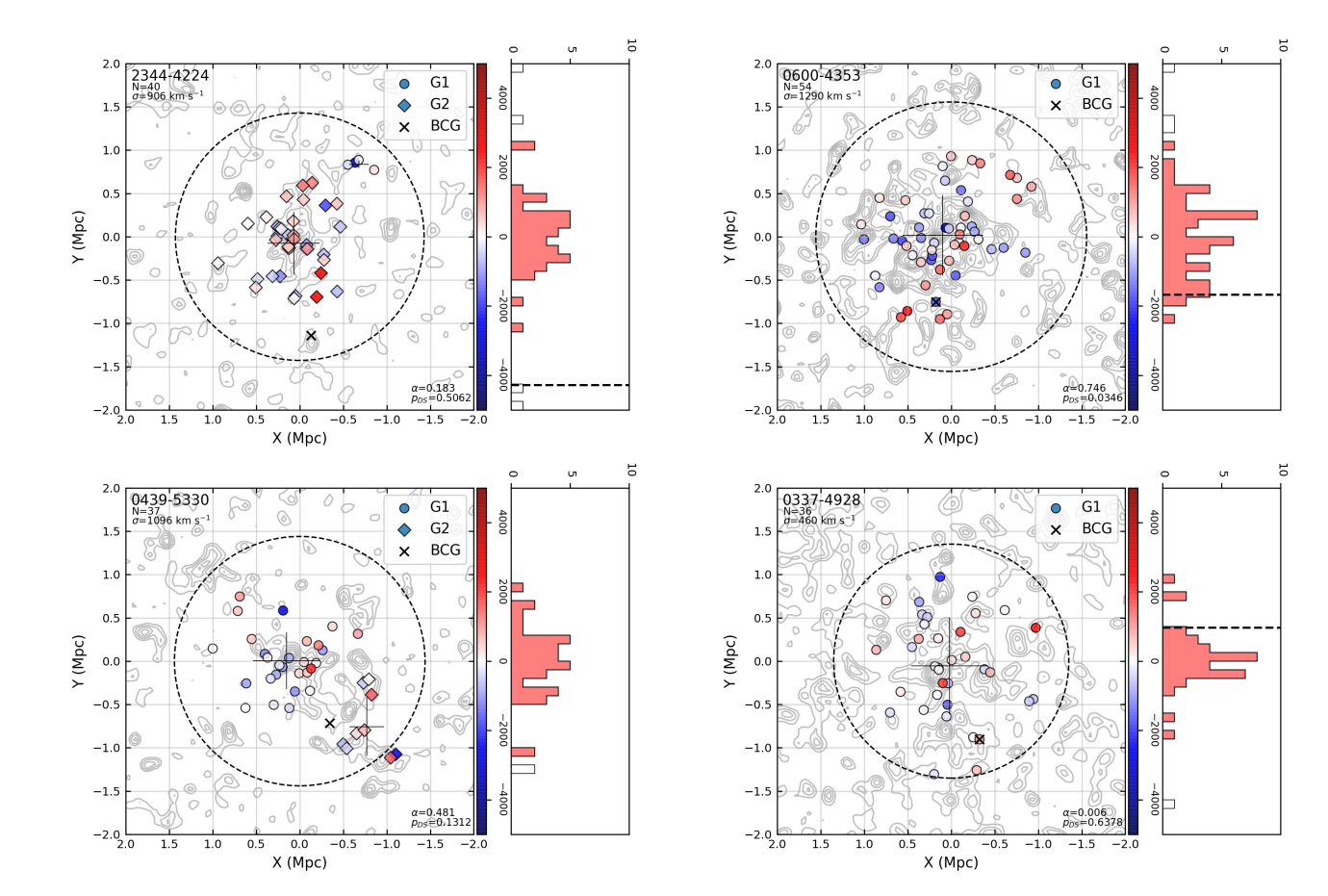


Figure 5.3: Distribution of galaxies in the projected plane for the 7 disturbed clusters together with contour levels for the numerical density map of RCS galaxies. Circles and diamonds show galaxies which belong to components found with GMM2D (only circles in the case of just one component). Centers and standard deviations of components found by GMM2D are noted with black solid perpendicular lines. The black cross indicate the position of the BCG and the dashed circle indicate R_{200} . Red and blue shades indicate the velocity of galaxies. The side panel on every plot shows the velocity distribution with the BCG pointed as a dashed black line and member galaxies as red filled bars.

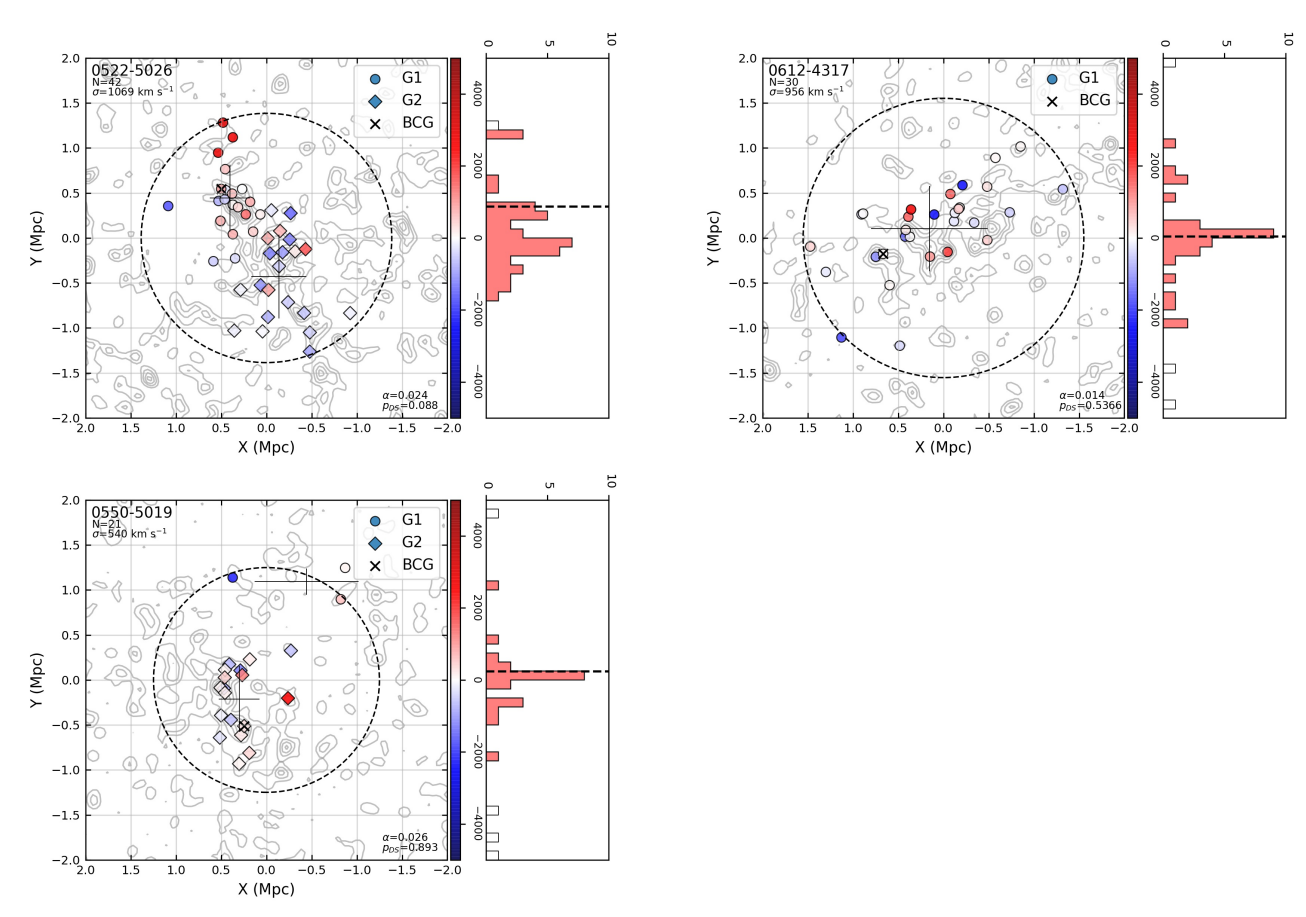


Figure 5.3: (Continued)

Chapter 6

Discussion and conclusions

Massive GC mergers allow us to study a range of phenomena, from particle physics (e.g., Harvey et al., 2015; Wittman et al., 2017; Fischer et al., 2021) to cosmology (e.g., Thompson et al., 2015; Bouillot et al., 2015). It is crucial, for the understanding of the impact of merging processes on the galaxy population, to assemble a sample that contains clusters in a range of merging states. To draw high significance results, over a large fraction of the Universe's life, a mass limited, nearly redshift independent, and statistically significant sample of disturbed clusters is ideal. Consequently, methods to accurately determine the dynamical state of GCs are an important ingredient. In this work we used spectroscopy for 15 GCs, with 14 of them selected by their large BCG to gas (X-ray peak/centroid or SZ centroid) offset. Our objective is to confirm the BCG candidate membership, to obtain dynamical masses, and use multiple statistical tests to probe the dynamical state of the clusters. The discussion of our statistical tests results are presented in the following order: first we discuss the outcome of the dynamical state tests, then we probe the tests' efficiency by making numerical simulations of 3D mergers, and finally we run the dynamical state tests over a large sample of GCs collected from literature.

6.1 Dynamical state in the LoS: AD and KS test

For the LoS analysis, the AD test finds between 3 and 4 clusters, depending on the velocity cut, as NG. On the other hand, KS test finds between 1 and 3 clusters. These low number of detections are not surprising since the sample is biased towards mergers in the plane of the sky. Thus, 9 clusters through all velocity cut levels show no evidence of perturbation in the LoS direction. However, it is worth noticing that clusters with visual signs of a bimodal velocity distribution (see Fig. 5.2), such as SPT-CLJ2344-4224, SPT-CLJ0144-4807, SPT-CLJ0451-4952, and SPT-CLJ0111-5518 are not classified as NG, while for SPT-CLJ0354-5904 only for the 3σ velocity cut case this cluster is classified as NG. This suggest that the AD and KS test are unable to reject the hypothesis of a G distribution with the current number of galaxies per cluster and the observed velocity separations in those clusters. If we fit two G distributions to the velocity profile of these clusters we find that we need at least 70(100) redshifts for the AD(KS) test to have enough statistical power to give a different classification in the best cases (i.e. minimum found for all fits; vel. separation of $\sim 1,300 \text{ km s}^{-1}$ and $\sigma_1/\sigma_2=2.39$; see app. A.7). Nevertheless, Hou et al. (2009) demonstrated using Monte Carlo simulations that the AD test is reliable even for small samples sizes of N<50. These simulations use 30,000 semi-analytical iterations to probe the skewness of Gaussian random distributions. Since our simulation intends to resemble a fusion of two different groups, this suggest that AD test may not discern merging substructure for the number of member galaxies and velocity separations in our data but it can reliably detect deviations from Gaussianity for this sample size regime. Thus, LoS perturbations in our sample, if any, should be detected by the AD test while mergers in the same orientation relies undetectable for our sample size regime (<60 member galaxies).

Thereby, for the $\pm 3,000~{\rm km\,s^{-1}}$ velocity cut level, 4 clusters present evidence of perturbation: SPT-CLJ0337-4928, SPT-CLJ0550-5019, SPT-CLJ0612-4327, and SPT-CLJ0522-5026.

6.2 Dynamical state in the spatial direction: GMM2D

The results from GMM2D, which use the galaxy spatial distribution, may correlate with the Z20 D_{BCG-SZ} offset results. At the $\pm 3,000~{\rm km\,s^{-1}}$ velocity cut level, GMM2D finds that 4 clusters SPT-CLJ0522-5026, SPT-CLJ0439-5330, SPT-CLJ2344-4224, and SPT-CLJ0550-5019 present more than one component in the sky plane. When looking at Fig. 5.3, these last two clusters (SPT-CLJ2344-4224 and SPT-CLJ0550-5019) show substructures with less than 5 members as

 $^{^{0}\}mathrm{Z}20$ uses all red sequence galaxies, while in this work we use only cluster galaxies spectroscopically confirmed

found by GMM2D. Specifically, the small substructure in SPT-CLJ0550-5019 seems highly uncorrelated in velocity and sky positions. Recommended minimum sample sizes for ML estimates were formulated by Psutka and Psutka (2019) which found at 90% confidence level a sample size $\hat{S}_{0.90} = 2.5d(d+4)$, where d is the number of dimensions. This set the limit to N > 30 galaxies needed to find confident results with GMM2D, which is not the case only for SPT-CLJ0550-5019 from the list of GMM2D disturbed clusters. This suggest that the result found by GMM2D for this cluster is not a confident result. In the case of SPT-CLJ2344-4224, there is a small system with 4 galaxies at a median velocity of -199 km s⁻¹ from the cluster center. The velocity dispersion is 1,151 km s⁻¹but if we remove the closest galaxy at -2.661 km s⁻¹the velocity dispersion is 233 km s⁻¹. Even if we recognize this small system as an infalling substructure, the question arises on how many galaxies must have a substructure to effectively disturb the dynamical state of a cluster with a certain number of members. As a reference, Hou et al. (2012) studied methods to classify the dynamical state of GCs by running simulations where a smaller substructure was accreted into the main cluster. The number of galaxies they used for this substructure was 10(4) when the main host had 50(10)members. Anyway, this question could not be answered here as we do not know how many other galaxies represent these spectroscopic members. Nevertheless, since the number of members for this cluster provide enough statistical power for GMM2D to assess the number of components at a 90% confidence level, we confirm the dynamical state of this cluster as disturbed.

In \S 4.2 we forced K to include up to two components. If we let K vary up to 8 components, we find that 4 of the clusters with at least 30 members have more than one component; 3 of them are the same clusters where GMM2D find exactly 2 components again; and for the forth cluster, SPT-CLJ0612-4317, GMM2D find 7 components. Thus indicating a heavy subclustering in the sky plane which GMM2D could not approximate to bimodality.

The clusters with unimodal distributions as found by GMM2D through all the velocity cuts are SPT-CLJ0600-4353, SPT-CLJ0451-4952, SPT-CLJ0354-5904, SPT-CLJ0337-4928, SPT-CLJ0111-5518, and SPT-CLJ0135-5904. Even when testing with 8 components, these cluster only show one component. All these clusters have more than 30 members, thus indicating that subclustering in the plane of the sky is discarded at a 90% confidence level. This does not discard the possibility of other forms of perturbations, such as deviations from Gaussianity,

as GMM2D does not account for deformations in the central distribution.

6.3 3D approach of the dynamical state: DS test

DS test does not find signals of perturbation in the 3D distribution in almost any cluster in the sample. The only coincidence with a NG distribution (strictly speaking, detection of substructure in this case) appear in table 5.2 for SPT-CLJ0600-4353. Hou et al. (2012) showed that DS test strongly depends on the sample size: It is mainly powerful to detect spatially separated components at any sample size but for 20<N<50, DS test can detect substructures only if the central locations are separated in LoS by 2σ ; for N>50 it can detect substructures even within 1σ of separation in LoS; and no matter the host sample size DS test can not detect substructures with less than 4 galaxies. Furthermore, DS test is designed to find substructure but not necessarily assess the dynamical state, thereby it is incomplete (Sifón et al., 2015). Also, there are known mergers where DS test could not find evidence of substructure (e.g., Menanteau et al., 2012; Barrena et al., 2013; Jee et al., 2014; Dawson et al., 2015), and most of these are mergers in the plane of the sky. Since our sample is biased towards mergers in the plane of the sky and the sample size regime is around 40 galaxy members, this suggest that DS test may be unsuitable for the velocity separations in our sample and substructure in the LoS direction remains undetectable for this test. Nevertheless, SPT-CLJ0600-4353, the only cluster with N>50, may be suffering mergers preferentially in the LoS while disturbance in the form of subclustering in the plane of the sky direction is unlikely (as found in \S 6.2).

6.4 Simulating 3D mergers

To test the performance of the statistics discussed above, we generated a random sample using numpy.random.multivariate_normal¹ and configure it to resemble a distribution of two Gaussian distributions separated by a predefined offset (see A.8 for details). To find appropriate cluster parameters representative of our cluster sample we first selected SPT-CLJ0522-5026 as it has multiple

 $^{^{1}} https://numpy.org/doc/stable/reference/random/generated/numpy.random.\\ multivariate_normal.html$

coincidences with NG distributions. But since our sample is at the brink of undersampling as discussed in previous sections, this yield unsatisfying results for the experiment. We want the simulation to be easily detected as perturbed by all the tests to explore their response to different merger dispositions. Thus, we increase the separations and scales of the configuration resembling an even massive SPT-CLJ0522-5026-like merger. We use velocity and spatial dispersions of $\sigma_v = 400 \,\mathrm{km}\,\mathrm{s}^{-1}$ and $\sigma_s = 0.375 \,\mathrm{Mpc}$, take separations of $d_v = 1,200 \,\mathrm{km}\,\mathrm{s}^{-1}$ and $d_s = 1.2 \,\mathrm{Mpc}$, and generate the distribution with N=50 data points. These characteristics are extended into three sets adopting different merger ratios. Table 6.1 shows the configuration sets indicating the number of data points, velocity dispersion, and spatial dispersion assigned to each Gaussian component to generate the distributions as in the example shown in Fig. 6.1.

 $\sigma_v \; (\,\mathrm{km}\,\overline{\mathrm{s}^{-1}})$ n $\sigma_s \text{ (Mpc)}$ 25 400 0.375D1Set 1: D225 400 0.375D130 475 0.4375Set 2: D220 325 0.3125D135 5500.5 Set 3: D215 250 0.25

Table 6.1: Parameter sets for 3D merger simulation.

Notes. Configurations sets for each case: Data points n, velocity dispersion σ_v , and spatial dispersion σ_s assigned to each distribution D1 and D2.

We iterate 100 times for each set, generating the double Gaussian distribution and estimating the dynamical state statistics each time². This process is performed for three different collision angles; we define a collision angle θ_c in a manner such that for $\theta_c = 0^{\circ}$ the merger is in the LoS direction (i.e. $d_v = 1,200 \,\mathrm{km\,s^{-1}}$ and $d_s = 0 \,\mathrm{Mpc}$), for $\theta_c = 90^{\circ}$ the merger is in the projected space direction (i.e. $d_v = 0 \,\mathrm{km\,s^{-1}}$ and $d_s = 1.2 \,\mathrm{Mpc}$), and for $\theta_c = 45^{\circ}$ the velocity and spatial offsets are $d_v = 1,200/\sqrt{2} \,\mathrm{km\,s^{-1}}$ and $d_s = 1.2/\sqrt{2} \,\mathrm{Mpc}$ (thus following a respective cosine and sine law at 45°).

The results presented in table 6.2, 6.3, 6.4 consists in the percentage of cases

 $^{^2}$ For reasons of computing resources the Monte Carlo simulations to estimate the DS p-value are reduced to 1,000 iterations.

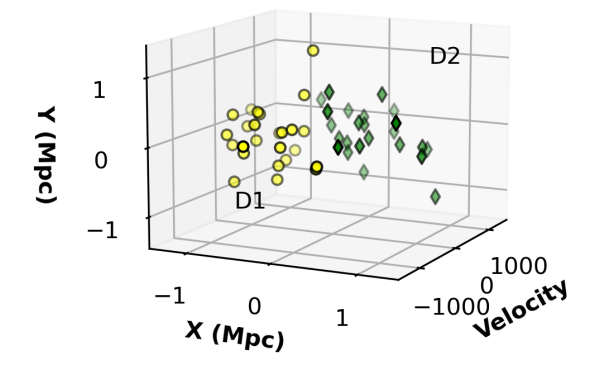


Figure 6.1: An example of the double Gaussian distribution with config. set 1 and an angle of 45° .

that a NG distribution is found by each statistic. The results show coherent behaviors for the LoS and sky plane direction tests as AD and KS show high efficiency when the merger is in the radial direction while GMM2D assess the correct number of components when they are in tangential disposition. When comparing the LoS tests at 0° and 45°, the fraction of NG classifications for AD test is always higher than the fraction found by KS test. This indicate that KS test is less efficient at detecting interacting systems than the AD test, which is in agreement with the findings in literature (Stephens, 1974; D'Agostino and Stephens, 1986; Hou et al., 2009). Note that the detections of disturbance of KS test in this study are always accompanied by another test's detection. This means that until now the results on perturbed and relaxed clusters in our sample does not change when ignoring KS test outcome.

In the case of 3D analysis, the DS test show an outstanding rate of detection when the merger has separations in both directions. Particularly, DS test fails to correctly classify the dynamical state of the merger when it is oriented specifically in the LoS or the sky plane direction, and much more so when the merger ratio is near to a 1:1 merger. When comparing the highest percentages at 90° with that at 0°, DS test show almost half the percentage of NG classifications with a 27%. This suggest that DS test has a low efficiency to detect substructure on mergers oriented in the sky plane direction. This reinforce the discussion hold in § 6.3 that DS test is unsuitable for our sample as it is selected with proxies that denote spatial disturbance and thus, it is biased towards mergers (or Virial equilibrium perturbations) in that direction.

These results are in agreement with the results of Hou et al. (2012) which

Table 6.2: Results of 3D merger simulation. $\theta_c=0^{\circ}$.

$\theta_c = 0^{\circ}$	Set 1: 25-25	Set 2: 30-20	Set 3: 35-15
$\alpha < 0.05$	98%	99%	95%
$D^* \ge 0.895$	90%	89%	77%
DS p -value<0.05	10%	18%	68%
GMM2D N-comp>1	0%	1%	3%

Notes. Dynamical statistics tested with a double Gaussian distribution with collision angle θ_c =0° (merger in the line of sight). The values indicate the percentage of NG classifications.

Table 6.3: Results of 3D merger simulation. $\theta_c=45^{\circ}$.

$\theta_c = 45^{\circ}$	Set 1: 25-25	Set 2: 30-20	Set 3: 35-15
$\alpha < 0.05$	33%	43%	32%
$D^* \ge 0.895$	29%	20%	21%
DS p -value<0.05	100%	100%	100%
GMM2D N-comp>1	17%	35%	45%

Notes. Dynamical statistics tested with a double Gaussian distribution with collision angle θ_c =45°. The values indicate the percentage of NG classifications.

presented a similar simulation based on groups of galaxies and showed that the DS test is significantly more sensitive to separations in the redshift space than to separations in projected angular position.

$\theta_c = 90^{\circ}$	Set 1: 25-25	Set 2: 30-20	Set 3: 35-15
$\alpha < 0.05$	3%	9%	15%
$D^* \ge 0.895$	0%	6%	12%
DS p -value<0.05	3%	12%	27%
GMM2D N-comp>1	87%	92%	97%

Table 6.4: Results of 3D merger simulation. $\theta_c = 90^{\circ}$.

Notes. Dynamical statistics tested with a double Gaussian distribution with collision angle θ_c =90° (merger in the plane of the sky). The values indicate the percentage of NG classifications.

6.5 Dynamical state of 138 galaxy clusters

We collected a large sample of 123 GCs from literature and estimated cluster redshifts as explained in § 4.1. We run the dynamical state tests on these clusters and plot the results in figures 6.2 to 6.4 alongside our 15 clusters. The full sample thus consist of 138 GCs. Fig. 6.2 shows the AD's α values against the cluster's number of members where only 19 of the clusters present evidence of perturbations on the velocity distribution. Fig. 6.3 show results for KS test where only 15 clusters are NG. Fig. 6.4 is the same figure but showing the DS p-value, indicating that 21 clusters present evidence of substructure. If we run GMM2D over this sample the number of components found is equal to two for 4 GCs of our SPT sample, 5 GCs from the B16 sample, and 9 GCs from the R14 sample. There are no clusters from the S13 sample that present bimodal projected distributions. Thus, a total of 18 clusters have a bimodal sky distribution as classified by GMM2D.

In Fig. 6.4 two separate groups of clusters with substructure can be identified: a group of clusters with N>50 which consist on SPT-CLJ0600-4353, a cluster from the R14 sample, and 5 clusters from the S13; and a group of clusters with $\sim 20 < N < \sim 35$ which consist on B16 and R14 clusters. In § 6.4 we found that the effects of merger angle and merger ratio affect the outcome of DS test for clusters with mergers with certain characteristics. Since we do not know the separations and ratios of the possible mergers of those clusters with high N_{mem} , the bias of DS test suggested by our results may not be reflected for these clusters. However, GMM2D indeed finds that these clusters have no separable components in the plane of the sky. Suggesting that DS test may be relying only on velocity separations to detect substructure. In the case of the group of clusters with low

number of members, our simulations were not intended for this sample size regime, but the velocity separation of these clusters should be similar or larger than 2σ , as found by (Hou et al., 2012). For the cluster with 3 members from the B16, this cluster has 2 galaxies at less than $\pm 50~\rm km\,s^{-1}$ and one galaxy at 1,122 km s⁻¹. Clearly, DS test took this high velocity galaxy as a substructure, which is in discrepancy with the results of Hou et al. (2012) that found that DS test could never detect substructure with less than 4 members. Finally, a total of 50 clusters (36%) present evidence of disturbance by at least one of AD, GMM2D, or DS test (using the $\pm 3,000~\rm km\,s^{-1}$ velocity cut level). There is only one additional cluster detected only by KS test with evidence of disturbance, thus accounting for 51(37%) GCs.

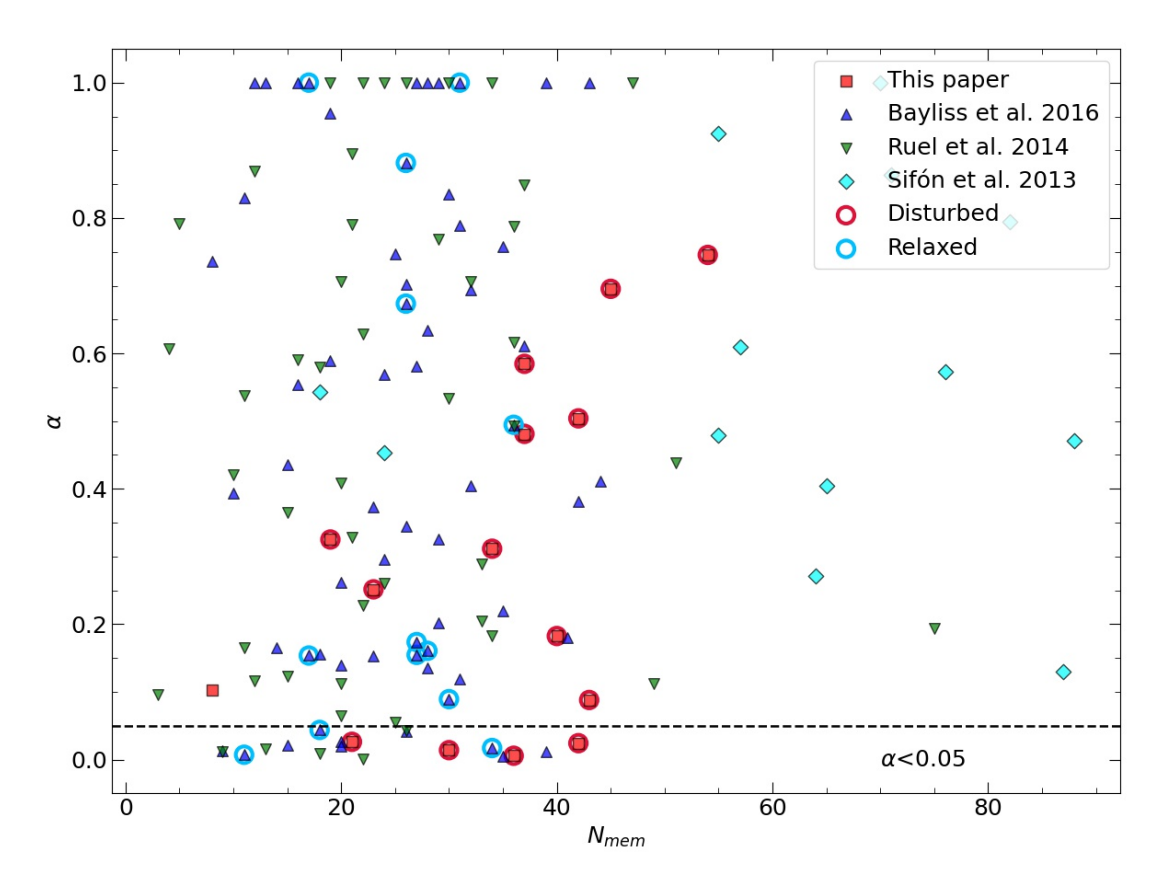


Figure 6.2: α values for 138 galaxy clusters. Cyan dots indicate 13 clusters from the S13 sample, green dots are 48 from the R14 sample, blue are 62 from B16, and red dots are the 15 clusters presented in this paper. The red and lightblue circles mark clusters from the disturbed and the relaxed sample, respectively.

Table 6.5 shows the percentage of NG clusters found by each test. We find that a 63% of the clusters are classified as relaxed by the AD, KS, GMM, and

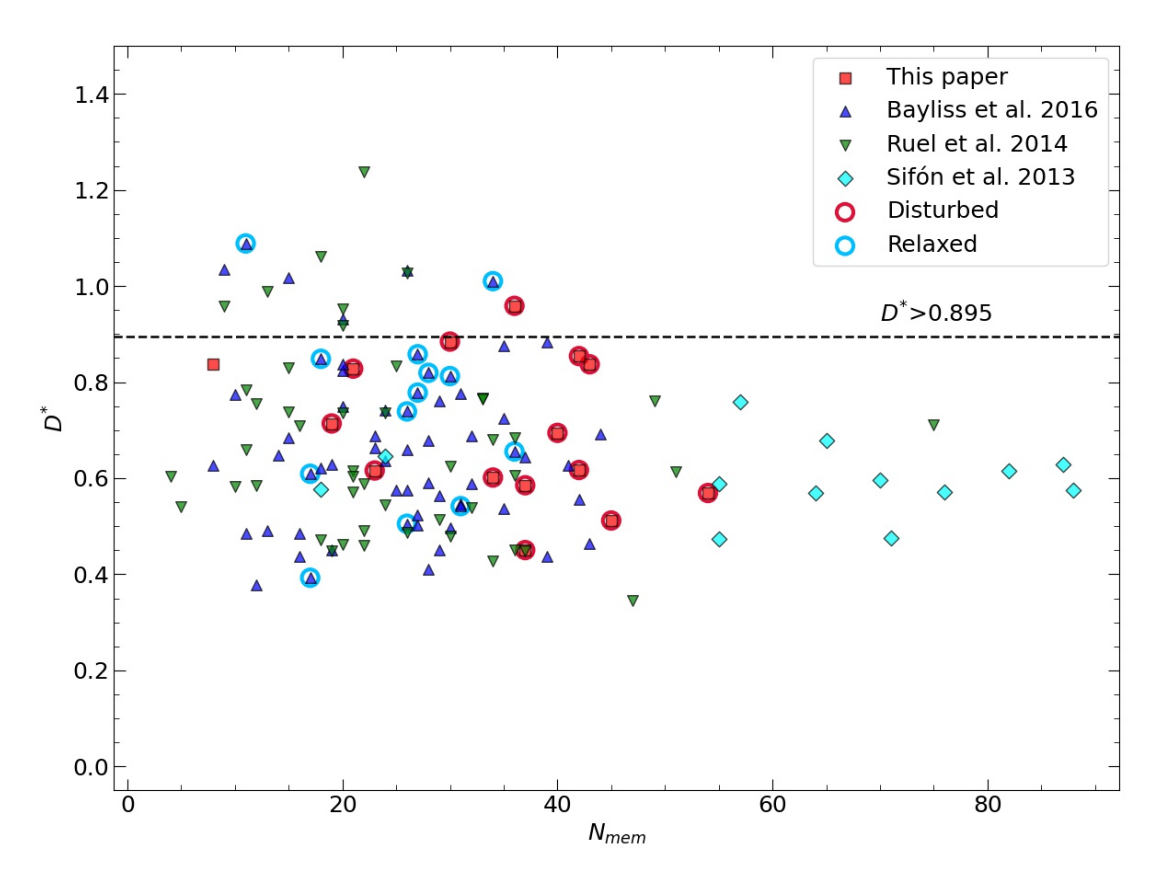


Figure 6.3: D^* values for 138 galaxy clusters.

DS tests for our membership selection criteria of $\pm 3{,}000~\rm km\,s^{-1}$. This percentage is 62% and 65% for the $\pm 2{,}500~\rm km\,s^{-1}$ and $\pm 3\sigma$ velocity cut levels, respectively. Thereby, 75(54%) of the clusters are relaxed by all these tests in all velocity cut levels. The percentage of relaxed clusters found in literature (De Luca et al., 2021, see Table 5) varies significantly, but our results are in the same limits found by works of similar sample size (e.g. >100 GCs with a percentage range of 16% -64%). We highlight the coincidence with the work of Rossetti et al. (2016) who studied 132 SZ-selected GCs and found that 52% \pm 4 of the sample were relaxed systems.

Table 6.5: Percentage of NG classifications by each criteria for 138 galaxy clusters.

	2,500	3,000	3σ
$\alpha < 0.05$	10.9%	13.8%	8.7%
$D* \ge 0.895$	8.7%	10.9%	8.7%
GMM2D N-comp=1	18.1%	13.0%	16.7%
DS p -value<0.05	16.7%	15.2%	15.2%

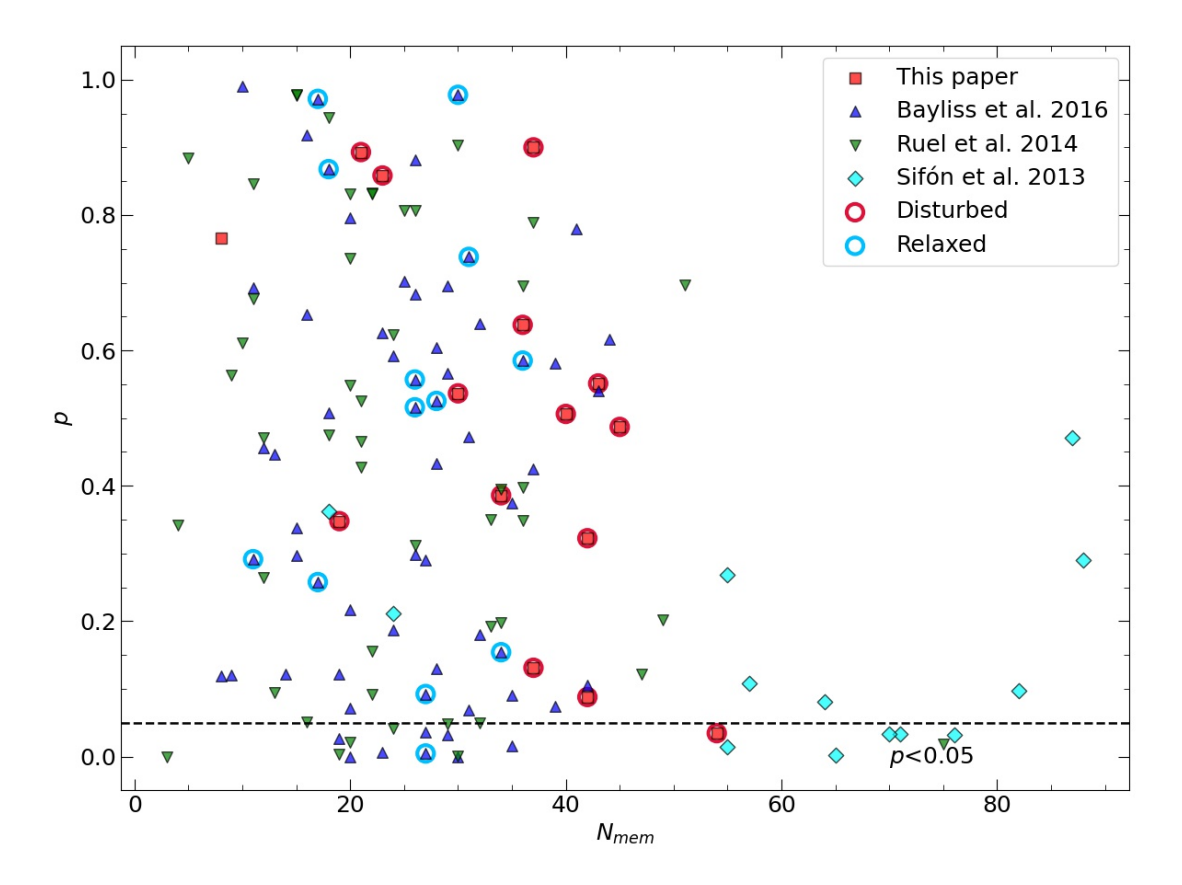


Figure 6.4: DS p-values for 138 galaxy clusters.

6.5.1 Relaxed sample

From the B16 sample, we identify a counter sample of GCs which are also classified as relaxed by Z20. For this section, the 13 relaxed GCs observed in common by B16 and Z20 will be referred as the relaxed sample and the 14 GCs of our sample selected as disturbed by Z20 will be referred as the disturbed sample. As a last approach on the functionality of the tests, we discuss the results on the dynamical state of this counter sample. Table 6.6 shows the cluster parameter estimations for the relaxed sample. The number of galaxy redshifts per clusters for this sample is typically less than 35 members, reaching as low as 10 galaxies.

SPT-CLJ	N_{mem}	z	σ	$M_{200,\rm dyn}^a$	M_{200}^{b}	R_{200}^{b}
			${\rm kms^{-1}}$	$10^{14} M_{\odot}$	$10^{14} M_{\odot}$	[']
J2233-5339	29	0.43977 ± 0.000637	710 ± 123	2.89 ± 1.38	8.23 ± 1.47	4.81
J0334-4659	34	0.486338 ± 0.001013	1212 ± 194	12.24 ± 5.39	8.29 ± 1.43	4.48
J0200-4852	35	0.49911 ± 0.000664	794 ± 125	3.8 ± 1.65	7.13 ± 1.35	4.18
J2232-5959	26	0.594737 ± 0.00103	979 ± 180	6.39 ± 3.23	8.39 ± 1.47	3.89
J0033-6326	13	0.597203 ± 0.00176	1282 ± 336	13.37 ± 9.65	7.12 ± 1.33	3.67
J0243-5930	26	0.634493 ± 0.001011	977 ± 179	6.2 ± 3.14	6.92 ± 1.28	3.48
J0542-4100	31	0.639851 ± 0.000993	1022 ± 171	7.0 ± 3.23	7.82 ± 1.42	3.6
J0352-5647	17	0.649071 ± 0.001037	796 ± 183	3.5 ± 2.21	6.41 ± 1.22	3.34
J2222-4834	27	0.651978 ± 0.001019	1018 ± 183	6.87 ± 3.41	8.22 ± 1.41	3.62
J0123-4821	20	0.654903 ± 0.001808	1467 ± 309	18.72 ± 10.86	6.73 ± 1.31	3.38
J0310-4647	28	0.706655 ± 0.000653	624 ± 110	1.74 ± 0.85	6.53 ± 1.26	3.17
J0406-4805	27	0.735608 ± 0.001301	1225 ± 221	10.87 ± 5.39	7.01 ± 1.26	3.16
J0324-6236	10	0.749882 ± 0.000939	520 ± 157	1.02 ± 0.85	7.57 ± 1.32	3.21

Table 6.6: Spectroscopy results for 13 Z20 relaxed clusters.

Notes. Spectroscopy results for the 13 GCs from the relaxed sample. ^aDynamical mass $M_{200,\rm dyn}$ calculated with Munari et al. (2013) formula (eq. 4.1). ^bMass M_{200} and radius R_{200} extracted from Z20.

In Fig. 6.2 to 6.4 the distributions of the 13 GCs from the relaxed sample and our 14 GCs from the disturbed sample are indicated with lightblue and red circles respectively. These results show mostly no correlation or tendency for the relaxed or disturbed sample. In the case of AD and KS test, this is not surprising as Z20 selection for candidates relies mostly on sky plane direction proxies such as the X-ray morphology and the BCG-X-ray offset. There are no expectations for our relaxed or disturbed candidates to show any kind of convergence with LoS proxies of the dynamical state. In the case of the DS test, which accounts for a 3D approach, the relaxed sample show only 1 cluster with evidence of substructure. Nevertheless, when looking at the continuous distribution of the p-value this sample show no special distribution in comparison to the disturbed sample. As explained in § 6.4, this may reflect the high dependence on velocity separations for the DS test to evaluate disturbance, which may be small in the disturbed sample and unaccounted for in the relaxed sample.

For the projected space analysis, GMM2D favour a distribution with one component through all velocity cut levels for 11 of 13 clusters from the relaxed sample, and only one cluster showed two components at the $\pm 3,000~{\rm km\,s^{-1}}$ velocity cut level. As seen in § 6.2, in the case of the disturbed sample these numbers were 6

and 4, for one and two-component clusters, respectively. Although the correlation with Z20 selection for the disturbed sample is not as significantly as expected, a correlation between GMM2D and the Z20 selection certainly exist for the relaxed sample. There are 9 of the relaxed clusters that show no evidence of perturbation by any test through all velocity cut levels. Since we found that 7 of the disturbed candidates showed evidence of perturbation (4 if only GMM2D), this suggest that the Z20 selection may be better to select relaxed candidates more than disturbed ones. However, the number of members of the relaxed sample is in general lower than 30 galaxies, thus no confident correlation with the Z20 selection of relaxed candidates can be found. Also, the number of spectroscopic members may be too low to resemble the 2D distribution of the clusters. If we use GMM2D over the RCS catalogs taking only galaxies within R_{200} , we find that many of the disturbed clusters show only one sky projected component, including SPT-CLJ0522-5026. Since RCS catalogs have hundreds of galaxies, this suggest that their distributions are too crowded to distinguish any structure and a more rigorous selection of galaxies from the RCS is needed to probe its distribution.

Chapter 7

Future work

The methods and procedures implemented in this study are the basis to characterize dynamically a larger sample of GCs. We look forward to extend the Z20 study by using optical data from the DECam eROSITA Survey (DeROSITAS) on 14,000 square degrees and X-ray data from the space telescope eROSITA on the same area. With this, we will classify the dynamical state of 40,000 GCs and find more clusters like SPT-CLJ0522-5026 and parameterize in detail the mergers using Monte Carlo methods with applications such as the Monte Carlo Merging Analysis Code MCMAC (Dawson, 2013). We will be able to estimate the dynamical mass of the clusters to measure its impact on the scaling relations of massive mergers and relaxed system. We will use spectral features, such as the D4000 intensity, to quantify the impact of the merger in the stellar formation of cluster galaxies. This will allow us to study the properties of galaxy populations like colors, stellar formation, and morphology to correlate them with the dynamical state, mass, and redshift. For SPT-CLJ0522-5026 we have already applied the MCMAC routine to separate the two projected structures found by GMM. The MCMAC method was developed by Dawson (2013) to discern the properties of dissociative mergers and propagate the uncertainty of the measured cluster parameters in an accurate and Bayesian manner. MCMAC gives as a result two different times since collision, TSP0 and TSP1, for an outgoing and an incoming merger, respectively, after the first pericentric passage. It provides the collision angle of the merger, 3D physical distances and velocities, and LoS velocity separation of the components. Table 7.1 shows the results characterizing the state of the merger.

In one hand, NG clusters tend to have larger velocity dispersions and thus, higher dynamical masses (Ribeiro et al., 2011; Old et al., 2018; Morell et al.,

7 Future work 60

Table 7.1: MCMAC results on SPT-CLJ0522-5026.

Param.	Median	Unit	Description
α	47^{+10}_{-11}	deg	Merger axis angle
$d3D_{obs}$	$1.62^{+0.29}_{-0.41}$	Mpc	3D distance of the halos at T obs.
$d3D_{max}$	$2.06^{+0.83}_{-0.34}$	Mpc	3D distance of the halos at apoapsis.
$v3D_{col}$	2616^{+188}_{-134}	$\rm km/s$	3D velocity at collision time.
$v3D_{obs}$	847^{+193}_{-89}	$\mathrm{km/s}$	3D velocity at T obs.
v_{rad}	578^{+106}_{-98}	$\rm km/s$	Radial velocity of the halos at T obs.
TSP0	$0.92^{+0.29}_{-0.18}$	Gyr	TSP for outgoing system.
TSP1	$2.82^{+2.12}_{-0.65}$	Gyr	TSP for incoming system.

2020). However, the velocity distribution of galaxies follow that of dark matter particles (Faltenbacher and Diemand, 2006; Evrard et al., 2008; Lau et al., 2010), in exception to the brightest few galaxies (Lau et al., 2010; Wu et al., 2013). On the other hand, Rines et al. (2016) studied the correlation between SZ and dynamical masses and found that the observed relation agrees very well with a simple virial scaling from mass (based on SZ) to velocity dispersion. Furthermore, SZ masses can overestimate the mass of the cluster when merger perturbations deviates the structure from relaxation (Gianfagna et al., 2021; Gianfagna et al., 2021). In this work we estimated dynamical masses and tried to compare their bias due to dynamical disturbance to that from SZ-based hydrostatic masses. Although, the results showed coherent tendencies for the relaxed and disturbed sample, the uncertainties were too large for anything to be settled. Therefore, these results were discarded. We learn from this study that mergers with different directions in the sky may show contrasting results depending on the dynamical classification proxy used. This discouraged the use of a mass based statistic of dynamical state as they are estimated with methods that are subject to bias from mergers with different collision angles. However, this also drive us to explore gravitational lensing methods in the future to measure weak and strong lensing masses. This will allow us to measure the effect not only of the dynamical state, but also the merger angle on common methods of mass estimation such as the dynamical mass and hydrostatic mass.

In future works we also want to pursue a deeper study on the complex allocation of unrelaxed clusters; massive mergers differ significantly from a simple double Gaussian fusion where factors like the number of components, the separation, the merger ratio or even the membership contamination as well should 7 Future work 61

not be obviated. Notice that an interesting example of this can be seen for SPT-CLJ0337-4928; in Fig. 5.2, the third panel in the right column shows how SPT-CLJ0337-4928 left out 5 galaxies, in the outskirts of the velocity profile, when taking a 3σ velocity cut level. The results of AD and KS test at this velocity cut level find concordance with a G distribution, but also classify this cluster as NG for any other velocity cut level (the which include these outskirt galaxies). This suggest that AD and KS test are unable to recognize the visible central double peak, that has a separation of $\sim 500 \text{ km s}^{-1}$, as something different than a single Gaussian distribution. The same happens for SPT-CLJ0550-5019.

Bibliography

- Allen, S. W., Evrard, A. E., and Mantz, A. B. (2011). Cosmological Parameters from Observations of Galaxy Clusters. *Annual Review of Astronomy & Astrophysics*, 49:409–470.
- Alpaslan, M. (2009). A quick guide to fxcor. arXiv preprint arXiv:0912.4755.
- Athey, T. L., Liu, T., Pedigo, B. D., and Vogelstein, J. T. (2019). Autogmm: Automatic and hierarchical gaussian mixture modeling in python.
- Balestra, I., Mercurio, A., Sartoris, B., Girardi, M., Grillo, C., Nonino, M., Rosati, P., Biviano, A., Ettori, S., Forman, W., Jones, C., Koekemoer, A., Medezinski, E., Merten, J., Ogrean, G. A., Tozzi, P., Umetsu, K., Vanzella, E., van Weeren, R. J., Zitrin, A., Annunziatella, M., Caminha, G. B., Broadhurst, T., Coe, D., Donahue, M., Fritz, A., Frye, B., Kelson, D., Lombardi, M., Maier, C., Meneghetti, M., Monna, A., Postman, M., Scodeggio, M., Seitz, S., and Ziegler, B. (2016). CLASH-VLT: DISSECTING THE FRONTIER FIELDS GALAXY CLUSTER MACS j0416.1-2403 WITH ~800 SPECTRA OF MEMBER GALAXIES. The Astrophysical Journal Supplement Series, 224(2):33.
- Barnacka, A. (2018). Gravitational lenses as high-resolution telescopes. *Physics Reports*, 778:1–46.
- Barrena, R., Girardi, M., and Boschin, W. (2013). The puzzling merging cluster abell 1914: new insights from the kinematics of member galaxies. *Monthly Notices of the Royal Astronomical Society*, 430(4):3453–3464.
- Bayliss, M. B., Ruel, J., Stubbs, C. W., Allen, S. W., Applegate, D. E., Ashby,
 M. L. N., Bautz, M., Benson, B. A., Bleem, L. E., Bocquet, S., Brodwin, M.,
 Capasso, R., Carlstrom, J. E., Chang, C. L., Chiu, I., Cho, H.-M., Clocchiatti, A., Crawford, T. M., Crites, A. T., de Haan, T., Desai, S., Dietrich, J. P.,

Dobbs, M. A., Doucouliagos, A. N., Foley, R. J., Forman, W. R., Garmire, G. P., George, E. M., Gladders, M. D., Gonzalez, A. H., Gupta, N., Halverson, N. W., Hlavacek-Larrondo, J., Hoekstra, H., Holder, G. P., Holzapfel, W. L., Hou, Z., Hrubes, J. D., Huang, N., Jones, C., Keisler, R., Knox, L., Lee, A. T., Leitch, E. M., von der Linden, A., Luong-Van, D., Mantz, A., Marrone, D. P., McDonald, M., McMahon, J. J., Meyer, S. S., Mocanu, L. M., Mohr, J. J., Murray, S. S., Padin, S., Pryke, C., Rapetti, D., Reichardt, C. L., Rest, A., Ruhl, J. E., Saliwanchik, B. R., Saro, A., Sayre, J. T., Schaffer, K. K., Schrabback, T., Shirokoff, E., Song, J., Spieler, H. G., Stalder, B., Stanford, S. A., Staniszewski, Z., Stark, A. A., Story, K. T., Vanderlinde, K., Vieira, J. D., Vikhlinin, A., Williamson, R., and Zenteno, A. (2016). SPT-GMOS: A Gemini/GMOS-South Spectroscopic Survey of Galaxy Clusters in the SPT-SZ Survey. *Astrophys. J. Suppl.*, 227:3.

Beers, T. C., Flynn, K., and Gebhardt, K. (1990). Measures of location and scale for velocities in clusters of galaxies - A robust approach. *Astron. J.*, 100:32–46.

Bleem, L. E., Bocquet, S., Stalder, B., Gladders, M. D., Ade, P. A. R., Allen, S. W., Anderson, A. J., Annis, J., Ashby, M. L. N., Austermann, J. E., Avila, S., Avva, J. S., Bayliss, M., Beall, J. A., Bechtol, K., Bender, A. N., Benson, B. A., Bertin, E., Bianchini, F., Blake, C., Brodwin, M., Brooks, D., Buckley-Geer, E., Burke, D. L., Carlstrom, J. E., Rosell, A. C., Carrasco Kind, M., Carretero, J., Chang, C. L., Chiang, H. C., Citron, R., Moran, C. C., Costanzi, M., Crawford, T. M., Crites, A. T., da Costa, L. N., de Haan, T., De Vicente, J., Desai, S., Diehl, H. T., Dietrich, J. P., Dobbs, M. A., Eifler, T. F., Everett, W., Flaugher, B., Floyd, B., Frieman, J., Gallicchio, J., García-Bellido, J., George, E. M., Gerdes, D. W., Gilbert, A., Gruen, D., Gruendl, R. A., Gschwend, J., Gupta, N., Gutierrez, G., Halverson, N. W., Harrington, N., Henning, J. W., Heymans, C., Holder, G. P., Hollowood, D. L., Holzapfel, W. L., Honscheid, K., Hrubes, J. D., Huang, N., Hubmayr, J., Irwin, K. D., James, D. J., Jeltema, T., Joudaki, S., Khullar, G., Klein, M., Knox, L., Kuropatkin, N., Lee, A. T., Li, D., Lidman, C., Lowitz, A., MacCrann, N., Mahler, G., Maia, M. A. G., Marshall, J. L., McDonald, M., McMahon, J. J., Melchior, P., Menanteau, F., Meyer, S. S., Miquel, R., Mocanu, L. M., Mohr, J. J., Montgomery, J., Nadolski, A., Natoli, T., Nibarger, J. P., Noble, G., Novosad, V., Padin, S., Palmese, A., Parkinson, D., Patil, S., Paz-Chinchón, F., Plazas, A. A., Pryke, BIBLIOGRAPHY 64

C., Ramachandra, N. S., Reichardt, C. L., Remolina González, J. D., Romer, A. K., Roodman, A., Ruhl, J. E., Rykoff, E. S., Saliwanchik, B. R., Sanchez, E., Saro, A., Sayre, J. T., Schaffer, K. K., Schrabback, T., Serrano, S., Sharon, K., Sievers, C., Smecher, G., Smith, M., Soares-Santos, M., Stark, A. A., Story, K. T., Suchyta, E., Tarle, G., Tucker, C., Vanderlinde, K., Veach, T., Vieira, J. D., Wang, G., Weller, J., Whitehorn, N., Wu, W. L. K., Yefremenko, V., and Zhang, Y. (2020). The SPTpol Extended Cluster Survey. *Astrophys. J. Suppl.*, 247(1):25.

- Bleem, L. E., Crawford, T. M., Ansarinejad, B., Benson, B. A., Bocquet, S., Carlstrom, J. E., Chang, C. L., Chown, R., Crites, A. T., Haan, T. d., Dobbs, M. A., Everett, W. B., George, E. M., Gualtieri, R., Halverson, N. W., Holder, G. P., Holzapfel, W. L., Hrubes, J. D., Knox, L., Lee, A. T., Luong-Van, D., Marrone, D. P., McMahon, J. J., Meyer, S. S., Millea, M., Mocanu, L. M., Mohr, J. J., Natoli, T., Omori, Y., Padin, S., Pryke, C., Raghunathan, S., Reichardt, C. L., Ruhl, J. E., Schaffer, K. K., Shirokoff, E., Staniszewski, Z., Stark, A. A., Vieira, J. D., and Williamson, R. (2022). CMB/kSZ and Compton-y Maps from 2500 deg² of SPT-SZ and Planck Survey Data. Astrophys. J. Suppl., 258(2):36.
- Bleem, L. E., Stalder, B., de Haan, T., Aird, K. A., Allen, S. W., Applegate, D. E., Ashby, M. L. N., Bautz, M., Bayliss, M., Benson, B. A., Bocquet, S., Brodwin, M., Carlstrom, J. E., Chang, C. L., Chiu, I., Cho, H. M., Clocchiatti, A., Crawford, T. M., Crites, A. T., Desai, S., Dietrich, J. P., Dobbs, M. A., Foley, R. J., Forman, W. R., George, E. M., Gladders, M. D., Gonzalez, A. H., Halverson, N. W., Hennig, C., Hoekstra, H., Holder, G. P., Holzapfel, W. L., Hrubes, J. D., Jones, C., Keisler, R., Knox, L., Lee, A. T., Leitch, E. M., Liu, J., Lueker, M., Luong-Van, D., Mantz, A., Marrone, D. P., McDonald, M., McMahon, J. J., Meyer, S. S., Mocanu, L., Mohr, J. J., Murray, S. S., Padin, S., Pryke, C., Reichardt, C. L., Rest, A., Ruel, J., Ruhl, J. E., Saliwanchik, B. R., Saro, A., Sayre, J. T., Schaffer, K. K., Schrabback, T., Shirokoff, E., Song, J., Spieler, H. G., Stanford, S. A., Staniszewski, Z., Stark, A. A., Story, K. T., Stubbs, C. W., Vanderlinde, K., Vieira, J. D., Vikhlinin, A., Williamson, R., Zahn, O., and Zenteno, A. (2015). Galaxy Clusters Discovered via the Sunyaev-Zel'dovich Effect in the 2500-Square-Degree SPT-SZ Survey. Astrophys. J. Suppl., 216:27.

BIBLIOGRAPHY 65

Bocquet, S., Saro, A., Mohr, J. J., Aird, K. A., Ashby, M. L. N., Bautz, M., Bayliss, M., Bazin, G., Benson, B. A., Bleem, L. E., Brodwin, M., Carlstrom, J. E., Chang, C. L., Chiu, I., Cho, H. M., Clocchiatti, A., Crawford, T. M., Crites, A. T., Desai, S., de Haan, T., Dietrich, J. P., Dobbs, M. A., Foley, R. J., Forman, W. R., Gangkofner, D., George, E. M., Gladders, M. D., Gonzalez, A. H., Halverson, N. W., Hennig, C., Hlavacek-Larrondo, J., Holder, G. P., Holzapfel, W. L., Hrubes, J. D., Jones, C., Keisler, R., Knox, L., Lee, A. T., Leitch, E. M., Liu, J., Lueker, M., Luong-Van, D., Marrone, D. P., McDonald, M., McMahon, J. J., Meyer, S. S., Mocanu, L., Murray, S. S., Padin, S., Pryke, C., Reichardt, C. L., Rest, A., Ruel, J., Ruhl, J. E., Saliwanchik, B. R., Sayre, J. T., Schaffer, K. K., Shirokoff, E., Spieler, H. G., Stalder, B., Stanford, S. A., Staniszewski, Z., Stark, A. A., Story, K., Stubbs, C. W., Vanderlinde, K., Vieira, J. D., Vikhlinin, A., Williamson, R., Zahn, O., and Zenteno, A. (2015). Mass Calibration and Cosmological Analysis of the SPT-SZ Galaxy Cluster Sample Using Velocity Dispersion σ_v and X-Ray Y $_X$ Measurements. Astrophys. J., 799:214.

- Bouillot, V. R., Alimi, J.-M., Corasaniti, P.-S., and Rasera, Y. (2015). Probing dark energy models with extreme pairwise velocities of galaxy clusters from the DEUS-FUR simulations. *Mon. Not. R. Astron. Soc.*, 450:145–159.
- Bruzual, G. and Charlot, S. (2003). Stellar population synthesis at the resolution of 2003. *Mon. Not. R. Astron. Soc.*, 344:1000–1028.
- Bykov, A. M., Churazov, E. M., Ferrari, C., Forman, W. R., Kaastra, J. S., Klein, U., Markevitch, M., and de Plaa, J. (2015). Structures and Components in Galaxy Clusters: Observations and Models. *Space Science Reviews*, 188:141–185.
- Carroll, B. W. and Ostlie, D. A. (2017). An introduction to modern astrophysics. Cambridge University Press.
- Chadayammuri, U., ZuHone, J., Nulsen, P., Nagai, D., Felix, S., Andrade-Santos, F., King, L., and Russell, H. (2022). Constraining merging galaxy clusters with X-ray and lensing simulations and observations: the case of Abell 2146. Mon. Not. R. Astron. Soc., 509(1):1201–1216.

Cho, H., Jee, M. J., Smith, R., Finner, K., and Lee, W. (2021). Multiwavelength Analysis of A1240, the Double Radio Relic Merging Galaxy Cluster Embedded in a ~80 Mpc-long Cosmic Filament. arXiv e-prints, page arXiv:2109.06879.

- Clowe, D., Bradač, M., Gonzalez, A. H., Markevitch, M., Randall, S. W., Jones, C., and Zaritsky, D. (2006). A direct empirical proof of the existence of dark matter. Astrophys. J. Let., 648:L109–L113.
- Clowe, D., Gonzalez, A., and Markevitch, M. (2004). Weak-Lensing Mass Reconstruction of the Interacting Cluster 1E 0657-558: Direct Evidence for the Existence of Dark Matter. *Astrophys. J.*, 604(2):596-603.
- Coil, A. (2013). The large-scale structure of the universe, ed. *TD Oswalt & WC Keel*, 387.
- Cuciti, V., Cassano, R., Brunetti, G., Dallacasa, D., de Gasperin, F., Ettori, S., Giacintucci, S., Kale, R., Pratt, G. W., van Weeren, R. J., and Venturi, T. (2021). Radio halos in a mass-selected sample of 75 galaxy clusters. II. Statistical analysis. Astron. Astrph., 647:A51.
- D'Agostino, R. and Stephens, M. (1986). Goodness-of-Fit Techniques(New York: Dekker).
- Danese, L., de Zotti, G., and di Tullio, G. (1980). On velocity dispersions of galaxies in rich clusters. *Astron. Astroph.*, 82:322–327.
- David, F. and Johnson, N. (1948). The probability integral transformation when parameters are estimated from the sample. JSTOR, 35(1/2):182-190.
- Davis, M., Huchra, J., Latham, D. W., and Tonry, J. (1982). A survey of galaxy redshifts. ii-the large scale space distribution. *The Astrophysical Journal*, 253:423–445.
- Dawson, W. A. (2013). The Dynamics of Merging Clusters: A Monte Carlo Solution Applied to the Bullet and Musket Ball Clusters. *Astrophys. J.*, 772:131.
- Dawson, W. A., Jee, M. J., Stroe, A., Ng, Y. K., Golovich, N., Wittman, D., Sobral, D., Brüggen, M., Röttgering, H. J. A., and van Weeren, R. J. (2015).
 MC²: Galaxy Imaging and Redshift Analysis of the Merging Cluster CIZA J2242.8+5301. Astrophys. J., 805(2):143.

de los Rios, M., Domínguez R., M. J., Paz, D., and Merchán, M. (2016). The messi (merging systems identification) algorithm and catalogue. *Monthly Notices of the Royal Astronomical Society*, 458(1):226.

- De Luca, F., De Petris, M., Yepes, G., Cui, W., Knebe, A., and Rasia, E. (2021). The Three Hundred project: dynamical state of galaxy clusters and morphology from multiwavelength synthetic maps. *Mon. Not. R. Astron. Soc.*, 504(4):5383–5400.
- Desroches, L.-B., Quataert, E., Ma, C.-P., and West, A. A. (2007). Luminosity dependence in the fundamental plane projections of elliptical galaxies. *Monthly Notices of the Royal Astronomical Society*, 377(1):402–414.
- Doubrawa, L., Machado, R. E. G., Laganá, T. F., Lima Neto, G. B., Monteiro-Oliveira, R., and Cypriano, E. S. (2020). Simulations of gas sloshing induced by a newly discovered gas poor substructure in galaxy cluster Abell 1644. *Mon. Not. R. Astron. Soc.*, 495(2):2022–2034.
- Dressler, A. and Shectman, S. A. (1988). Evidence for substructure in rich clusters of galaxies from radial-velocity measurements. *Astron. J.*, 95:985–995.
- Einstein, A. (1936). Lens-like action of a star by the deviation of light in the gravitational field. *Science*, 84(2188):506–507.
- Evrard, A. E., Bialek, J., Busha, M., White, M., Habib, S., Heitmann, K., Warren, M., Rasia, E., Tormen, G., Moscardini, L., Power, C., Jenkins, A. R., Gao, L., Frenk, C. S., Springel, V., White, S. D. M., and Diemand, J. (2008). Virial Scaling of Massive Dark Matter Halos: Why Clusters Prefer a High Normalization Cosmology. Astrophys. J., 672:122–137.
- Fabricant, D., Cheimets, P., Caldwell, N., and Geary, J. (1998a). The FAST Spectrograph for the Tillinghast Telescope. *Pub. Astron. Soc. Pacific*, 110(743):79–85.
- Fabricant, D. G., Hertz, E. N., Szentgyorgyi, A. H., Fata, R. G., Roll, J. B., and Zajac, J. M. (1998b). Construction of the Hectospec: 300 optical fiber-fed spectrograph for the converted MMT. In D'Odorico, S., editor, Optical Astronomical Instrumentation, volume 3355 of Society of Photo-Optical Instrumentation Engineers (SPIE) Conference Series, pages 285–296.

Faltenbacher, A. and Diemand, J. (2006). Velocity distributions in clusters of galaxies. *Mon. Not. R. Astron. Soc.*, 369:1698–1702.

- Ferrari, C., Benoist, C., Maurogordato, S., Cappi, A., and Slezak, E. (2005). Dynamical state and star formation properties of the merging galaxy cluster Abell 3921. *Astron. Astrph.*, 430:19–38.
- Finn, R. A., Balogh, M. L., Zaritsky, D., Miller, C. J., and Nichol, R. C. (2008). Mass and Redshift Dependence of Star Formation in Relaxed Galaxy Clusters. Astrophys. J., 679(1):279–292.
- Fischer, M. S., Brüggen, M., Schmidt-Hoberg, K., Dolag, K., Ragagnin, A., and Robertson, A. (2021). Unequal-mass mergers of dark matter haloes with rare and frequent self-interactions. *Mon. Not. R. Astron. Soc.*.
- Gao, X. (2018). Memberships of the open cluster NGC 6405 based on a combined method: Gaussian mixture model and random forest. The Astronomical Journal, 156(3):121.
- Gianfagna, G., De Petris, M., Yepes, G., De Luca, F., Sembolini, F., Cui, W., Biffi, V., Kéruzoré, F., Macías-Pérez, J., Mayet, F., Perotto, L., Rasia, E., and Ruppin, F. (2021). Exploring the hydrostatic mass bias in MUSIC clusters: application to the NIKA2 mock sample. *Mon. Not. R. Astron. Soc.*, 502(4):5115–5133.
- Gianfagna, G., Rasia, E., Cui, W., Petris, M. D., and Yepes, G. (2021). The hydrostatic mass bias in the three hundred clusters.
- Gonzalez, E. J., Foëx, G., Nilo Castellón, J. L., Domínguez Romero, M. J., Alonso, M. V., García Lambas, D., Moreschi, O., and Gallo, E. (2015). Low X-ray luminosity galaxy clusters III. Weak lensing mass determination at 0.18 z 0.70. Mon. Not. R. Astron. Soc., 452:2225–2235.
- Goodall, C. (1983). M-estimators of location: An outline of the theory.
- Graham, A. W. (2016). Galaxy Bulges and Their Massive Black Holes: A Review. In Laurikainen, E., Peletier, R., and Gadotti, D., editors, *Galactic Bulges*, volume 418 of *Astrophysics and Space Science Library*, page 263.

Harvey, D., Massey, R., Kitching, T., Taylor, A., and Tittley, E. (2015). The non-gravitational interactions of dark matter in colliding galaxy clusters. *Science*, 347:1462–1465.

- Harvey, D., Tittley, E., Massey, R., Kitching, T. D., Taylor, A., Pike, S. R., Kay, S. T., Lau, E. T., and Nagai, D. (2014). On the cross-section of dark matter using substructure infall into galaxy clusters. *Monthly Notices of the Royal Astronomical Society*, 441(1):404–416.
- Hennig, C., Mohr, J. J., Zenteno, A., Desai, S., Dietrich, J. P., Bocquet, S., Strazzullo, V., Saro, A., Abbott, T. M. C., Abdalla, F. B., Bayliss, M., Benoit-Lévy, A., Bernstein, R. A., Bertin, E., Brooks, D., Capasso, R., Capozzi, D., Carnero, A., Carrasco Kind, M., Carretero, J., Chiu, I., D'Andrea, C. B., daCosta, L. N., Diehl, H. T., Doel, P., Eifler, T. F., Evrard, A. E., Fausti-Neto, A., Fosalba, P., Frieman, J., Gangkofner, C., Gonzalez, A., Gruen, D., Gruendl, R. A., Gupta, N., Gutierrez, G., Honscheid, K., Hlavacek-Larrondo, J., James, D. J., Kuehn, K., Kuropatkin, N., Lahav, O., March, M., Marshall, J. L., Martini, P., McDonald, M., Melchior, P., Miller, C. J., Miquel, R., Neilsen, E., Nord, B., Ogando, R., Plazas, A. A., Reichardt, C., Romer, A. K., Rozo, E., Rykoff, E. S., Sanchez, E., Santiago, B., Schubnell, M., Sevilla-Noarbe, I., Smith, R. C., Soares-Santos, M., Sobreira, F., Stalder, B., Stanford, S. A., Suchyta, E., Swanson, M. E. C., Tarle, G., Thomas, D., Vikram, V., Walker, A. R., and Zhang, Y. (2017). Galaxy populations in massive galaxy clusters to z = 1.1: colour distribution, concentration, halo occupation number and red sequence fraction. Mon. Not. R. Astron. Soc., 467:4015-4035.
- Hernández-Lang, D., Zenteno, A., Diaz-Ocampo, A., Cuevas, H., Clancy, J., Prado P., H., Aldás, F., Pallero, D., Monteiro-Oliveira, R., Gómez, F. A., Ramirez, A., Wynter, J., Carrasco, E. R., Hau, G. K. T., Stalder, B., McDonald, M., Bayliss, M., Floyd, B., Garmire, G., Katzenberger, A., Kim, K. J., Klein, M., Mahler, G., Nilo Castellon, J. L., Saro, A., and Somboonpanyakul, T. (2021). Clash of Titans: a MUSE dynamical study of the extreme cluster merger SPT-CLJ0307-6225. arXiv e-prints, page arXiv:2111.15443.
- Hoekstra, H., Bartelmann, M., Dahle, H., Israel, H., Limousin, M., and Meneghetti, M. (2013). Masses of galaxy clusters from gravitational lensing. Space Science Reviews, 177(1):75–118.

Hou, A., Parker, L. C., Balogh, M. L., McGee, S. L., Wilman, D. J., Connelly, J. L., Harris, W. E., Mok, A., Mulchaey, J. S., Bower, R. G., and Finoguenov, A. (2013). Do group dynamics play a role in the evolution of member galaxies? Mon. Not. R. Astron. Soc., 435(2):1715–1726.

- Hou, A., Parker, L. C., Harris, W. E., and Wilman, D. J. (2009). STATISTICAL TOOLS FOR CLASSIFYING GALAXY GROUP DYNAMICS. *The Astrophysical Journal*, 702(2):1199–1210.
- Hou, Z., Reichardt, C. L., Story, K. T., Follin, B., Keisler, R., Aird, K. A., Benson, B. A., Bleem, L. E., Carlstrom, J. E., Chang, C. L., Cho, H., Crawford, T. M., Crites, A. T., de Haan, T., de Putter, R., Dobbs, M. A., Dodelson, S., Dudley, J., George, E. M., Halverson, N. W., Holder, G. P., Holzapfel, W. L., Hoover, S., Hrubes, J. D., Joy, M., Knox, L., Lee, A. T., Leitch, E. M., Lueker, M., Luong-Van, D., McMahon, J. J., Mehl, J., Meyer, S. S., Millea, M., Mohr, J. J., Montroy, T. E., Padin, S., Plagge, T., Pryke, C., Ruhl, J. E., Sayre, J. T., Schaffer, K. K., Shaw, L., Shirokoff, E., Spieler, H. G., Staniszewski, Z., Stark, A. A., van Engelen, A., Vanderlinde, K., Vieira, J. D., Williamson, R., and Zahn, O. (2012). Constraints on Cosmology from the Cosmic Microwave Background Power Spectrum of the 2500-square degree SPT-SZ Survey. Submitted to Astrophys. J..
- Hubble, E. (1929). A Relation between Distance and Radial Velocity among Extra-Galactic Nebulae. Contributions from the Mount Wilson Observatory, vol. 3, pp.23-28, 3:23-28.
- Hubble, E. P. (1926). Extragalactic nebulae. The Astrophysical Journal, 64.
- Jee, M. J., Hoekstra, H., Mahdavi, A., and Babul, A. (2014). Hubble space telescope/advanced camera for surveys confirmation of the dark substructure in a520. *The Astrophysical Journal*, 783(2):78.
- Kelkar, K., Dwarakanath, K. S., Poggianti, B. M., Moretti, A., Monteiro-Oliveira, R., Machado, R. E. G., Lima-Neto, G. B., Fritz, J., Vulcani, B., Gullieuszik, M., and Bettoni, D. (2020). Passive spirals and shock influenced star formation in the merging cluster A3376. Mon. Not. R. Astron. Soc., 496(1):442–455.
- Kolmogorov, A. (1933). Sulla determinazione empirica di una lgge di distribuzione. Inst. Ital. Attuari, Giorn., 4:83–91.

Kravtsov, A. V. and Borgani, S. (2012). Formation of Galaxy Clusters. *Annual Review of Astronomy & Astrophysics*, 50:353–409.

- Lacey, C. and Cole, S. (1993). Merger rates in hierarchical models of galaxy formation. *Mon. Not. R. Astron. Soc.*, 262:627.
- Lau, E. T., Nagai, D., and Kravtsov, A. V. (2010). Effects of baryon dissipation on the dark matter virial scaling relation. *The Astrophysical Journal*, 708(2):1419.
- Lauer, T. R., Postman, M., Strauss, M. A., Graves, G. J., and Chisari, N. E. (2014). Brightest Cluster Galaxies at the Present Epoch. *Astrophys. J.*, 797:82.
- Lilliefors, H. W. (1967). On the kolmogorov-smirnov test for normality with mean and variance unknown. *Journal of the American Statistical Association*, 62(318):399–402.
- Lin, Y.-T. and Mohr, J. J. (2004). K-band Properties of Galaxy Clusters and Groups: Brightest Cluster Galaxies and Intracluster Light. Astrophys. J., 617:879–895.
- Lloyd, N. S. (1998). The anderson-darling test for normality.
- Lopes, P. A. A. (2007). Empirical photometric redshifts of luminous red galaxies and clusters in the Sloan Digital Sky Survey. *Mon. Not. R. Astron. Soc.*, 380:1608–1620.
- López-Cruz, O., Barkhouse, W. A., and Yee, H. K. C. (2004). The Color-Magnitude Effect in Early-Type Cluster Galaxies. *Astrophys. J.*, 614:679–691.
- Lourenço, A. C. C., Lopes, P. A. A., Laganá, T. F., Nascimento, R. S., Machado, R. E. G., Moura, M. T., Jaffé, Y. L., Ribeiro, A. L., Vulcani, B., Moretti, A., and Riguccini, L. A. (2020). The dynamical state of Abell 2399: a bullet-like cluster. *Mon. Not. R. Astron. Soc.*, 498(1):835–849.
- Lovisari, L., Forman, W. R., Jones, C., Ettori, S., Andrade-Santos, F., Arnaud, M., Démoclès, J., Pratt, G. W., Randall, S., and Kraft, R. (2017). X-ray morphological analysis of the planck ESZ clusters. *The Astrophysical Journal*, 846(1):51.

Ma, C.-J., Ebeling, H., Marshall, P., and Schrabback, T. (2010). The impact of a major cluster merger on galaxy evolution in MACSJ0025.4-1225. *Mon. Not. R. Astron. Soc.*, 406:121–136.

- Mamon, G. A., Biviano, A., and Murante, G. (2010). The universal distribution of halo interlopers in projected phase space. Bias in galaxy cluster concentration and velocity anisotropy? *ArXiv e-prints*.
- Mann, A. W. and Ebeling, H. (2012a). X-ray-optical classification of cluster mergers and the evolution of the cluster merger fraction. *Mon. Not. R. Astron. Soc.*, 420:2120–2138.
- Mann, A. W. and Ebeling, H. (2012b). X-ray-optical classification of cluster mergers and the evolution of the cluster merger fraction. *Mon. Not. R. Astron. Soc.*, 420:2120–2138.
- Mansheim, A. S., Lemaux, B. C., Tomczak, A. R., Lubin, L. M., Rumbaugh, N., Wu, P.-F., Gal, R. R., Shen, L., Dawson, W. A., and Squires, G. K. (2017). Suppressed star formation by a merging cluster system. *Mon. Not. R. Astron. Soc.*, 469:L20–L25.
- Massey, R., Kitching, T., and Nagai, D. (2011). Cluster bulleticity. *Monthly Notices of the Royal Astronomical Society*, 413(3):1709–1716.
- Massey Jr., F. (1951). The kolmogorov-smirnov test for goodness of fit. *Journal* of the American Statistical Association, 46(253):68–78.
- McPartland, C., Ebeling, H., Roediger, E., and Blumenthal, K. (2016). Jellyfish: the origin and distribution of extreme ram-pressure stripping events in massive galaxy clusters. *Mon. Not. R. Astron. Soc.*, 455:2994–3008.
- Menanteau, F., Hughes, J. P., Sifón, C., Hilton, M., González, J., Infante, L., Barrientos, L. F., Baker, A. J., Bond, J. R., Das, S., Devlin, M. J., Dunkley, J., Hajian, A., Hincks, A. D., Kosowsky, A., Marsden, D., Marriage, T. A., Moodley, K., Niemack, M. D., Nolta, M. R., Page, L. A., Reese, E. D., Sehgal, N., Sievers, J., Spergel, D. N., Staggs, S. T., and Wollack, E. (2012). The Atacama Cosmology Telescope: ACT-CL J0102-4915 "El Gordo," a Massive Merging Cluster at Redshift 0.87. Astrophys. J., 748:7.

Menci, N. and Fusco-Femiano, R. (1996). Galaxy velocity dispersion profiles from merging in clusters. *The Astrophysical Journal*, 472(1):46–53.

73

- Monteiro-Oliveira, R., Cypriano, E. S., Machado, R. E. G., Lima Neto, G. B., Ribeiro, A. L. B., Sodré, L., and Dupke, R. (2017). The merger history of the complex cluster Abell 1758: a combined weak lensing and spectroscopic view. *Mon. Not. R. Astron. Soc.*, 466:2614–2632.
- Monteiro-Oliveira, R., Cypriano, E. S., Vitorelli, A. Z., Ribeiro, A. L. B., Sodré, L., Dupke, R., and Mendes de Oliveira, C. (2018). New insights on the dissociative merging galaxy cluster Abell 2034. *Mon. Not. R. Astron. Soc.*, 481:1097–1114.
- Monteiro-Oliveira, R., Morell, D. F., Sampaio, V. M., Ribeiro, A. L. B., and de Carvalho, R. R. (2022). Unveiling the internal structure of the Hercules supercluster. *Mon. Not. R. Astron. Soc.*, 509(3):3470–3487.
- Monteiro-Oliveira, R., Soja, A. C., Ribeiro, A. L. B., Bagchi, J., Sankhyayan, S., Candido, T. O., and Flores, R. R. (2021). Probing Saraswati's heart: evaluating the dynamical state of the massive galaxy cluster A2631 through a comprehensive weak-lensing and dynamical analysis. *Mon. Not. R. Astron. Soc.*, 501(1):756–768.
- Morell, D. F., Ribeiro, A. L. B., de Carvalho, R. R., Rembold, S. B., Lopes, P. A. A., and Costa, A. P. (2020). Classification and evolution of galaxies according to the dynamical state of host clusters and galaxy luminosities. *Mon. Not. R. Astron. Soc.*, 494(3):3317–3327.
- Mostoghiu, R., Knebe, A., Cui, W., Pearce, F. R., Yepes, G., Power, C., Dave, R., and Arth, A. (2019). The Three Hundred Project: The evolution of galaxy cluster density profiles. *Mon. Not. R. Astron. Soc.*, 483(3):3390–3403.
- Moura, M. T., Machado, R. E. G., and Monteiro-Oliveira, R. (2021). Simulations of the merging galaxy cluster Abell 2034: what determines the level of separation between gas and dark matter. *Mon. Not. R. Astron. Soc.*, 500(2):1858–1869.
- Munari, E., Biviano, A., Borgani, S., Murante, G., and Fabjan, D. (2013). The relation between velocity dispersion and mass in simulated clusters of galaxies:

dependence on the tracer and the baryonic physics. Mon. Not. R. Astron. Soc., 430(4):2638–2649.

74

- Muratov, A. L. and Gnedin, O. Y. (2010). MODELING THE METALLICITY DISTRIBUTION OF GLOBULAR CLUSTERS. *The Astrophysical Journal*, 718(2):1266–1288.
- Nurgaliev, D., McDonald, M., Benson, B. A., Bleem, L., Bocquet, S., Forman, W. R., Garmire, G. P., Gupta, N., Hlavacek-Larrondo, J., Mohr, J. J., Nagai, D., Rapetti, D., Stark, A. A., Stubbs, C. W., and Vikhlinin, A. (2017). Testing for X-RaySZ Differences and Redshift Evolution in the X-Ray Morphology of Galaxy Clusters. Astrophys. J., 841:5.
- Old, L., Wojtak, R., Pearce, F. R., Gray, M. E., Mamon, G. A., Sifón, C., Tempel, E., Biviano, A., Yee, H. K. C., de Carvalho, R., Müller, V., Sepp, T., Skibba, R. A., Croton, D., Bamford, S. P., Power, C., von der Linden, A., and Saro, A. (2018). Galaxy Cluster Mass Reconstruction Project III. The impact of dynamical substructure on cluster mass estimates. *Mon. Not. R. Astron. Soc.*, 475(1):853–866.
- Osinga, E., van Weeren, R. J., Boxelaar, J. M., Brunetti, G., Botteon, A., Brüggen, M., Shimwell, T. W., Bonafede, A., Best, P. N., Bonato, M., Cassano, R., Gastaldello, F., di Gennaro, G., Hardcastle, M. J., Mandal, S., Rossetti, M., Röttgering, H. J. A., Sabater, J., and Tasse, C. (2021). Diffuse radio emission from galaxy clusters in the LOFAR Two-metre Sky Survey Deep Fields. *Astron. Astrph.*, 648:A11.
- Owers, M. S., Couch, W. J., Nulsen, P. E. J., and Randall, S. W. (2012). Shocking Tails in the Major Merger Abell 2744. *Astrophys. J. Let.*, 750:L23.
- Pedregosa, F., Varoquaux, G., Gramfort, A., Michel, V., Thirion, B., Grisel, O., Blondel, M., Prettenhofer, P., Weiss, R., Dubourg, V., Vanderplas, J., Passos, A., Cournapeau, D., Brucher, M., Perrot, M., and Édouard Duchesnay (2011). Scikit-learn: Machine learning in python. *Journal of Machine Learning Research*, 12(85):2825–2830.
- Pimbblet, K. A., Drinkwater, M. J., and Hawkrigg, M. C. (2004). Intercluster filaments of galaxies programme: abundance and distribution of filaments

in the 2dfgrs catalogue. Monthly Notices of the Royal Astronomical Society, 354(4):L61–L65.

75

- Pinkney, J., Roettiger, K., Burns, J. O., and Bird, C. M. (1996). Evaluation of Statistical Tests for Substructure in Clusters of Galaxies. *Astrophys. J. Suppl.*, 104:1.
- Pizzolato, F. and Soker, N. (2010). Solving the angular momentum problem in the cold feedback mechanism of cooling flows. *Monthly Notices of the Royal Astronomical Society*, 408(2):961–974.
- Poggianti, B. M., Fasano, G., Omizzolo, A., Gullieuszik, M., Bettoni, D., Moretti, A., Paccagnella, A., Jaffé, Y. L., Vulcani, B., Fritz, J., Couch, W., and D'Onofrio, M. (2016). Jellyfish Galaxy Candidates at Low Redshift. Astron. J., 151:78.
- Porter, S. C. and Raychaudhury, S. (2005). The pisces-cetus supercluster: a remarkable filament of galaxies in the 2df galaxy redshift and sloan digital sky surveys. *Monthly Notices of the Royal Astronomical Society*, 364(4):1387–1396.
- Powell, L. C., Kay, S. T., and Babul, A. (2009). The relationship between substructure in 2d x-ray surface brightness images and weak-lensing mass maps of galaxy clusters: a simulation study. *Monthly Notices of the Royal Astronomical Society*, 400(2):705–730.
- Press, W. H., Teukolsky, S. A., Vetterling, W. T., and Flannery, B. P. (2007). in Numerical recipes: the art of scientific computing. 3rd ed.; Cambridge: Cambridge Univ. Press).
- Psutka, J. V. and Psutka, J. (2019). Sample size for maximum-likelihood estimates of gaussian model depending on dimensionality of pattern space. *Pattern Recognition*, 91:25–33.
- Quintana, H., Carrasco, E. R., and Reisenegger, A. (2000). The Shapley Supercluster. II. Spectroscopic Observations in a Wide Area and General Morphology. Astron. J., 120(2):511–522.
- Ribeiro, A. L. B., Lopes, P. A. A., and Rembold, S. B. (2013). NoSOCS in SDSS. III. The interplay between galaxy evolution and the dynamical state of galaxy clusters. *Astron. Astroph.*, 556:A74.

Ribeiro, A. L. B., Lopes, P. A. A., and Trevisan, M. (2011). Non-Gaussian velocity distributions - the effect on virial mass estimates of galaxy groups. *Mon. Not. R. Astron. Soc.*, 413(1):L81–L85.

- Rines, K. J., Geller, M. J., Diaferio, A., and Hwang, H. S. (2016). HeCS-SZ: THE HECTOSPEC SURVEY OF SUNYAEV–ZELDOVICH-SELECTED CLUSTERS. *The Astrophysical Journal*, 819(1):63.
- Roberts, I. D., van Weeren, R. J., McGee, S. L., Botteon, A., Drabent, A., Ignesti, A., Rottgering, H. J. A., Shimwell, T. W., and Tasse, C. (2021). Lotss jellyfish galaxies: I. radio tails in low redshift clusters.
- Rossetti, M., Gastaldello, F., Ferioli, G., Bersanelli, M., De Grandi, S., Eckert, D., Ghizzardi, S., Maino, D., and Molendi, S. (2016). Measuring the dynamical state of Planck SZ-selected clusters: X-ray peak BCG offset. *Mon. Not. R. Astron. Soc.*, 457:4515–4524.
- Ruel, J., Bazin, G., Bayliss, M., Brodwin, M., Foley, R. J., Stalder, B., Aird, K. A., Armstrong, R., Ashby, M. L. N., Bautz, M., Benson, B. A., Bleem, L. E., Bocquet, S., Carlstrom, J. E., Chang, C. L., Chapman, S. C., Cho, H. M., Clocchiatti, A., Crawford, T. M., Crites, A. T., de Haan, T., Desai, S., Dobbs, M. A., Dudley, J. P., Forman, W. R., George, E. M., Gladders, M. D., Gonzalez, A. H., Halverson, N. W., Harrington, N. L., High, F. W., Holder, G. P., Holzapfel, W. L., Hrubes, J. D., Jones, C., Joy, M., Keisler, R., Knox, L., Lee, A. T., Leitch, E. M., Liu, J., Lueker, M., Luong-Van, D., Mantz, A., Marrone, D. P., McDonald, M., McMahon, J. J., Mehl, J., Meyer, S. S., Mocanu, L., Mohr, J. J., Montroy, T. E., Murray, S. S., Natoli, T., Nurgaliev, D., Padin, S., Plagge, T., Pryke, C., Reichardt, C. L., Rest, A., Ruhl, J. E., Saliwanchik, B. R., Saro, A., Sayre, J. T., Schaffer, K. K., Shaw, L., Shirokoff, E., Song, J., Šuhada, R., Spieler, H. G., Stanford, S. A., Staniszewski, Z., Starsk, A. A., Story, K., Stubbs, C. W., van Engelen, A., Vanderlinde, K., Vieira, J. D., Vikhlinin, A., Williamson, R., Zahn, O., and Zenteno, A. (2014). Optical Spectroscopy and Velocity Dispersions of Galaxy Clusters from the SPT-SZ Survey. Astrophys. J., 792:45.
- Sarazin, C. L. (2002). The Physics of Cluster Mergers, pages 1–38. Springer Netherlands, Dordrecht.

Sarazin, C. L. (2004). Mergers, Cosmic Rays, and Nonthermal Processes in Clusters of Galaxies. *Journal of Korean Astronomical Society*, 37:433–438.

- Saro, A., Mohr, J. J., Bazin, G., and Dolag, K. (2013). Toward unbiased galaxy cluster masses from line-of-sight velocity dispersions. *The Astrophysical Journal*, 772(1):47.
- Schneider, P. (2015). Extragalactic astronomy and cosmology an introduction.
- Sevilla-Noarbe, I., Bechtol, K., Kind, M. C., Rosell, A. C., Becker, M. R., Drlica-Wagner, A., Gruendl, R. A., Rykoff, E. S., Sheldon, E., Yanny, B., Alarcon, A., Allam, S., Amon, A., Benoit-Lévy, A., Bernstein, G. M., Bertin, E., Burke, D. L., Carretero, J., Choi, A., Diehl, H. T., Everett, S., Flaugher, B., Gaztanaga, E., Gschwend, J., Harrison, I., Hartley, W. G., Hoyle, B., Jarvis, M., Johnson, M. D., Kessler, R., Kron, R., Kuropatkin, N., Leistedt, B., Li, T. S., Menanteau, F., Morganson, E., Ogando, R. L. C., Palmese, A., Paz-Chinchón, F., Pieres, A., Pond, C., Rodriguez-Monroy, M., Smith, J. A., Stringer, K. M., Troxel, M. A., Tucker, D. L., de Vicente, J., Wester, W., Zhang, Y., Abbott, T. M. C., Aguena, M., Annis, J., Avila, S., Bhargava, S., Bridle, S. L., Brooks, D., Brout, D., Castander, F. J., Cawthon, R., Chang, C., Conselice, C., Costanzi, M., Crocce, M., da Costa, L. N., Pereira, M. E. S., Davis, T. M., Desai, S., Dietrich, J. P., Doel, P., Eckert, K., Evrard, A. E., Ferrero, I., Fosalba, P., García-Bellido, J., Gerdes, D. W., Giannantonio, T., Gruen, D., Gutierrez, G., Hinton, S. R., Hollowood, D. L., Honscheid, K., Huff, E. M., Huterer, D., James, D. J., Jeltema, T., Kuehn, K., Lahav, O., Lidman, C., Lima, M., Lin, H., Maia, M. A. G., Marshall, J. L., Martini, P., Melchior, P., Miquel, R., Mohr, J. J., Morgan, R., Neilsen, E., Plazas, A. A., Romer, A. K., Roodman, A., Sanchez, E., Scarpine, V., Schubnell, M., Serrano, S., Smith, M., Suchyta, E., Tarle, G., Thomas, D., To, C., Varga, T. N., Wechsler, R. H., Weller, J., and Wilkinson, R. D. (2021). Dark energy survey year 3 results: Photometric data set for cosmology. The Astrophysical Journal Supplement Series, 254(2):24.
- Sifón, C., Hoekstra, H., Cacciato, M., Viola, M., Köhlinger, F., van der Burg, R. F. J., Sand, D. J., and Graham, M. L. (2015). Constraints on the alignment of galaxies in galaxy clusters from ~14 000 spectroscopic members. *Astron. Astrph.*, 575:A48.

Sifón, C., Menanteau, F., Hasselfield, M., Marriage, T. A., Hughes, J. P., Barrientos, L. F., González, J., Infante, L., Addison, G. E., Baker, A. J., Battaglia, N., Bond, J. R., Crichton, D., Das, S., Devlin, M. J., Dunkley, J., Dünner, R., Gralla, M. B., Hajian, A., Hilton, M., Hincks, A. D., Kosowsky, A. B., Marsden, D., Moodley, K., Niemack, M. D., Nolta, M. R., Page, L. A., Partridge, B., Reese, E. D., Sehgal, N., Sievers, J., Spergel, D. N., Staggs, S. T., Thornton, R. J., Trac, H., and Wollack, E. J. (2013). The Atacama Cosmology Telescope: Dynamical Masses and Scaling Relations for a Sample of Massive Sunyaev-Zel'dovich Effect Selected Galaxy Clusters. Astrophys. J., 772:25.

- Smirnov, N. (1948). Table for estimating the goodness of fit of empirical distributions. The annals of mathematical statistics, 19(2):279–281.
- Soja, A. C., Sodré, L., Monteiro-Oliveira, R., Cypriano, E. S., and Lima Neto, G. B. (2018). A Gemini view of the galaxy cluster RXC J1504-0248: insights on the nature of the central gaseous filaments. *Mon. Not. R. Astron. Soc.*, 477:3279–3292.
- Stephens, M. A. (1974). Edf statistics for goodness of fit and some comparisons. Journal of the American Statistical Association, 69(347):730–737.
- Stroe, A., Sobral, D., Paulino-Afonso, A., Alegre, L., Calhau, J., Santos, S., and van Weeren, R. (2017). A large H α survey of star formation in relaxed and merging galaxy cluster environments at z $\sim 0.15-0.3$. Mon.Not.R.Astron.Soc., 465: 2916 2935.
- Tam, S.-I., Jauzac, M., Massey, R., Harvey, D., Eckert, D., Ebeling, H., Ellis, R. S., Ghirardini, V., Klein, B., Kneib, J.-P., Lagattuta, D., Natarajan, P., Robertson, A., and Smith, G. P. (2020). The distribution of dark matter and gas spanning 6 Mpc around the post-merger galaxy cluster MS 0451-03. *Mon. Not. R. Astron. Soc.*, 496(3):4032–4050.
- A. Knebe & V. Muller (1999). Quantifying substructure in galaxy clusters.
- Thompson, R., Davé, R., and Nagamine, K. (2015). The rise and fall of a challenger: the Bullet Cluster in Λ cold dark matter simulations. *Mon. Not. R. Astron. Soc.*, 452:3030–3037.

Tonry, J. and Davis, M. (1979). A survey of galaxy redshifts. I. Data reduction techniques. *Astron. J.*, 84:1511–1525.

- Ueda, S., Ichinohe, Y., Molnar, S. M., Umetsu, K., and Kitayama, T. (2020). Gas Density Perturbations in the Cool Cores of CLASH Galaxy Clusters. Astrophys. J., 892(2):100.
- Wells, L. A. and Bell, D. J. (1994). Cleaning images of bad pixels and cosmic rays using iraf.
- Wen, Z. L. and Han, J. L. (2013). Substructure and dynamical state of 2092 rich clusters of galaxies derived from photometric data. *Mon. Not. R. Astron. Soc.*, 436:275–293.
- Wen, Z. L. and Han, J. L. (2015). Dependence of the bright end of composite galaxy luminosity functions on cluster dynamical states. *Mon. Not. R. Astron. Soc.*, 448:2–8.
- Wittman, D., Golovich, N., and Dawson, W. A. (2017). The Mismeasure of Mergers: Revised Limits on Self-interacting Dark Matter in Merging Galaxy Clusters. *ArXiv e-prints*.
- Wu, H.-Y., Hahn, O., Evrard, A. E., Wechsler, R. H., and Dolag, K. (2013). Virial scaling of galaxies in clusters: bright to faint is cool to hot. *Monthly Notices of the Royal Astronomical Society*, 436(1):460–469.
- Xu, W., Fang, L.-Z., and Wu, X.-P. (2000). Virialization of Galaxy Clusters and Beyond. *Astrophys. J.*, 532:728–739.
- Yahil, A. and Vidal, N. V. (1977). The Velocity Distribution of Galaxies in Clusters. *Astrophys. J.*, 214:347–350.
- York, D. G., Adelman, J., Anderson Jr, J. E., Anderson, S. F., Annis, J., Bahcall, N. A., Bakken, J., Barkhouser, R., Bastian, S., Berman, E., et al. (2000). The sloan digital sky survey: Technical summary. *The Astronomical Journal*, 120(3):1579.
- Yuan, Z. S. and Han, J. L. (2020). Dynamical state for 964 galaxy clusters from Chandra X-ray images. Mon. Not. R. Astron. Soc., 497(4):5485–5497.

BIBLIOGRAPHY 80

Yuan, Z. S., Han, J. L., and Wen, Z. L. (2022). Dynamical state of galaxy clusters evaluated from X-ray images. *arXiv e-prints*, page arXiv:2204.02699.

Zenteno, A., Hernández-Lang, D., Klein, M., Vergara Cervantes, C., Hollowood, D. L., Bhargava, S., Palmese, A., Strazzullo, V., Romer, A. K., Mohr, J. J., Jeltema, T., Saro, A., Lidman, C., Gruen, D., Ojeda, V., Katzenberger, A., Aguena, M., Allam, S., Avila, S., Bayliss, M., Bertin, E., Brooks, D., Buckley-Geer, E., Burke, D. L., Capasso, R., Carnero Rosell, A., Carrasco Kind, M., Carretero, J., Castander, F. J., Costanzi, M., da Costa, L. N., De Vicente, J., Desai, S., Diehl, H. T., Doel, P., Eifler, T. F., Evrard, A. E., Flaugher, B., Floyd, B., Fosalba, P., Frieman, J., García-Bellido, J., Gerdes, D. W., Gonzalez, J. R., Gruendl, R. A., Gschwend, J., Gutierrez, G., Hartley, W. G., Hinton, S. R., Honscheid, K., James, D. J., Kuehn, K., Lahav, O., Lima, M., McDonald, M., Maia, M. A. G., March, M., Melchior, P., Menanteau, F., Miquel, R., Ogando, R. L. C., Paz-Chinchón, F., Plazas, A. A., Roodman, A., Rykoff, E. S., Sanchez, E., Scarpine, V., Schubnell, M., Serrano, S., Sevilla-Noarbe, I., Smith, M., Soares-Santos, M., Suchyta, E., Swanson, M. E. C., Tarle, G., Thomas, D., Varga, T. N., Walker, A. R., Wilkinson, R. D., and DES Collaboration (2020). A joint SZ-X-ray-optical analysis of the dynamical state of 288 massive galaxy clusters. Mon. Not. R. Astron. Soc., 495(1):705-725.

Zenteno, A., Mohr, J. J., Desai, S., Stalder, B., Saro, A., Dietrich, J. P., Bayliss, M., Bocquet, S., Chiu, I., Gonzalez, A. H., Gangkofner, C., Gupta, N., Hlavacek-Larrondo, J., McDonald, M., Reichardt, C., and Rest, A. (2016). Galaxy populations in the 26 most massive galaxy clusters in the South Pole Telescope SPT-SZ survey. Mon. Not. R. Astron. Soc., 462:830–843.

Appendix A

Pipeline and scripts

This section provides code lines details and instructions for the proceedings used in this work. Unless stated otherwise, every script is wrote over Python 3.6.13 (default, Jun 4 2021, 14:25:59) environment. In some cases, IRAF packages are used because we find it more comfortable to use, instead of writing an entire python script for simple tasks.

A.1 Downloading DES images and catalogs

Access to DES database is private and available only to verified accounts, to login into https://deslabs.ncsa.illinois.edu/desaccess/ you should first register following the steps in https://data.darkenergysurvey.org/fnalmisc/onboard/onboard.html. Once access is granted you should login into the DES science database (dessci) and see a series of tools, to download the catalogs we use the DataBase Access tool which allows you to submit your own OracleDB queries directly to the database. You have to use the query editor to compose your database SQL query to retrieve tables with the requested columns from different data releases for a selected sky area.

The following script shows and example used for SPT-CLJ0147-5622, a SPT cluster included in the observation program.

```
SELECT coadd_object_id,ra,dec,mag_auto_g,magerr_auto_g,mag_auto_r

,magerr_auto_r,mag_auto_i,magerr_auto_i,mag_auto_z,magerr_auto_z

,MOF_PSF_MAG_G,MOF_PSF_MAG_ERR_G,MOF_PSF_MAG_R,MOF_PSF_MAG_ERR_R

,MOF_PSF_MAG_I,MOF_PSF_MAG_ERR_I,MOF_PSF_MAG_Z,MOF_PSF_MAG_ERR_Z

,MOF_BDF_MAG_G_CORRECTED,MOF_BDF_MAG_R_CORRECTED,MOF_BDF_MAG_I_CORRECTED
```

```
MOF_BDF_MAG_Z_CORRECTED,FLAGS_FOOTPRINT,FLAGS_BADREGIONS,FLAGS_GOLD

FLAGS_FOREGROUND,EXT_MASH,A_IMAGE,B_IMAGE,THETA_J2000,DNF_ZMC_SOF

NDNF_ZMEAN_SOF,DNF_ZSIGMA_SOF

FROM DES_ADMIN.Y6_GOLD_1_1 WHERE

(ra > 26.5934910432709 AND ra < 27.3369089567291)

AND (dec > -56.58372 AND dec < -56.17208)</pre>
```

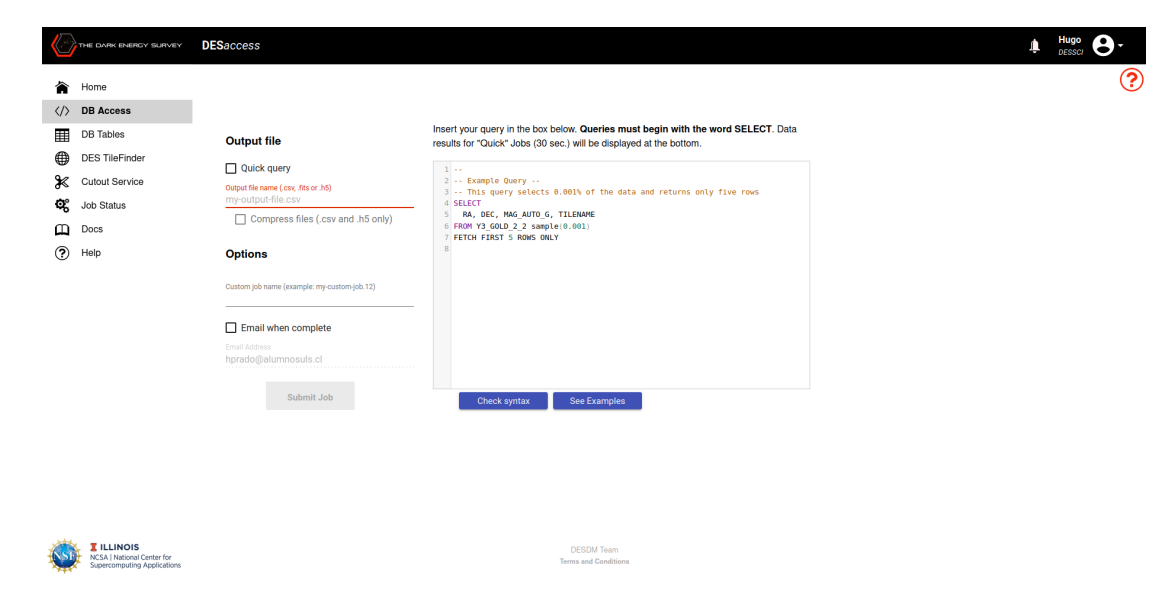
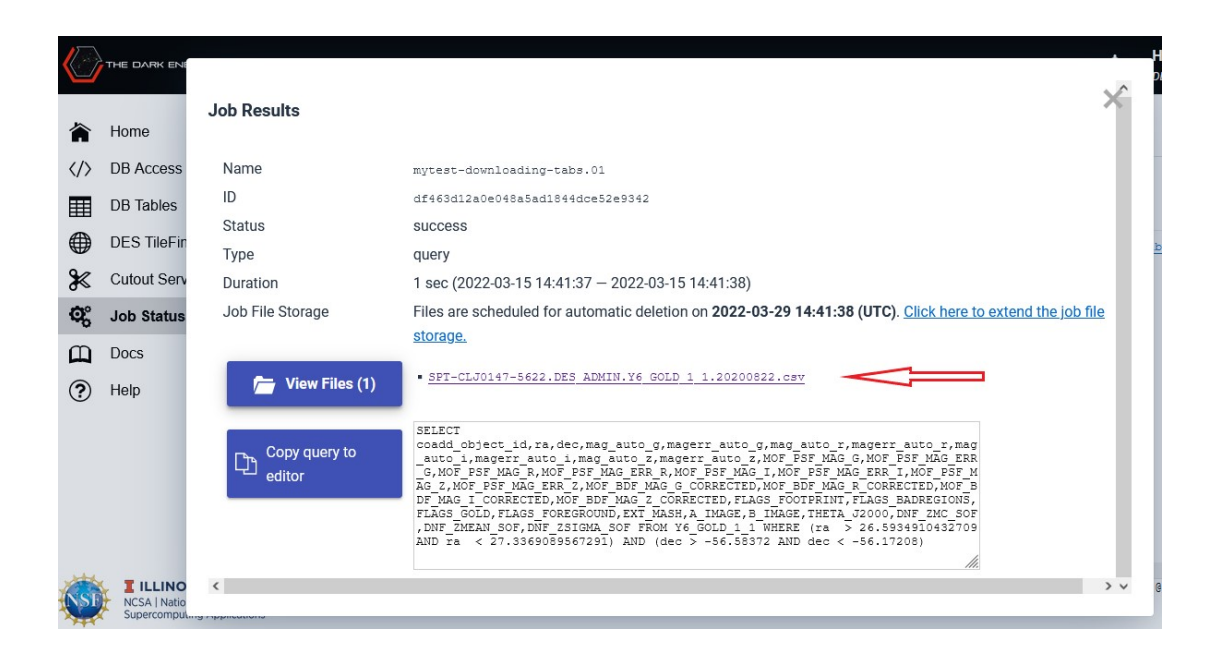


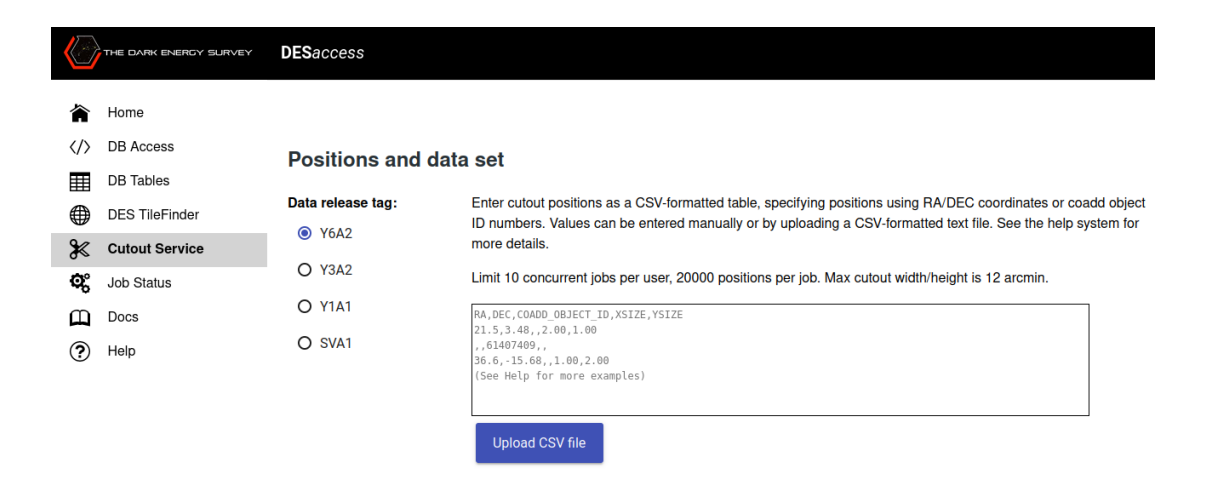
Figure A.1: The DES science DB access tool. The right terminal prompts the SQL command lines where you can check the syntax before submitting the job.

Before submitting a job, you may use the Check syntax to validate your query syntax to avoid failed jobs due to typos. Also, you can select **Quick Query** or specify the output file name to show the resulting table in the web browser or to download a file containing the results. Note that specifying a custom job name in the options section can help make it easier to filter the job list on the Job Status page to find one or more jobs. When the job is submitted, you can download the table by clicking in the job details in the job status tab.

The .fits images can be downloaded from the same page using the Cutout Service which allows you to download raw or color image data based on input coordinates and areal dimensions. First, you have to select the data release tag associated with the data set you wish to access. In the right panel enter the positions in the sky that designate the centers of your cutout images in the form of a CSV-formatted table, with a header row naming the table columns for subse-



quent lines. Note that each position must be specified using either RA/DEC sky coordinates or the Coadd tile ID.



These are some examples of the CSV table that are also in the page's help section showing different cases:

```
RA,DEC,COADD_OBJECT_ID,XSIZE,YSIZE,COLORS_FITS,RGB_STIFF_COLORS,
RGB_LUPTON_COLORS,RGB_MINIMUM,RGB_STRETCH,RGB_ASINH,MAKE_FITS,
MAKE_RGB_STIFF,MAKE_RGB_LUPTON
46.275669,-34.256000,,0.90,1.30,g,gry;riy,,,,true,false,true
,,61407409,1.1,0.8,z,,riy,0.9,40.0,11.0,true,,true
```

This example shows the minimum columns you must include when specifying positions only by coordinates:

```
RA, DEC
2 46.275669,-34.256000
```

or only by Coadd ID

```
1 COADD_OBJECT_ID
2 61407409
3 61407435
```

You have to select the **FITS format** to generate the data files and the bands. You can select one or both of the **color image formats** to generate files suitable for visual inspection. Two color rendering methods are offered: STIFF and Lupton. Note that, for the color image format, exactly three color bands must be selected.



The areal dimensions can be specified in the CSV table by using the columns XSIZE and YSIZE. Otherwise, you can use the bars in the Cutout Size option to give a single size (in arcminutes) for all the images. Finally, after submitting the job and the query is processed, in the job details you will find links to download each of the FITS files corresponding to the selected bands, the RGB images as .png files and a .tar.gz compressed file containing all the requested files.

A.1.1 Donwloading SPT spectroscopic catalogs

The SPT catalogs can be found on the public network in VizieR following the urls¹²³ or by directly searching their corresponding titles. Before submitting the query, be sure to select the cluster identifier, RAJ2000, DEJ2000, and redshift columns. In the preferences panel you can choose the file format for the table. The same procedure must be used to download the Tables with the clusters coordinates to 2D and 3D analysis, in the case of B16 sample the tables should also include the i-band magnitudes for estimation of the relaxation parameter.

A.2 RCS align with saods9

Before entering the official Gemini steps to submit the mask design⁴, you should find proper coordinates and position angle for the mask's frame. This can be perform by using visualization tools to display RGB images in WCS coordinates. For this purpose we use saods9⁵, the following example is a bash command line to generate RGB images in logarithmic scale:

```
ds9 -rgb -red SPT-CLJ2228-5828_i.fits -log -z1 1 -z2 2000
-green SPT-CLJ2228-5828_r.fits -log -z1 1 -z2 2000
-blue SPT-CLJ2228-5828_g.fits -log -z1 1 -z2 2000
```

Using the Zoom/pan zoom rotate parameters module the position angle and center coordinates can be monitored. You should use them in a manner so the highest number of slits can be distributed into cluster galaxies. In our case we also use the -region "file" option to show the positions of RCS galaxies and BCGs, where file should be a proper table containing the coordinates and marker pref-

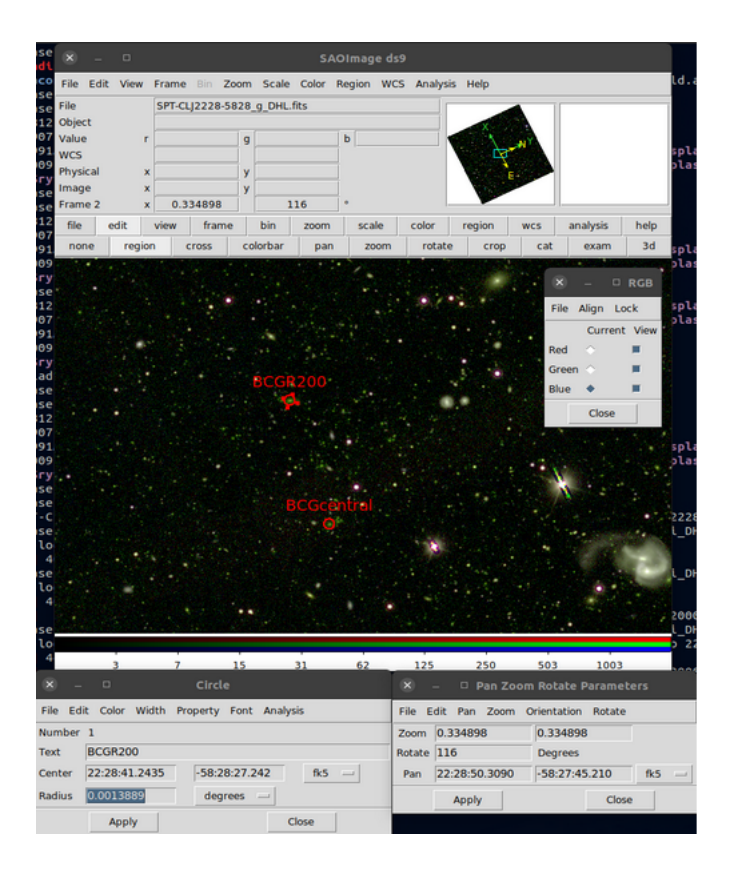
¹B16 release: "Full spectroscopic data release of the SPT-GMOS" in https://vizier.cds.unistra.fr/viz-bin/VizieR-3?-source=J/ApJS/227/3/table3&-out.max=50&-out.form=HTML%20Table&-out.add=_r&-out.add=_RAJ,_DEJ&-sort=_r&-oc.form=sexa

²R14 release: "SPT-SZ survey galaxy clusters optical spectroscopy" in https://vizier.cds.unistra.fr/viz-bin/VizieR-3?-source=J/ApJ/792/45/table3&-out.max=50&-out.form=HTML%20Table&-out.add=_r&-out.add=_RAJ,_DEJ&-sort=_r&-oc.form=sexa

³S13 release: "Massive SZE clusters observations with ACT" in https://vizier.cds.unistra.fr/viz-bin/VizieR-3?-source=J/ApJ/772/25/table&-out.max=50&-out.form=HTML%20Table&-out.add=_r&-out.add=_RAJ,_DEJ&-sort=_r&-oc.form=sexa

⁴e.g. here https://gmmps-documentation.readthedocs.io/en/latest/index.html

⁵https://howtoinstall.co/es/saods9



erences 6 .

A.3 Data reduction

A.3.1 Identifying and correcting first end over-scaled spectra

After the wavelength calibration, some of the spectra presented an abnormal augment at the beginning of the continuum. To correct this we identify spectra with over-scaled edge features by searching for pixels in the first 1,000Å with deviations greater than 5σ from the median of the continuum. When a spectra is identified as over-scaled, we remove all the information before the first pixel without over-escalation after the (over-escaled) maximum identified in the first 1,000Å.

To cut the first end of over-scaled spectra caused by the flux calibration we

⁶documentation in https://ds9.si.edu/doc/ref/region.html

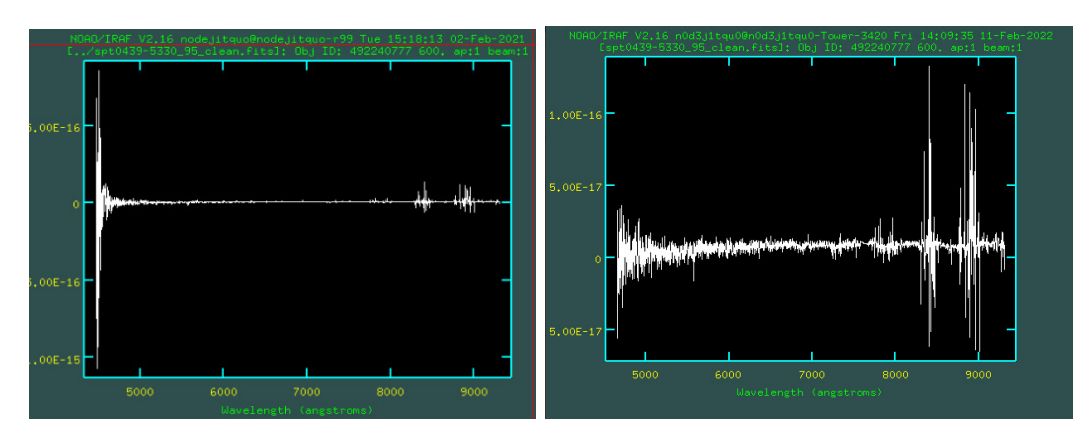


Figure A.2: An example of a first end over-scaled spectra in the left panel. The right panel shows the same spectra after the correction.

use astropy.io.fits module to handle the 1D spectra. The following code lines shows a step by step example for a single 1D spectra and should be iterated over the whole sample: Load the spectra and create a table with the corresponding wavelength of each pixel. Take the CRVAL1 and CDELT1 keywords values from the headers, which are the initial wavelength and resolution of the spectra respectively, to correctly generate the wavelength-pixel relation.

```
from astropy.io import fits
    from astropy.table import Table
2
    import numpy as np
3
    filename = "spt0439-5330_95_clean.fits" #slit 45(i+50) from second mask from 0439
    hdul = fits.open(filename)
6
    data = hdul[0].data
                             #counts
    #generate wavelength from
8
    #CRVAL1(AA), CDELT1(AA/pixel) and range(len(hdul[0].data))
9
    wave = hdul[0].header["CRVAL1"]
10
           + ((hdul[0].header["CDELT1"])*np.array(range(len(data))))
11
    #make wave table: col0: wavelength, col1: counts
    spectra = Table([wave,data])
13
```

Then, identify if the first end of the spectra is over-scaled by comparing it to the median characteristics of the whole spectra.

```
climit = 10

#take the standard deviation

sig = np.std(spectra["col1"])
```

The climit is the minimum sigma deviation and is set to 10 since we find it by visual inspection to be suitable for our case. When an over-scaled spectra is identified, proceed to find a correct wavelength to cut the affected area.

```
climit2 = 5
1
    if oscaled:
2
        #histogram of 100 bins of the first 1000AA
3
        plt.clf()
4
        h = plt.hist(frt[frt["dev"]>=climit2]["col0"]
                      ,bins=int((frt["col0"][len(frt)-1] - frt["col0"][0])/100)
6
                      ,range=[frt["col0"][0],frt["col0"][len(frt)-1]])
        #find index position kmax of the highest peak in hist
8
        for k in range(len(h[0])):
9
            if h[0][k] == np.max(h[0]):
10
                 kamax = k
11
                 break
        #find the first bin after the maximum in kmax which has no over-scalation
13
        for k in range(len(h[0])):
14
            wvpit = spectra[spectra["col0"] >= h[1][k]]
15
            wvpit = wvpit[wvpit["col0"] <= h[1][k+1]]["col1"]</pre>
16
            if k > kamax and h[0][k]==0 and 0.0 not in wvpit:
17
                 wvlim = spectra[spectra["col0"] <= h[1][k]] #find the highest wv</pre>
18
                 wvlim = wvlim[wvlim["col0"] >= h[1][k-1]]
                                                               #with o.s. in the bin
19
                 wvlim = wvlim[wvlim["dev"] >= climit2]
20
                 wvlim = np.max(wvlim["col0"])
22
        #find the pixel of that wavelength
23
        for k in range(len(spectra)):
24
             if spectra["col0"][k] == wvlim:
25
                 kalim = k
26
                 break
27
```

climit2 is the minimum deviation to identify an over-scalated pixel. Finally, with wvlim estimated, you can cut the spectra being careful of keep the same

resolution and correct header keywords (e.g. by using scopy in IRAF or any similar python module).

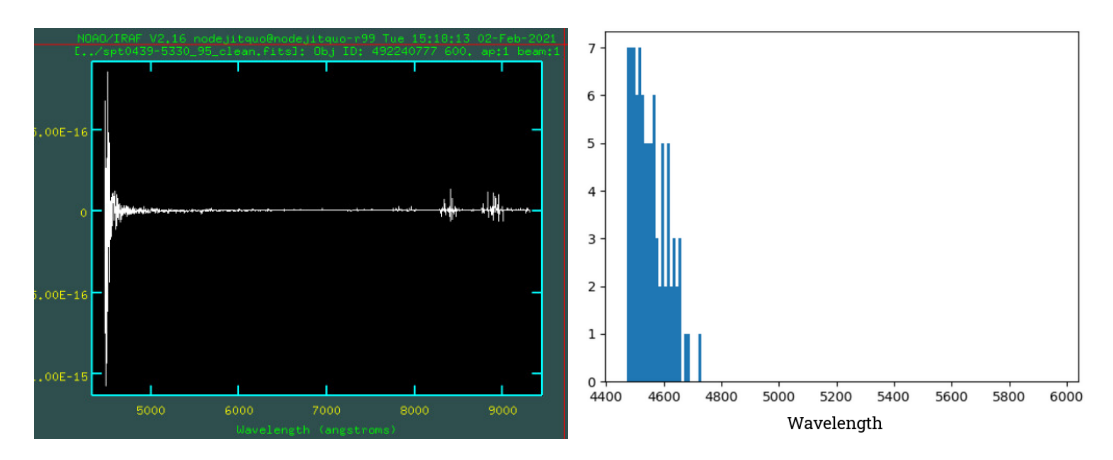


Figure A.3: *left*: Same first end over-scaled spectra of Fig. A.2. *right*: histogram of over-scaled pixels in the first end of the continuum. The resulting wvlim in this example is 4660Å.

A.4 Catalogs and BCG matching

To match the BCG coordinates from Z20 to our catalogs we use the match_to_catalog_sky⁷ task from the astropy.coordinates.SkyCoord module which finds the nearest on-sky matches of a coordinate in a set of catalog coordinates.

The following script shows the implementation of this task to match the BCG coordinates tabulated in a latex file to our cluster catalogs.

```
#match BCGs using match_to_catalog (same result as with TOPCAT)
    #https://docs.astropy.org/en/stable/coordinates/matchsep.html
    def match(cl_lst,filename):
        ext = filename.split(".")[1] #file extension
        #read file with BCG coordinates on literature
        bcg = Table.read(filename,format=ext)
        idx_1st = []
        d2d_1st = []
        for i in range(len(cl_lst)):
                                        #iterate for each cluster
9
            cluster = cl_lst[i]
10
            #load cluster catalog
11
            crt = Table.read("fxcor_"+str(cluster)+"_prom.cat",format="csv")
12
```

⁷https://docs.astropy.org/en/stable/api/astropy.coordinates.match_coordinates_sky.html#astropy.coordinates.match_coordinates_sky

```
if i==0: #create an auxiliary table to save the data
13
                bcg_lst = Table(crt[0])
14
                bcg_lst.remove_row(0)
15
            #locate correct coordinates in the BCG table
16
            sbcg = bcg[bcg["SPT-CL"]=="J"+str(cluster)]
17
            #convert to Skycoord coordinate object
18
            d = SkyCoord(ra=sbcg["RA"][0]*u.degree,dec=sbcg["DEC"][0]*u.degree)
19
            #convert cluster catalog to Skycoord coordinates catalog
20
            catalog = SkyCoord(ra=crt["RA"]*u.degree,dec=crt["DEC"]*u.degree)
21
            #match bcg to catalog
22
            idx, d2d, d3d = d.match_to_catalog_sky(catalog)
23
            d2d_1st += [d2d.value[0]*3600]
                                               #save 2d separation in arcsec
24
            bcg_lst.add_row(crt[idx])
                                         #save best match into aux table
25
        #add useful columns (2d sep and cluster id)
26
        bcg_lst["Z20 match offset (arcsec)"] = d2d_lst
27
        bcg_lst["SPT-CL"] = ["J"+str(clid) for clid in cl_lst]
28
        return bcg_lst
29
```

The bcg table should contain the "SPT-CL" column with the ID of the clusters in format "J2344-4224" as an instance, and coordinates of the corresponding BCGs "RA" and "DEC" in degrees. We first run this script to match the BCGs against all the spectra files, including those rejected in the spectroscopy process, finding best match separations lower than 1" except for two clusters, SPT-CLJ2344-4224 and SPT-CLJ0600-4353. Using TOPCAT to corroborate our results, we get the exact same result finding separations of 57.6" and 25.7" for these clusters, respectively. Visual inspection of the images revealed that there was no spectra of the BCG candidates in our tables and so, we decided to use dedicated time in SOAR/Goodman program to take spectroscopy of the BCG candidates plus other good candidates.

To match the DES catalogs to our cluster galaxies to get magnitudes we implement the same python package. Important details to say is that all the matches have separations lower than 1" and the specific DES magnitude used is "MOF_BDF_MAG_I_CORRECTED" that is the Magneto Optical Filter (MOF) based magnitude of the Bulge+Disk model.

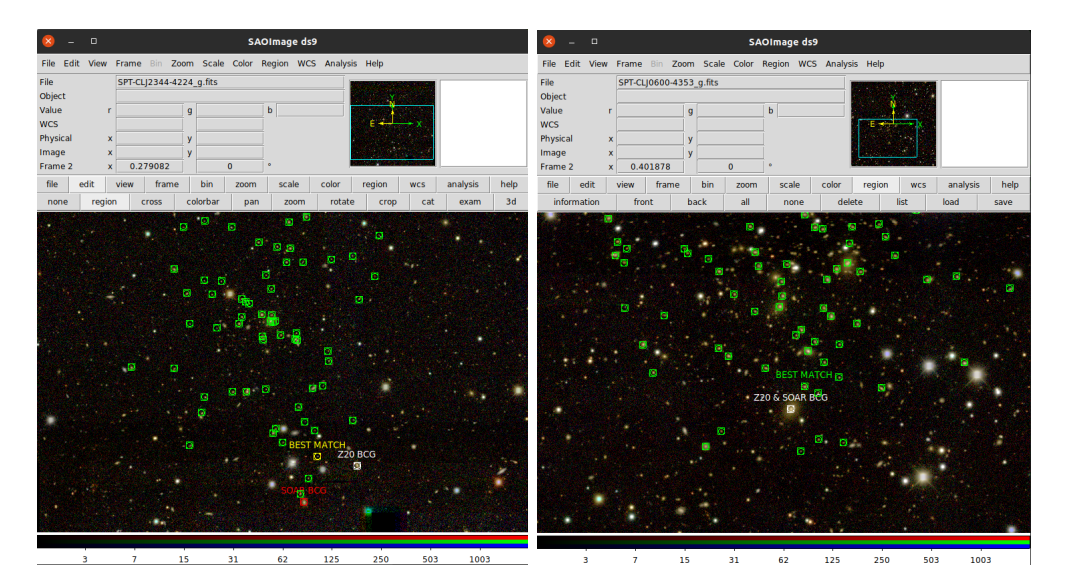


Figure A.4: Saods9 RGB displays of cluster galaxies with BCG candidates, SOAR BCG, and the best match found in our catalogs for both clusters, SPT-CLJ2344-4224 and SPT-CLJ0600-4353.

A.5 Cluster redshifts and dynamical masses

The following script lines come from the zcluster definition which we use to estimate the cluster redshifts and dynamical masses of the clusters. This task involves several python libraries including many astropy modules, also matplotlib, numpy, and uncertainties.ufloat. The installation of any python library should be done via pip⁸.

```
import numpy as np
import matplotlib.pyplot as plt
from astropy.table import Table
import astropy.stats as st
from astropy.constants import c
from astropy import units as u
from astropy.cosmology import FlatLambdaCDM
from uncertainties import ufloat

#
c = c.to(u.km/u.s).value
cosmo = FlatLambdaCDM(HO=68.3,OmO=0.299) #Bocquet et al. 2015 cosmology
#
```

To handle the redshifts of the galaxies notice that fxcor measure $\log(z+1)$,

⁸https://pypi.org/project/pip/

then calculates the velocity as $c(10^{(l)}\log(z+1))-1)=cz$, and finally it multiples for the corresponding factor to estimate relative, observed and heliocentric velocities (Alpaslan, 2009).

```
cl_lst = ["2344-4224","0151-5654","0144-4807","0600-4353","2358-6129"
                     ,"0451-4952","0354-5904","0439-5330","0337-4928","0111-5518"
2
                     ,"0135-5904","0522-5026","2100-5708","0612-4317","0550-5019"]
3
    for r in range(len(cl_lst)): #iterate on every cluster
4
        plt.clf()
5
        cluster = cl_lst[r]
6
        #load cluster catalog
7
        crt = Table.read(path+"fxcor_"+str(cluster)+"_prom.cat",format="csv")
        x = crt["VEL_HEL"]
9
        x = np.array(x,dtype="float64")
10
        x.sort()
11
        x = x/c
                   #to get redshifts make VEL_HEL/c
12
```

Then, to get the initial guess on the cluster redshift we generate an histogram of bin size 0.005 and take the center of the bin with the highest peak.

```
#----#
1
   binval = 0.005
2
    upper = (np.around((x[len(x)-1]/binval))+1)*binval
   lower = (np.around(x[0]/binval)-1)*binval
    nbin = int(np.around((upper-lower)/binval))
    h = plt.hist(x,bins=nbin,range=(lower,upper))
6
    #----#
7
    for i in range(len(h[0])):
8
       if h[0][i] == max(h[0]):
9
           lo = h[1][i]
10
           up = h[1][i+1]
11
           zpeak = (lo+up)/2
12
```

This way we can take all the galaxies within $\pm 5{,}000~\rm km\,s^{-1}$ (or $\pm 2{,}500~\rm km\,s^{-1}$, see § 4.1) and improve the estimate of the central location by iterating the biweight location estimator, which is usually rapid and require only a few steps (Beers et al., 1990).

```
#---5,000km/s_cut----#
    initcut = 5000 #5,000 kms initial cut
    zcl = zpeak
    #Danese, L., de Zotti, G., & di Tullio, G. 1980, A&A, 82, 322
    crt["PEC_VEL"] = (((crt["VEL_HEL"]/c) - zcl)/(1+zcl))*c
    #---peculiar velocities and velocity cut
    clip = crt[abs(crt["PEC_VEL"]) <= initcut]</pre>
    if len(clip) <= 15:
        hinit = initcut/2 #2,500 kms
        clip = crt[abs(crt["PEC_VEL"]) <= hinit]</pre>
10
    \#---initial\_biweight\_iteration---\#
11
    for 1 in range(3):
12
        zcl = st.biweight_location(clip["VEL_HEL"]/c,M=np.array([zcl]))
13
        #improve initial quess before 3sigma clipping (Beers et al. 1990)
```

Finally, we use the 3σ -clipping method to find a final redshift. The following script lines come from the **zcluster** definition which we use to estimate the cluster redshifts and dynamical masses of the clusters.

```
#---sigma_clippping----#
    while True:
2
        #---cluster redshift
3
        zcl = st.biweight_location(clip["VEL_HEL"]/c,M=np.array([zcl]))
4
        #---update PEC_VEL
        clip.remove_column("PEC_VEL")
6
        clip["PEC_VEL"] = (((clip["VEL_HEL"]/c) - zcl)/(1+zcl))*c
        #---Sigma Biweight
        sigma_bi = st.biweight_scale(clip["PEC_VEL"], M=np.array([0.0]))
9
        #-----Sigma Gapper (as Hou et al. 2009)
10
        clip.sort("PEC_VEL")
11
        n = len(clip)
        p = []
13
        for 1 in range(1,n):
                                \#l=1, ..., n-1
14
            w = 1*(n-1)
15
            g = clip["PEC_VEL"][1] - clip["PEC_VEL"][1-1]
            p += [w*g]
17
        sigma_g = (np.sqrt(np.pi)*np.sum(p))/(n*(n-1))
18
        #----sigma to use depending on memebers (Bayliss et al 2016)
19
        if n >= 15:
20
            sigma = sigma_bi
        elif n < 15:
22
```

```
sigma = sigma_g
23
        #---rejected_galaxies
24
        rej = clip[abs(clip["PEC_VEL"]) >= (s*sigma)]
25
        #---when there are no rejected galaxies end the iteration and
26
        #calculate sigma error
27
        if len(rej) == 0:
            #Ruel, J., Bazin, G., Bayliss, M., et al. 2014, ApJ, 792, 45
29
            sigma_err = 0.92*sigma/np.sqrt(len(clip)-1)
            if sigma == sigma_g:
31
                sigma_err = 0.91*sigma/np.sqrt(len(clip)-1)
            break
33
        #---if len(rej)!=0 then cut in s*sigma and start over again
34
        clip = clip[abs(clip["PEC_VEL"]) <= (s*sigma)]</pre>
35
    #---uncertainty
36
    zcl_err = np.std(clip["VEL_HEL"]/c)/np.sqrt(len(clip))
    #---update pec velocities on the crate, then save
38
    crt.remove_column("PEC_VEL")
39
    crt["PEC_VEL"] = (((crt["VEL_HEL"]/c) - zcl)/(1+zcl))*c
40
    crt.write(path+"fxcor_"+str(cluster)+"_prom.cat",format="csv"
41
               ,overwrite="True")
    ns3 = len(clip) #---how many galaxies survive the 3 sigma clipping
43
    #(not the same as member galaxies)
```

This in return provides the cluster redshift zcl, its uncertainty zcl_err, velocity dispersion sigma and its uncertainty sigma_err. Finally, to estimate the dynamical masses we use Bocquet et al. (2015) cosmology on the scaling relation calibrated by Munari et al. (2013).

```
#-----dynamicalmass------#

hz = cosmo.H(z=zcl).value /100

###################

#Munari et al. 2013

A = ufloat(1177,4.2)

munalpha = ufloat(0.364,0.002)

sss = ufloat(sigma,sigma_err) #1D velocity dispersion

Mdynu = (((sss/A)**(1/munalpha))*10)/hz #*1e14 Msun

Mdyn = Mdynu.nominal_value #dynamical mass

Mdyn_err = Mdynu.std_dev #uncertainty
```

A.6 Dynamical state indicators

A.6.1 AD and KS test

To perform this task we execute the module normal_ad from the python package statsmodels on the proper velocities of member galaxies for each cluster. The package normal_ad⁹ takes an array of ordered values to return A^2 . For the array data x the python syntax is

```
from statsmodels.stats.diagnostic import normal_ad
import numpy as np

aa, paa = normal_ad(np.sort(x))
```

where **aa** is the A^2 statistic. This value is then used to calculate equations 4.2 and 4.3.

```
a, b = 3.6789468, 0.1749916 #Nelson et al. 1998
2 aastar = (aa)*(1+(0.75/len(x)) + (2.25/(len(x)**2)))
3 alpha_ad = a*np.exp(((-1)*aastar)/b)
4 if alpha_ad > 1: #dont care about alpha >1 so here I limit it to 1
5 alpha_ad = 1
```

This in return provide the α statistic alpha_ad capped to 1.

For KS test, we use the module $lilliefors^{10}$ from the same python package. This will calculate the D statistic which is then used to calculate eq. 4.7. For the array data \mathbf{x} the python syntax is

```
from statsmodels.stats.diagnostic import lilliefors as liltest

D, pD = liltest(np.sort(x),dist="norm",pvalmethod="table")

Dstar = D*(np.sqrt(len(x)) - 0.01 + (0.85/np.sqrt(len(x))))
```

 $^{^9 \}rm https://www.statsmodels.org/stable/generated/statsmodels.stats.diagnostic.normal_ad.html$

¹⁰https://www.statsmodels.org/stable/generated/statsmodels.stats.diagnostic.
lilliefors.html

This in return provides the D^* statistic.

A.6.2 Gaussian Mixture Modelling

GaussianMixture¹¹ is a module from the package sklearn.mixture that makes a representation of a Gaussian mixture model probability distribution to estimate the parameters of a Gaussian mixture distribution. We use this module taking diagonal covariance matrices for each component. Also, this module is fully scalable to 3 dimensional analysis and we tried to add the velocity phase space together with the sky plane positions, this scenario requires a normalization of the parameters to avoid differences in magnitudes or scales of the attributes of the measures (Gao, 2018), but this configuration yield inconsistent results and so we decided to use it only for sky plane analysis.

To work the sky plane coordinates we first convert the sky positions of the galaxies into 2D physical positions. For this, we set the Bocquet et al. (2015) cosmology and then estimate separations, from the center of the cluster in Mpc, by assuming that all the galaxies are at the same redshift as the cluster redshift.

```
import numpy as np
1
    from astropy.table import Table
2
    from astropy.cosmology import FlatLambdaCDM
3
    cosmo = FlatLambdaCDM(H0=68.3,0m0=0.299) #Bocquet et al. 2015 cosmology
4
5
    cluster = "2344-4224"
6
    velcut=3000
    crt = Table.read("fxcor_"+cluster+"_prom.cat",format="csv") #load catalog
8
    clip = crt[abs(crt["PEC_VEL"])<=velcut] #membership selection</pre>
    coocl = Table.read("clcenter_z20.latex",format="latex") #load table with Z20 centers
10
    #take ra, dec of the corresponding center from Z20
11
    ra = float(coocl[coocl["SPT-CL"] == "J"+str(cluster)]["RA"][0])
12
    dec = float(coocl[coocl["SPT-CL"] == "J"+str(cluster)]["DEC"][0])
13
    #convert center and catalog coordinates to SkyCoord object
14
    d = SkyCoord(ra*u.degree,dec*u.degree)
15
    catalog = SkyCoord(ra=clip["RA"]*u.degree,dec=clip["DEC"]*u.degree)
16
    #position angle of catalog galaxies with respect to center
17
    pa = d.position_angle(catalog)
18
    lst = d.separation(catalog).to(u.arcsec) #separation in arcsec
```

 $^{^{11}} https://scikit-learn.org/stable/modules/generated/sklearn.mixture. \\ Gaussian Mixture.html$

```
#angular diameter distance at cluster redshift
d_A = cosmo.angular_diameter_distance(z=zcl)
distance_Mpc = (lst*d_A).to(u.Mpc,u.dimensionless_angles()) #distance in Mpc
#X, Y coords in Mpc of each galaxy centered on the cluster center
Y = distance_Mpc*np.cos(pa)
X = distance_Mpc*np.sin(pa)
clip["PRJ_SEP"] = distance_Mpc #save to clip
clip["X"] = X
clip["Y"] = Y
clip["PA"] = pa
```

This example for SPT-CLJ2344-4224 member galaxies (i.e. within $\pm 3,000$) calculates X, Y distances in Mpc to the center of the cluster. We then generate a suitable array for GaussianMixture to process, a list of K modes and run the module.

```
import numpy as np
    from astropy.table import Table, join
2
            #maximum number of K modes
    cmp=2
    #generate 2D array with coordinates
    points = np.array([np.array(clip["X"]),np.array(clip["Y"])])
    points = points.T
    N = np.arange(1, cmp+1)
                               \#array 1, 2, \ldots, K
    #GMM for each K model
    models = [None for k in range(len(N))]
10
    for k in range(len(N)):
        models[k] = GaussianMixture(n_components=N[k],covariance_type="diag").fit(points)
12
    BIC = [m.bic(points) for m in models] #take BIC of the models
    gmmtab = Table([BIC,N])
                               #tabulate BIC with K model
14
    gmmtab.sort("col0")
15
    #take diff between first and second best model
16
    delta_bic = abs(gmmtab["col0"][0] - gmmtab["col0"][1])
17
    #take K of the best model
   N2_BIC = int(gmmtab[gmmtab["col0"]==np.min(gmmtab["col0"])]["col1"])
```

This provides the number of 2D components N2_BIC when considering up to 2 main components. The next script shows how to extract useful data from the fit to make the figures in 5.3.

```
best_gmm = models[N2_BIC-1] #select best model
1
    #----take labels, centers, and sigmas of each group in the model
2
    labs = best_gmm.predict(points)
3
    labs = Table(np.reshape(np.array(labs),[len(labs),1])) #reshape to column like array
    centers = best_gmm.means_ #centers of the components
    sigmas_lst = np.sqrt(best_gmm.covariances_) #take spatial Mpc dispersion of each mode
    clip["gmmlabels"] = labs["col0"]
                                        #save labels of mode membership: 0,1,\ldots,K-1
    #save centers and X, Y sigmas of the corresponding component for each galaxy
    X_{lst} = []
    Y_lst = []
10
    Xsig_lst = []
11
    Ysig_lst = []
12
    for k in range(len(clip)):
13
        X_lst += [centers[clip["gmmlabels"][k]][0]]
14
        Y_lst += [centers[clip["gmmlabels"][k]][1]]
15
        Xsig_lst += [sigmas_lst[clip["gmmlabels"][k]][0]]
16
        Ysig_lst += [sigmas_lst[clip["gmmlabels"][k]][1]]
17
    clip["gr_X"] = X_lst
18
    clip["gr_Y"] = Y_lst
19
    clip["grsig_X"] = Xsig_lst
20
    clip["grsig_Y"] = Ysig_lst
21
    clip.write("gmm2dlabs_"+str(cluster)+"_"+str(velcut)+".csv",format="csv"
22
                , overwrite=True)
```

These proceedings are then iterated for each cluster and velocity cut level.

A.6.3 DS test and Monte Carlo method

DS test analyze the the spatial distribution of galaxies estimating Δ/N by considering the spatial and velocity distribution of the galaxies. The p-value is estimated by using Monte Carlo methods. For the cluster SPT-CLJ2344-4224 at redshift zcl with velocity dispersion sigma, the following scripts dictates how we esimate the DS p-value for the member galaxies of this cluster.

```
import numpy as np
from astropy.table import Table

cluster = '2344-4224' #cluster ID

zcl = 0.282384 #cluster redshift
sigma = 906 #velocity dispersion
```

```
velcut = 3000
                    #velocity cut level
    crt = Table.read(path+"fxcor_"+str(cluster)+"_prom.cat",format="csv") #load catalog
    clip = crt[abs(crt["PEC_VEL"])<=velcut] #velocity cut</pre>
    #-----#
    # Einasto et al. (2012)
11
   X = clip
    cz = X["PEC_VEL"]
                      #take peculiar velocities
13
    cz = np.array(cz,dtype="float")
   N = len(X)
                      #sample size
15
   n = int(round(np.sqrt(N)))
                               #<----Pinkney et al. (1996)
16
    #locate n nearest neighbors of each galaxy
   X['index'] = [np.empty((n,)).tolist()] * N
18
    for (p, j, id) in zip(np.array(X["X"]), np.array(X["Y"]), np.arange(len(X["index"]))):
        galsky = np.sqrt((X["X"] - p)**2 + (X["Y"] - j)**2)
20
        idx_lst = galsky.argsort()
21
        #save array of indexes of the neighbors for each galaxy
22
        X["index"][id] = list(idx_lst[1:n+1])
    delta = []
    for k in X["index"]: #iterate for each group of neighbors
25
        cz_local = cz[np.array(k,dtype="int")] #take peculiar velocities
        delta += [((n+1)/(sigma**2)) * ((cz_local.mean())**2
27
                                              + (cz_local.std() - sigma)**2)]
    delta_original = np.sqrt(np.array(delta)).sum()
29
```

Then to estimate the p-value,

```
import random
2
    import os
3
    #Monte Carlo shuffling definition
4
    def montecarlo(data, output, sigma):
        cz = np.array(data["PEC_VEL"])
6
        N = len(data)
7
        n = int(round(np.sqrt(N))) #<----Pinkney et al. (1996)
8
                                   #now we shuffle the velocities keeping the coordinates
        random.shuffle(cz)
9
        delta = []
10
        for i in data['index']:
                                    #iterate over shuffled velocities
11
            cz_local = cz[np.array(i,dtype="int")] #take s. velocities of the neighbors
12
            delta += [((n+1)/(sigma**2)) * ((cz_local.mean()**2))
13
                                              + (cz_local.std() - sigma)**2)]
14
        output.put(np.sqrt(np.array(delta)).sum())
16
```

```
#----create directory for temp files
        os.makedirs('DSTEST/dstest')
18
    except Exception as error:
19
        #directory already exists
20
        pass
21
    for k in range(50):
                              #make montecarlo 5,000 iterations (50x100)
        output = mp.Queue()
23
        processes= [mp.Process(target=montecarlo, args=(X[['PEC_VEL', 'index']], output,
^{24}
                                                           sigma)) for l in range(100)]
25
        for p in processes:
26
            p.start()
        for p in processes:
28
            p.join()
        pickle.dump(np.array([output.get() for p in processes])
30
                     ,open('DSTEST/dstest/\%s_\%s.out'\%(str(cluster), k),'wb'))
    data = np.array([])
32
    for k in range(50):
33
        data = np.append(data, pickle.load(open('DSTEST/dstest/\%s_\%s.out'\%(str(cluster))
34
                                                  , k), 'rb')))
35
    #----fraction of elements above the value of the original delta (Hou et al 2009)
    pds = len(data[ data>delta_original])/len(data)
37
```

We then iterate over the clusters to find each pds. When estimating the p-value for the 138 SPT clusters we only use 1,000(20x50) iterations to save computation time.

A.7 Sample size statistics for 1D dynamical tests

The following series of scripts dictates how we find the minimum number of galaxies for AD and KS test to work efficiently in a bimodal distribution scenario with scales and parameters extracted from our clusters.

First, we fit a double Gaussian distribution via least-square fitting of the velocity profile.

```
import numpy as np
from astropy.table import Table
from lmfit import Model

#
def double_gaussian(X, amp1, mu1, sig1, amp2, mu2, sig2):
    return (amp1 * np.exp(-((X-mu1)**2)/(2*(sig1**2))))
```

```
+ (amp2 * np.exp(-((X-mu2)**2)/(2*(sig2**2))))
7
8
    cluster = '2344-4224'
                             #cluster ID
9
                    #bin size 250 km/s
    binval= 250
10
    models = []
11
    gsep = []
12
    ratlst = []
13
    crt = Table.read("fxcor_"+cluster+"_prom.cat",format="csv") #load catalog
14
    crt = crt[abs(crt["PEC_VEL"])<=3000]</pre>
                                             #only member galaxies
15
    gmodel = Model(double_gaussian)
                                        #initializate double gaussian model
16
    #generate an histogram
17
    x = np.array(crt["PEC_VEL"])
    x.sort()
19
    binval = 250
20
    upper = (np.around((x[len(x)-1]/binval))+1)*binval
21
    lower = (np.around(x[0]/binval)-1)*binval
22
    nbin = int(np.around((upper-lower)/binval))
23
    plt.clf()
24
    h = plt.hist(x,bins=nbin,range=(lower,upper))
25
    #fit model to histogram (initial quess values found by visual inspection)
26
    params = gmodel.make_params(amp1=6, mu1=750, sig1=400, amp2=6, mu2=-750, sig2=400)
27
    result = gmodel.fit(h[0], params, X=(h[1]+(binval/2))[:-1])
28
    models += [result]
29
```

Although, fitting the model to a discrete representation (an histogram with bin size equal to 250 km s⁻¹) of the density distribution may seem odd, this resolution is indeed enough for lmfit to find a coherent representation of the distribution with the initial guess parameters that we found by visual inspection. We use this method for all the selected clusters with a visually noticeable bimodal distribution (SPT-CLJ2344-4224, SPT-CLJ0144-4807, SPT-CLJ0451-4952, and SPT-CLJ0111-5518, and SPT-CLJ0354-5904. See Fig. 5.2). Fig. A.5 shows the best fit found for SPT-CLJ2344-4224 with this configuration.

From these functions we randomly generate distributions increasing the number of data points N up to 100 in ten different sets (N=10,20,...,100). We iterate each set 100 times and estimate the AD and KS test each time.

```
from statsmodels.stats.diagnostic import normal_ad
from statsmodels.stats.diagnostic import lilliefors as liltest

#
res = np.array(models[0].params) #select model
```

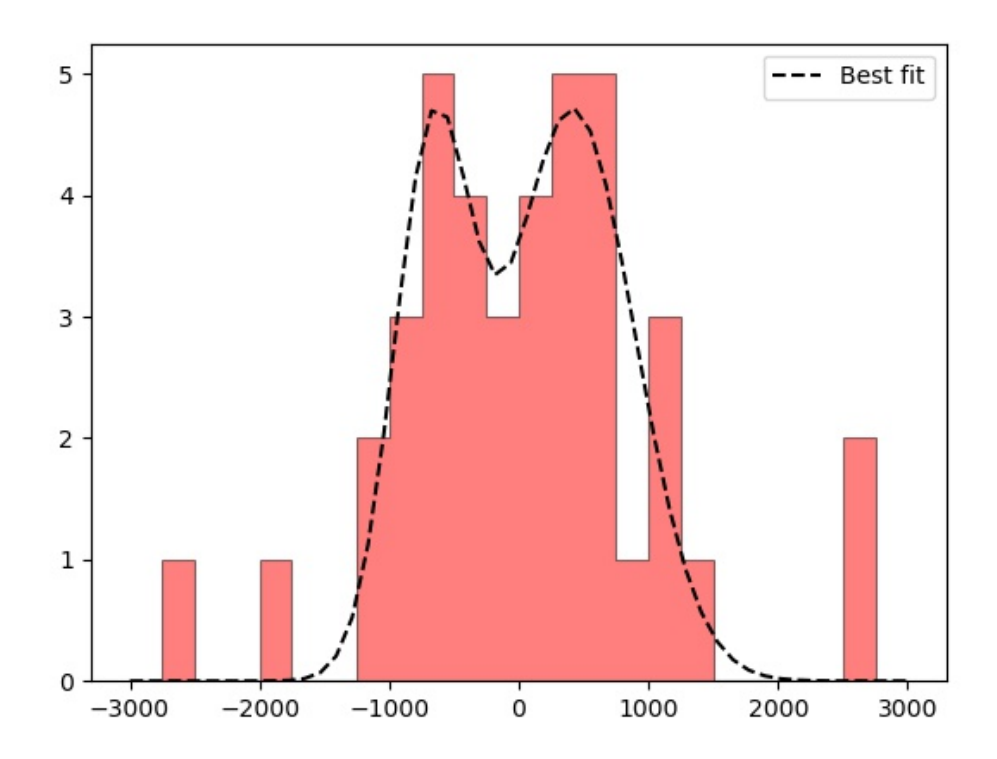


Figure A.5: Best Double Gaussian fit found by lmfit to the velocity profile of SPT-CLJ2344-4224.

```
gsep += [abs(res[1]-res[4])]
                                         #calculate separation of the Gaussians
    ratlst += [abs(res[2] / res[5])]
                                         #calculate sig1 / sig2
6
    nran = [10,20,30,40,50,60,70,80,90,100]
                                                 #initialization of sets
    p_lst = []
8
    d_1st = []
9
    for N in nran:
10
        ad_1st = []
11
        ks_lst = []
12
        for iter in range(100):
                                    #iterate 100 times for each set
13
             \#distribute\ data\ points\ weighted\ by\ sigma\ ratio\ n_1/sigma_1 = n_2/sigma_2
            n1=int(np.around((N / (abs(np.around(res[2],0))
15
                              + abs(np.around(res[5],0)))*abs(np.around(res[2],0))))
16
            n2=int(np.around((N / (abs(np.around(res[2],0)))
17
                              + abs(np.around(res[5],0)))*abs(np.around(res[5],0)))
18
             #generate Gaussians and stack them
19
            gdist1 = np.random.normal(res[1],abs(res[2]),n1)
20
            gdist2 = np.random.normal(res[4],abs(res[5]),n2)
^{21}
            gdist = list(gdist1) + list(gdist2)
22
```

```
#########AD##############
23
            x = gdist
24
            a,b = 3.6789468, 0.1749916
25
            aa, paa = adtest(np.sort(x))
26
            aastar = (aa)*(1+(0.75/len(x)) + (2.25/(len(x)**2)))
27
            alpha_ad = a*np.exp(((-1)*aastar)/b)
28
            if alpha_ad > 1:
29
                 alpha_ad = 1
30
            ad_lst += [alpha_ad]
31
             ######KS######
32
            D, pD = liltest(np.sort(x),dist="norm",pvalmethod="table")
33
            Dstar = D*(np.sqrt(len(x)) - 0.01 + (0.85/np.sqrt(len(x))))
34
            ks_lst += [Dstar]
35
        #take fraction of NG classifications
36
        p_lst += [len(np.array(ad_lst)[np.array(ad_lst)<0.05])/len(ad_lst)]</pre>
37
        d_lst += [len(np.array(ks_lst)[np.array(ks_lst)>0.895])/len(ks_lst)]
38
    rakt = Table(np.array([cluster]+p_lst),names=["N"]+nran)
39
    rakt2 = Table(np.array([cluster]+d_lst),names=["N"]+nran)
40
```

Finally, these python command lines are iterated for SPT-CLJ2344-4224, SPT-CLJ0144-4807, SPT-CLJ0451-4952, SPT-CLJ0111-5518, and SPT-CLJ0354-5904. The fraction of NG classifications for each set is shown in Table A.1, the last two columns in this table show the separation between the center of both Gaussian distributions d and the ratio of their velocity dispersions σ_1/σ_2 . To populate the components with data points we weight using this ratio following that $n_1/n_2 = \sigma_1/\sigma_2$, where n_1 and n_2 are the data points assigned to each Gaussian. As expected, while the number of data points increase in each set the fraction of NG classifications increase as the test's statistical power scales with sample size. The earliest set in which the fraction of NG classifications reach a 90% rate of detection is for the distribution function of SPT-CLJ0144-4807. This suggest that at least 70(100) galaxy members are needed by AD(KS) to safely discriminate a bimodal distribution with a separation of ~ 1300 km s⁻¹ and a presumably merger ratio of ~ 2 and we expect this number to be higher for shorter separations.

SPT-CL		10	20	30	40	50	60	70	80	90	100	$d (\mathrm{km}\mathrm{s}^{-1})$	σ_1/σ_2
J2344-4224	AD	0.07	0.06	0.14	0.16	0.32	0.48	0.5	0.74	0.63	0.74	1083	1.61
	KS	0.06	0.05	0.12	0.15	0.21	0.26	0.35	0.44	0.5	0.48		
J0144-4807	AD	0.05	0.15	0.45	0.51	0.66	0.81	0.94	0.92	0.99	0.98	1299	2.39
JU144-40U1	KS	0.07	0.09	0.21	0.32	0.55	0.67	0.8	0.86	0.85	0.91	1499	۵.39
J0451-4952	AD	0.02	0.1	0.24	0.25	0.39	0.57	0.58	0.65	0.74	0.79	1127	2.40
JU4J1-4JJZ	KS	0.04	0.06	0.15	0.14	0.22	0.35	0.39	0.45	0.58	0.62	1141	2.40
J0111-5518	AD	0.05	0.17	0.32	0.49	0.69	0.86	0.85	0.94	0.97	0.96	1632	1.77
90111-9910	KS	0.04	0.1	0.24	0.33	0.48	0.65	0.71	0.86	0.89	0.92	1032	1.11
J0354-5904	AD	0.08	0.16	0.14	0.27	0.35	0.42	0.56	0.69	0.67	0.87	1554	4.04
	KS	0.06	0.08	0.1	0.08	0.17	0.29	0.27	0.3	0.62	0.62		

Table A.1: Fraction of NG classifications

Notes. Fraction of NG classifications with AD and KS for visually selected bimodal clusters for each set (app. A.7). The last two columns indicate the separation between the center of both Gaussian distributions d in km s⁻¹ and the ratio of their velocity dispersions σ_1/σ_2 .

A.8 Statistics for 2D dynamical tests

```
##########confiq#########
    offsetesp = 1.2
2
    #offsetespra = offsetesp*np.cos(np.pi/4)
    #offsetespdec = offsetesp*np.sin(np.pi/4)
    n1 = [25,30,35]
    n2 = [25, 20, 15]
    offset = 1200
    sigma1 = [400, 475, 550]
    sigma2 = [400, 325, 250]
    sigmaesp1 = [0.375, 0.4375, 0.5]
    sigmaesp2 = [0.375, 0.3125, 0.25]
    niter = 100
13
    cmp = 2
    ang = 0
    ####################################
15
16
    crt_lst = []
    for nd in range(3):
```

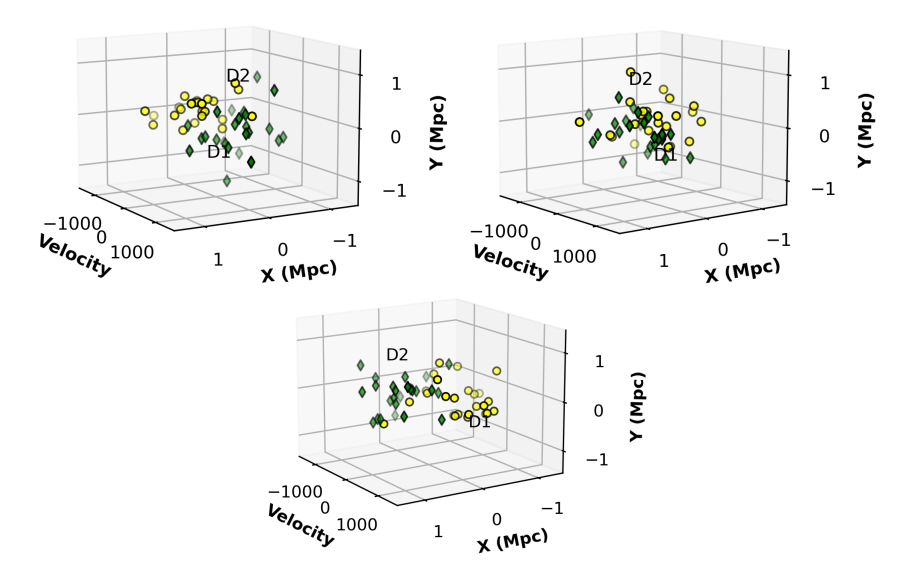


Figure A.6: Example samples generated for angle 0, 45, and 90.

```
Dstar_lst = []
19
        alpha_ad_lst = []
20
        pds_lst = []
        N2_BIC_1st = []
22
        for i in range(niter):
            24
25
            pos_matrix1 = [-(offset/2)*np.cos(ang*np.pi/180)
26
                           ,-(offsetesp/2)*np.sin(ang*np.pi/180),0]
27
            cov_matrix1 = [[(sigma1[nd])**2,0,0]
28
                           ,[0,(sigmaesp1[nd])**2,0],[0,0,(sigmaesp1[nd])**2]]
29
            D1 = np.random.multivariate_normal(np.array(pos_matrix1),np.array(cov_matrix1)
30
                                                ,size=int(n1[nd]))
31
            pos_matrix2 = [(offset/2)*np.cos(ang*np.pi/180)
32
                           ,(offsetesp/2)*np.sin(ang*np.pi/180),0]
33
            cov_matrix2 = [[(sigma2[nd])**2,0,0]
34
                           ,[0,(sigmaesp2[nd])**2,0],[0,0,(sigmaesp2[nd])**2]]
35
            D2 = np.random.multivariate_normal(np.array(pos_matrix2),np.array(cov_matrix2)
36
                                                ,size=int(n2[nd]))
37
            x3 = np.vstack((D1,D2))
38
```

This will generate the double Gaussian distribution depending on the value for ang. Notice that the collision direction is always in the velocity-X axis plane. Fig. A.6 show us an example of this.

We then estimate the dynamical statistics each time (see app. A.6) and save

them into alpha_ad_lst, Dstar_lst, DSp_lst, and N_GMM2D_lst. Then, when the 100 iterations ends, take the fraction of NG classifications in each array.

This will estimate the number of NG classifications by each statistic for each set and save them into crt_lst. This process is then iterated for the angles 0°, 45°, and 90°.